AN ABSTRACT OF THE DISSERTATION OF

Douglas E. Meisenheimer for the degree of Doctor of Philosophy in Environmental Engineering presented on March 17, 2020.

Title: Interfacial Relaxation and Two-Fluid Flow in Porous Media: A Fast X-Ray Microtomography Study

Abstract approved:

____

Dorthe Wildenschild

The flow of multiple immiscible fluids within a porous medium controls many natural and engineered systems in the environment including: geologic CO_2 sequestration, enhanced oil recovery from underground reservoirs, and contaminant remediation of groundwater. The need to understand how fluids are transported and distributed in these processes is important for designing accurate models that can improve process efficiency. The research comprising this dissertation developed and utilized a fast X-ray microtomography technique that allows for three-dimensional, near real-time, investigations of multiphase flow. Constitutive relationships based on multiphase state variables (saturation, capillary pressure, interfacial area, fluid topology) are tested for accurate predictions of quasi- and non-equilibrium two-fluid flow experiments in an effort to better understand the role of fluid relaxation on these relationships and state variables. The effect of bubble generation and transport, relevant to multiphase processes such as air stripping, on these relationships is also studied. Collectively, results show the need for constitutive relationships which include all four measured state variables to uniquely predict two-fluid flow independent of flow condition or bubble generation. An empirical relationship is also developed to predict interfacial area, an important mass transfer parameter, depending on the degree of relaxation within the system. Overall, the presented findings may help design more efficient engineering practices and transport models.

Interfacial Relaxation and Two-Fluid Flow in Porous Media: A Fast X-Ray Microtomography Study

by
Douglas E. Meisenheimer

A DISSERTATION

submitted to

Oregon State University

in partial fulfillment of
the requirements for the
degree of

Doctor of Philosophy

Presented March 17, 2020
Commencement June 2020

Doctor of Philosophy dissertation of Douglas E. Meisenheimer presented on March 17, 2020

APPROVED:

Major Professor, representing Environmental Engineering

Head of the School of Chemical, Biological, and Environmental Engineering

Dean of the Graduate School

I understand that my dissertation will become part of the permanent collection of Oregon State University libraries. My signature below authorizes release of my dissertation to any reader upon request.

Douglas E. Meisenheimer, Author

ACKNOWLEDGEMENTS

First and foremost, I would like to express my immense gratitude to Dr. Dorthe Wildenschild whose guidance has allowed me to survive and flourish within the ordeal that is a PhD program with her wonderful advice, technical knowledge, patience, and frequent reminders of the difference between “media” and “medium.” Her aide will be instrumental in my success as a scientist and research. I would also like to thank everyone in the Wildenschild group, but especially Chris Brueck, Rebecca Paustian, and Linnéa Andersson for their help with pulling off all-nighters at the synchrotron. Finally I would like to thank my family for their love and support throughout this process.

CONTRIBUTION OF AUTHORS

Portions of the research presented in this dissertation are a product of some wonderful collaborations with knowledgeable researchers in the subject area. Dr. Mark Rivers from The University of Chicago and GSECARS at the Advanced Photon Source, was instrumental in developing the pink-beam microtomography technique used throughout these studies. He also supplied the x-ray distribution graphs in Chapter 3. Dr. James McClure from Virginia Tech supplied the R scripts to run the GAMs in Chapters 4 and 6 and supplied instrumental help in using them and understanding their output. Finally, Dr. Dorthe Wildenschild provided technical, analytical, and editorial support on all Chapters comprising this dissertation.

TABLE OF CONTENTS

Page

TABLE OF CONTENTS (Continued)

TABLE OF CONTENTS (Continued)

Page

TABLE OF CONTENTS (Continued)

LIST OF FIGURES

LIST OF FIGURES (Continued)

LIST OF FIGURES (Continued)

Figure | Page

LIST OF FIGURES (Continued)

Figure Page

LIST OF TABLES

Interfacial Relaxation and Two-Fluid Flow in Porous Media: A Fast X-Ray Microtomography Study

Chapter 1. Introduction

1.1 Overview

Flow and transport of immiscible fluids within porous media is a field that controls many environmental engineering systems, both natural and engineered. An example of a multiphase system which is largely impactful to the environment is the vadose zone, or the region between the ground surface and the subsurface water table. In this region, water is transported through the air-shared pore space by hydrologic processes such as infiltration and surface runoff and ecologic process such as root uptake from plants. The need to understand how fluids are transported and distributed in this multiphase system is obvious due to its wide impact on societal and environmental health such as groundwater recharge and crop yields. Some other environmental multiphase systems include: geologic CO_2 sequestration, enhanced oil recovery from underground reservoirs, the transport and remediation of non-aqueous phase liquids (NAPLs) from groundwater aquifers or the vadose zone, and the removal of volatile organic compounds (VOCs) from groundwater utilizing mass transfer into produced gas phases to strip these contaminants from solution. Most of these processes are dependent on the distribution and concentration of the fluid-fluid interfaces (the fundamental difference between multiphase flow and single phase flow), such as the efficiency of geologic capillary trapping of CO_2 [Herring et al., 2013] or the availability of dissolved oxygen for bioremediation of groundwater contaminants [Fry et al., 1995]. Therefore, scientists and engineers in these fields require accurate models that can predict the multiphase transport in these systems for better and more efficient process operation.

In order to test theories and models of multiphase flow, experimental studies within porous media must be performed. This can be difficult as most of these processes occur over large amounts of space in the subsurface, and therefore multiphase flow can be studied at multiple length scales. The two scales of interest in this study are the pore-scale and macro-scale. At the pore-scale, the porous media is resolved to individually identify solid grains, the connected pore space between the solid phase which allows fluids to flow through the system, the spatial distribution of the fluid phases, and the resulting interfaces between the phases. These characteristics are averaged over a representative elementary volume (REV), which is defined as a volume that is large enough that properties of the system do not change with increasing volume, therefore providing statistically meaningful averaged properties at the macro-scale [Bear, 1988]. Because of this averaging, explicit spatial information is lost, but invariant parameters such as porosity, macroscopic capillary pressure, and specific fluid-fluid interfacial area are measured. This upscaling is important for multiphase models because utilizing pore-scale information would overly complicate models when trying to model transport on much larger scales.

Traditionally, practitioners have relied on empirical relationships between macroscopic capillary pressure (P_c) and wetting phase saturation (S_w) to model systems with two fluids (hereby referred to as two-phase flow). This relationship assumes that P_c is solely a function of saturation, while processes that affect fluid distribution such as solid wettability, fluid-fluid interfacial configuration, and pore morphology are not accounted. The $P_c(S_w)$ relationship is well known to exhibit hysteretic behavior, i.e. the relationship is process and history dependent, and therefore separate functions are needed depending on whether the system is draining (drainage) or filling (imbibition) with respect to the fluid that is wetting the solid surface. It has been proposed that a geometric description of the system needs to be included to uniquely describe two-phase flow systems. Hassanizadeh and Gray [1990, 1993] suggested that specific interfacial area (a_{nw}), the total interfacial area between the non-wetting and wetting fluids over the REV volume, accounts for variations in fluid configurations that can be present in a porous medium. They proposed that when taking into account interfacial area in the empirical relationships, such that Pc = $P_c(S_w, a_{nw})$, the drainage and imbibition $P_c(S_w, a_{nw})$ relationships would fall on a unique surface. This is important to modeling efforts because two-phase flow therefore could be uniquely described by one relationship without the need for multiple relationships and a tracking of fluid flow history in the system.

Other than fluid flow modeling efforts, interfacial area is also an important parameter in mass transfer of many environmental remediation processes. One such example is the use of macro- and nano-bubbles [Li et al., 2014] for techniques such as air sparging of gasoline contaminated aquifers and dissolved oxygen enhancement in bioremediation efforts. Therefore, it is important to study the generation of interfacial area within a porous medium (either from fluid displacement through two-phase flow or bubble transport and entrapment) under different flow conditions to achieve predictive tools that can be useful under a variety of situations.

There has been a concerted effort in the literature to validate the theories presented by Hassanizadeh and Gray both numerically [Held & Celia, 2001; Joekar-Niasar & Hassanizadeh, 2011; Joekar-Niasar et al., 2008; Porter et al., 2009; Reeves & Celia, 1996] and experimentally [Chen et al., 2007; Cheng et al., 2004; Karadimitriou et al., 2013; Porter et al., 2010; Pyrak-Nolte et al., 2008]. These studies have shown that the $P_c(S_w, a_{nw})$ relationship is unique, within experimental error, under quasi-equilibrium flow conditions. However, a lingering question is whether these observations hold true under non-equilibrium flow conditions. Many multiphase systems within the environment do not occur under equilibrium conditions; therefore, it is important to generate the $P_c(S_w, a_{nw})$ relationship under non-equilibrium conditions. This has been done in two-dimensional micromodels [Godinez-Brizuela et al., 2017; Karadimitriou et al., 2014] and using simulations via dynamic pore-network modeling [Joekar-Niasar & Hassanizadeh, 2012]. The dynamic pore-network model found some differences between the transient and quasi-static $P_c(S_w, a_{nw})$ surfaces, but determined that the differences were negligible. The micromodel studies, on the other hand, determined that the transient and quasi-static $P_c(S_w, a_{nw})$ surfaces were statistically different. There has not yet been any effort to generate 3-dimensional experimental data comparing the $P_c(S_w, a_{nw})$ relationship under quasi- and non-equilibrium conditions. But, recent advances in pore-scale imaging of multiphase flow using fast X-ray microtomography (an imaging technique that allows for near real-time visualization of fluids within a 3-dimensional opaque porous medium) can be used to generate non-equilibrium 3-dimensional experimental data, which is the main focus of this study.

An assumption underlying the $P_c(S_w, a_{nw})$ relationship is that each fluid phase is continuous, but in most circumstances this condition is not met in two-phase flow systems especially under more dynamic conditions [Wildenschild et al., 2001; 2005]. Therefore, other state variables have been investigated that can describe connectivity and shape of the fluids, such as fluid topology [Herring et al., 2013; McClure et al., 2016; Schlüter et al., 2016]. The Euler characteristic of the nonwetting phase (χ_n) has been used as the standard to measure the connectedness of fluid configurations. Schlüter et al. showed that the Euler characteristic conveys complementary information that helps explain the hysteresis present in the $anw(Sw)$ relationship. Using a lattice Boltzmann model, McClure et al. further demonstrated that the inclusion of χ_n in the $P_c(S_w, a_{nw})$ relationship is unique under equilibrium (2016, 2018) and dynamic (2018) conditions.

1.2 Research Goals

The goal of this research is to generate high resolution, 3-dimensional, X-ray microtomography (µCT) data of non-equilibrium two-phase flow. This data can then be used to develop a better understanding of the effect of flow condition (quasi- or non-equilibrium flow) on invariant parameters of two-phase flow and the applicability of state variable constitutive relationships in predicting two-phase flow under different fluid flow conditions. The specific objectives for this research are as follows:

1. Develop a fast x-ray microtomography methodology at the Advanced Photon Source 13-BMD beamline to image non-equilibrium two-phase flow.
2. Collect 3-dimensional µCT data for quasi- and non-equilibrium flow with and without bubble formation and transport.
3. Investigate the effect of bubble formation and flow condition of the two-phase flow state variables (P_c, S_w, a_{nw}, χ_n).
4. Investigate the effect of fluid relaxation on formation of interfacial area.

5. Test the ability of the state variable constitutive relationships to predict the state of a two-phase system under the various testing situations.

1.3 Document Organization

Chapter 2 provides a brief review of the literature and theoretical background relevant to this research. Chapter 2 is divided into three sections, the first of which provides a brief discussion on the basics of multiphase flow. The second section discusses empirical relationships used to predict the state of two-phase flow systems. The third section provides a brief overview of x-ray microtomography which is the experimental technique that was modified and utilized for the investigations comprising the research presented in this dissertation.

Chapter 3 presents the development and optimization of a fast x-ray microtomography technique using pink-beam radiation at the Advanced Photon Source GSECARS 13-BMD beamline. This imaging technique was used to accomplish the research presented in Chapters 4, 5 and 6. Quasi- and non-equilibrium two-phase flow experiments were imaged and analyzed to measure multiphase state variables (capillary pressure, saturation, interfacial area, Euler characteristic) in Chapter 4. With these measures a study on the effect of flow condition on constitutive state variable relationships was then tested and compared with similar studies performed in 2-dimensonal micromodels and Lattice-Boltzmann models. In Chapter 5, the interfacial area measurements from Chapter 4 were compared with datasets in the literature to study the effect of fluid relaxation in quasi-equilibrium experiments on interfacial area generation. An empirical $a_{nw}(S_w)$ relationship is presented in an effort to predict interfacial area for a given system dependent on the number of quasi-equilibrium relaxation points taken during a drainage or imbibition experiment. A set of quasi- and non-equilibrium two-phase flow experiments with bubble formation and transport were collected and presented in Chapter 6 to investigate the effect of bubbles on multiphase state variables and constitutive relationships was studied.

Finally, Chapter 7 provides a summary and the major conclusions of the research presented in this dissertation.

Chapter 2. Background

2.1 Basics of Multiphase Flow

2.1.1 Wettability, contact angle and surface tension

Two-phase flow processes consist of two fluid phases (liquid or gas) permeating through a solid matrix. The fluid that holds a higher affinity with the solid phase is termed the wetting phase and spreads along the solid surface more readily than the other fluid which is termed the non-wetting phase. This preferential affinity of the solid phase for one fluid over another is defined as wettability. The porous medium mainly used in this work is a packed bed of hydrophilic soda-lime glass beads that are characterized as water-wet due to their preference to be coated by water rather than the non-wetting phase (air). The wettability characteristics of a solid can be determined experimentally by measuring the contact angle (θ) that the fluid is pinned in relation to the solid surface (shown in Fig. 2-1). In geological applications, the contact angle is usually measured through the aqueous phase.

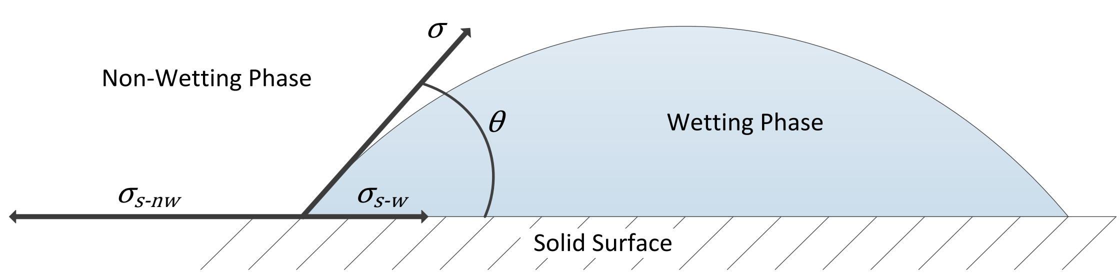

Figure 2-1. Drop of water on flat surface with representative contact angle and surface tensions.

The fluid with a θ between 0º and 90º is defined as the wetting phase and the fluid with a contact angle between 90º and 180º is the non-wetting phase. The contact angle, and therefore the wettability of the system, is dependent on the thermodynamic need to minimize free surface energy. Surface energy can be conceptualized as the energy required to cut a block of material (e.g. water) in half. The energy required to break the cohesive bonds along the cut is equal to the free surface energy present in the two created surfaces (assuming a reversible process). The energy required to make these surfaces is therefore directly related to the surface area created. The relationship of energy per unit area, or more commonly force (F) per unit length (L), is defined as surface tension (σ) and is represented in Eq. (2.1):

$$\sigma = \frac{F}{2L} \tag{2.1}$$

At thermodynamic equilibrium, the forces need to balance on the contact line where all three phases are present. Therefore, the surface tensions (for a given unit length) determine the contact angle of the fluids and is described by Young's equation (for a 2D system):

$$\sigma_{s-nw} = \sigma_{s-w} + \sigma\cos\theta_c \tag{2.2}$$

where σ_{s-nw} is the surface tension between the solid and non-wetting phase, σ_{s-w} is the surface tension between the solid and wetting phase, σ is the interfacial tension between the fluid phases, and θ_c is the equilibrium contact angle.

2.1.2 Contact angle hysteresis

Dependence of a physical property on the history of the system is defined as hysteresis. Young's equation (Eq. (2.2)) uses an equilibrium contact angle because there is a range of contact angles that are possible depending on the history of the system. For example, if the solid surface in Fig. 2-1 was angled so that the water droplet started moving down the surface there would be a an advancing (θ_A) and receding contact angle (θ_R), as shown in Fig. 2-2. This effect is caused by the adhesive force of water with the solid surface and surface roughness which creates local energy barriers that the water has to overcome to wet the surface.

The fact that θ_A is significantly larger than θ_R is known as contact angle hysteresis [Dullien, 1992]. Hysteresis, therefore, has a complicating effect on accurately characterizing the movement of fluids in porous media. For example, imagine an air-water interface that is repeatedly moved back and forth within a capillary tube. If the contact angle was measured randomly without knowing the current flow conditions it would be impossible to tell in which direction the interface was moving if the contact angle was between θ_A and θ_R. The importance of hysteresis on multi-phase fluid flow characterization is discussed further in Section 2.2.

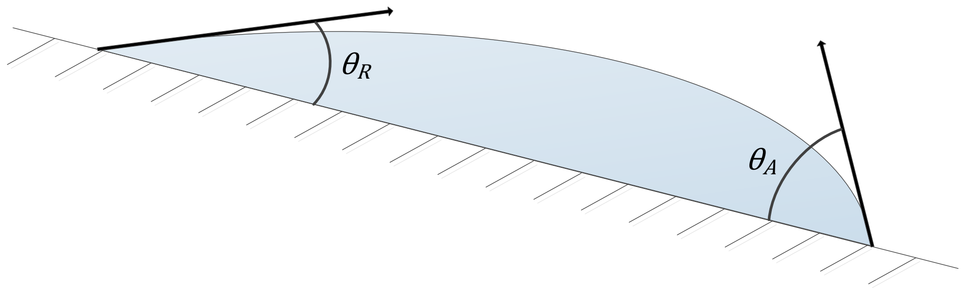

Figure 2-2. Drop of water on tilted surface with representative advancing and receding contact angles.

2.1.3 Capillary pressure

Equilibrium capillary pressure (P_c^{eq}) is defined as the pressure difference across an interface between two static fluids. The Young-Laplace equation relates this difference between the bulk pressures of the fluid phases to the interfacial tension, contact angle, and curvature of the fluid-fluid interface:

$$P_c^{eq} = P_n - P_w = \sigma \left(\frac{1}{r_1} + \frac{1}{r_2}\right) cos\theta \tag{2.3}$$

where r_1 and r_2 are the two principal radii of curvature at a point on the fluid-fluid interface [L^{-1}]. In strongly water-wet porous media the contact angle can be estimated as $\theta = 0^o$ and Eq. (2.3) can be reduced to:

$$P_c^{eq} = 2J_{nw}\sigma \tag{2.4}$$

where J [L] is the mean curvature of the fluid-fluid interface. In 2D micromodel studies, only one curvature can be measured, so the two principal radii are set equal which assumes a spherical interface.

In non-equilibrium flow conditions, pressures are imposed on fluid reservoirs to induce flow, thereby creating pressure gradients throughout the fluid phases that are functions of time and space. The capillary pressure at the fluid-fluid interface, therefore, does not equate to the differential pressure between the reservoir pressure conditions as in Eq. (2.3). The difference between the dynamic capillary pressure (P_c^{dyn}) and P_c^{eq} is commonly modeled as [Hassanizadeh et al., 2002]:

$$P_c^{dyn} - P_c^{eq} = -\tau \frac{\partial S_w}{\partial t} \tag{2.5}$$

where τ (M L^{-1} T^{-1}) is a material coefficient that is a measure of the speed in which a change in saturation takes place and $\partial S_w/\partial t$ is the rate of change of saturation.

2.1.4 Topology of the non-wetting phase

Topology, or the way that constituent parts are distributed and interrelated , had been measured in multiphase systems by the Euler characteristic (e.g. Herring et al., 2013), χ, which is a topological invariant that describes the connectivity of a fluid phase. It is described by the following relationship:

$$\chi = \beta_0 - \beta_1 + \beta_2 \tag{2.6}$$

where β_0 is the number of distinct regions of the fluid phase, β_1 is the number of redundant connections within each distinct region, and β_2 is the number of encapsulated voids in each region. The β_2 value for the non-wetting phase can be neglected in air-water experiments since an element of water or solid could not be completely suspended in air. Fundamentally, the Euler characteristic quantifies the entrapment and breaking up of fluid connections in pore throats (i.e. snap-off) during multiphase flow.

2.2 Constitutive Relationships Modeling Fluid Configuration

Constitutive (or empirical) relationships are developed (usually empirically but relations from first principles are also possible) to describe a given system with the essential features of that system, usually to close a system of equations [Miller et al., 1998]. An important constitutive relationship in multiphase history is the relation between capillary pressure and saturation (P_c-S_w), a schematic example of which is shown in Fig. (2-3).

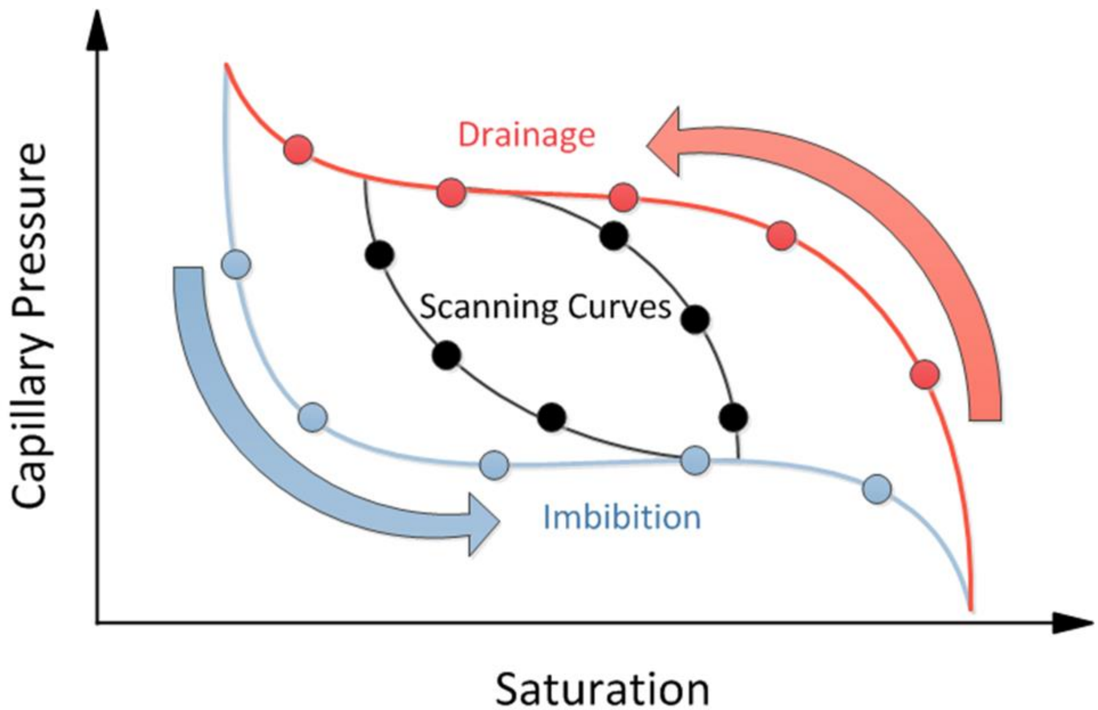

Figure 2-3. A schematic example of the relationship between capillary pressure and saturation. The main drainage and imbibition loop is shown with examples of scanning curves which start at intermediate saturations.

This P_c-S_w is widely known to be hysteric, meaning that separate functions need to be developed whether the system is undergoing imbibition or drainage as seen by the separation between the curves in Fig. (2-3), and dependent of the porous medium and fluid properties [Miller et al., 1998]. There have been attempts to address these issues including the J-Leverett function which nondimensionalizes the P_c-S_w curves as a function of permeability, surface tension and wettability [Leverett, 1941]; as well as the Brooks and Corey [Brooks & Corey, 1964] and van Genuchten [1980] models; but most of these are limited in their applicability. It can be argued that models should be developed based on first principles which can describe the simultaneous movement of two (or more) fluids in a porous media, which these relationships lack. Fundamentally, the difference between single and multi-phase flow is the existence of fluid-fluid interfaces. The inclusion of interfaces and evolutionary terms in conservation equations would allow for the accounting of multiple fluids. Hassanizadeh and Gray [1990, 1993] thereby hypothesized that the inclusion of specific interfacial area in the *Pc-S* relationship would provide a non-hysteretic solution, where drainage and imbibition P_c-S_w-a_{nw} surfaces would overlap and one surface could describe the system. More recently, researchers have proposed that further extension of this relationship to include Euler characteristic, or a measure of the distribution of fluids within a system, to uniquely describe a system [McClure et al., 2016].

2.3 X-Ray Computed Microtomography (μCT)

X-ray computed microtomography (μCT) is an experimental technique that can non-destructively image the microstructure of 3-dimensional, opaque materials. This is done by utilizing the differences in X-ray attenuations between phases from differences in density and X-ray adsorption edges of the phases. In general, X-rays are emitted from a source (either from a synchrotron such as the Advanced Photon Source, or from a lab-scale μCT unit) and passed through the sample before being received by a detector which measures the X-ray attenuation at each point in the sample, collecting a two-dimensional X-ray attenuation map of the sample (i.e. a radiograph). The sample is then rotated in the X-ray beam 180 degrees in small angle increments and a radiograph is collected at each of these angles. The collected radiographs are then mathematically reconstructed into a 3-dimensional image of the sample that can be used to visualize cross-sections through the sample and measure parameters of interest (such as saturation, capillary pressure, interfacial area, and Euler characteristic). The use of dopant in a phase of interest changes the x-ray attenuation of a sample to make it more easily distinguishable in μCT images from the other phases. Therefore the standard μCT technique is to use a monochromator to reduce the full-spectrum X-ray beam to a single energy (Fig. 2-4(a)) slightly above the x-ray adsorption edge of the dopant. This generates an image with high contrast between the phases of interest allowing for easier separation of the phases (i.e. segmentation) during image analysis.

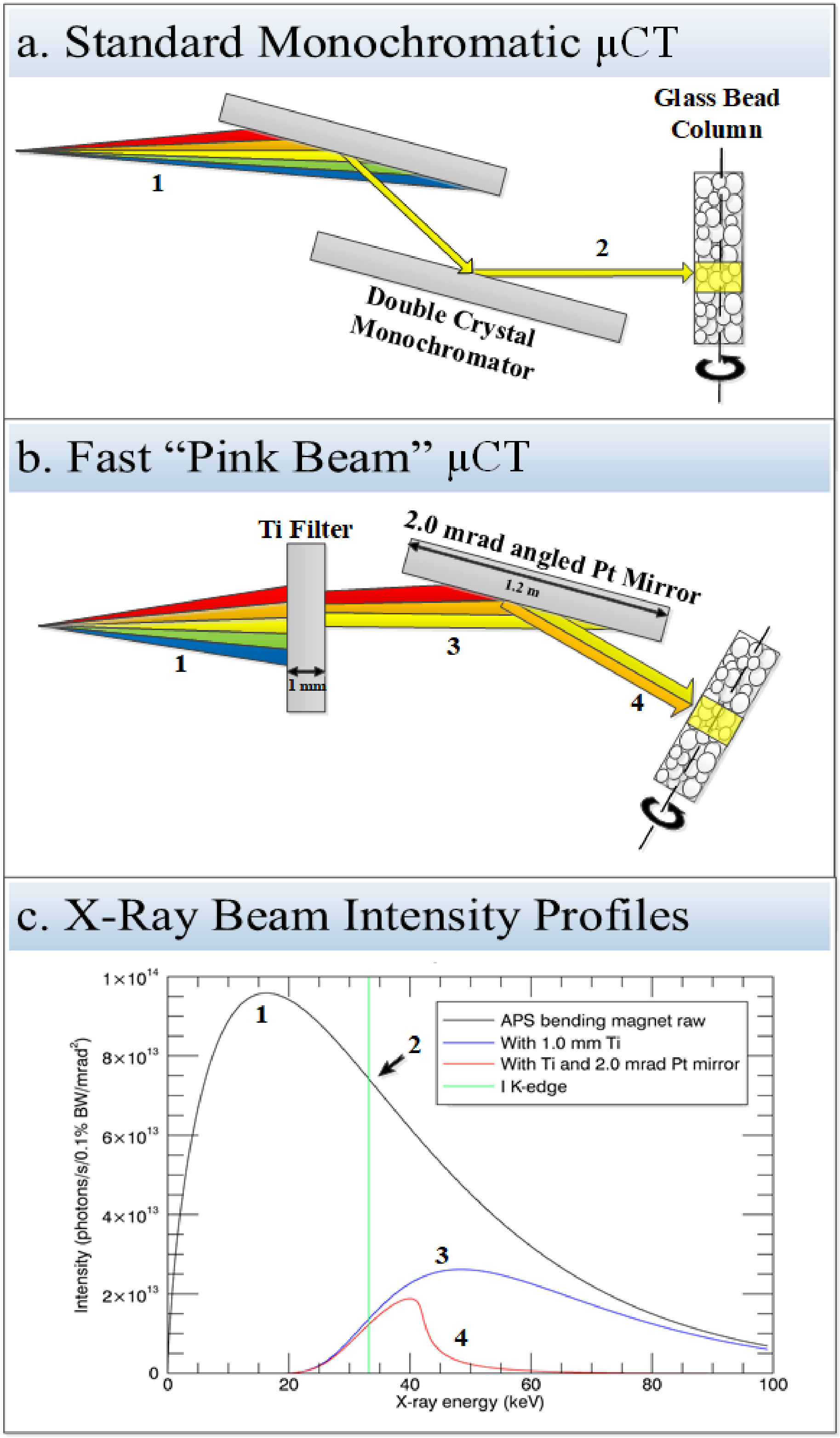

Figure 2-4. (a) The standard monochromatic and (b) fast X-ray beam setups at the Advanced Photon Source, not drawn to scale. (c) X-ray beam intensity profiles for the (1) white beam, (2) monochromatic beam, and a pink beam configuration (3) after passing through a Ti filter and (4) after reflection from a 2.0 mrad angled Pt mirror.

There have been a variety of application for this technology to investigate multiphase flow in porous media (e.g. Cnudde & Boone, 2013; Wildenschild & Sheppard, 2013) using standard microtomography, though images can take ~15 minutes at the synchrotron which imposes quasi-equilibrium conditions on any fluid experiments. But with recent advances in x-ray systems and detectors, fast μCT methods have been developed which allow researchers to study processes in near real-time. Some of the first instances of using fast μCT techniques to visualize three-dimensional samples undergoing rapid changes were conducted at the European Synchrotron Radiation Facility [Michiel et al., 2005] and the Swiss Light Source (SLS) [Mokso et al., 2010] using a monochromatic methodology. Another fast μCT technique utilizes a broader range of x-ray energies to image (i.e. pink-beam). This technique is shown in Fig. (2-4b). Pink beam is acquired by filtering the low and high x-ray energies from the full-spectrum white beam that is produced at the synchrotron. The difference in x-ray intensities between the methods can be seen in Fig. (2-4c). The majority of the research presented in this dissertation is the optimization of a pink-beam technique for multiphase flow, and the subsequent use of the technique to study and compare quasi- and non-equilibrium flow.

Chapter 3. Optimizing Pink-Beam Fast X-Ray Microtomography for Multiphase Flow in 3D Porous Media

Douglas E. Meisenheimer[1], Mark L. Rivers[2] and Dorthe Wildenschild[1]

1. School of Chemical, Biological, and Environmental Engineering, Oregon State University, Corvallis, Oregon, U.S.A.

2. Department of Geophysical Sciences and Center for Advanced Radiation Sources, The University of Chicago, Chicago, Illinois, U.S.A.

Journal of Microscopy, Wiley-Blackwell
111 River St, Hoboken, NJ 07030, USA
Volume 277, Issue 2
https://doi.org/10.1111/jmi.12872

3.1 Abstract

A fast pink-beam X-ray microtomography methodology was developed at the GSECARS 13-BMD beamline at the Advanced Photon Source to study multiphase flow in porous media. The white beam X-ray distribution of the Advanced Photon Source is modified using a 1-mm copper filter and the beam is reflected off a platinum mirror angled at 1.5 mrad, resulting in a pink beam with X-ray intensities predominately in the range of 40–60 keV. Bubble formation in the wetting phase and wettability alteration of the solid phase from x-ray exposure can be a problem with high flux and high energy beams, but the suggested pink-beam configuration mitigates these effects. With a 14-second acquisition time for capturing a complete dataset, the evolving fluid-fronts of non-equilibrium three-dimensional multiphase flow can be studied in real-time and the images contain adequate image contrast and quality to measure important multiphase quantities such as contact angles and interfacial areas.

3.2 Introduction

Understanding multiphase flow in porous media is important to many fields including groundwater management and remediation, soil and agricultural practices, CO2 sequestration and petroleum engineering. Scientists and engineers in these fields require experimental data acquired under field conditions to accurately create models of the dynamic multiphase flow processes being studied. The recent introduction of fast X-ray microtomography (μCT) allows multiphase flow experiments to be observed in three dimensions under non-equilibrium flow conditions. This methodology eliminates the need to make the decision to either make assumptions regarding the third dimension when using two-dimensional micromodels [Godinez-Brizuela et al., 2017] or generate data only under quasi-equilibrium flow conditions using standard μCT methods [Porter et al., 2010].

Some of the first instances of using fast μCT techniques to visualize three-dimensional (3D) samples undergoing rapid changes were conducted at the European Synchrotron Radiation Facility [Michiel et al., 2005] and the Swiss Light Source

(SLS) [Mokso et al., 2010]. Berg et al. [2013] and Youssef et al. [2013] were among the first to investigate multiphase flow using fast µCT. Since then, a handful of multiphase flow studies have been published [Andrew et al., 2015; Armstrong et al., 2014; Rücker et al., 2015; Singh et al., 2017], most of which were performed at the TOMCAT beamline at the SLS. This beamline utilizes a superbend bending magnet to deliver sufficient X-ray flux while also allowing for a monochromatic beam to enable edge-specific scanning for increased image contrast and quality. The TOMCAT beamline allows for scan times on the order of 1–20 seconds while still achieving a decent field of view (FOV) (3–4 mm in each direction). Schlüter et al. [2016; 2017] did collect 3D experimental data in a time-resolved experiment using pink-beam µCT at the Advanced Photon Source (APS), however, this initial pink-beam fast µCT experiment had a relatively limited temporal resolution of 113 seconds. Although this is almost an order of magnitude faster than conventional monochromatic methods, Berg et al. (2013) concluded that time resolutions of 10–30 seconds are needed to observe differences in fluid front configurations for non-equilibrium flow. This study was designed to optimize the parameters of pink-beam scanning to provide adequate temporal resolution for non-equilibrium multiphase flow, optimize image quality to accurately measure multiphase quantities such as interfacial curvature and ultimately verify that the physics of the system is not affected by the methodology.

3.3 Methods

3.3.1 X-ray beam and scanning parameter selection

The experiments were performed at the GSECARS 13-BMD beamline at the APS located at Argonne National Laboratory. The white X-ray beam from the bending magnet was converted to pink beam by reflecting the filtered beam vertically down from a platinum mirror toward the experimental setup, effectively removing high energy X-rays. Low-energy X-rays were removed with an in-line water-cooled filter. Initial experimentation resulted in excessive bubble formation in the wetting phase due to radiation exposure from the pink beam, presumably due to hydrolysis. X-ray absorption in the water is greater at low energies, therefore, it was hypothesized that changing the in-line filter to something that would remove more of the low-energy X-rays would alleviate bubble formation, at the expense of contrast. Initially, a 1-mm titanium in-line filter was utilized. The titanium filter would be ideal for image contrast as the peak of the X-ray distribution would be closest to the iodine K-edge (we use iodine as a contrast agent to better distinguish water from air in the flow system). Fig. 3-1a depicts the X-ray intensity distribution of the initial setup (1 mm Ti filter, 2.0 mrad Pt mirror angle) with the peak intensity slightly above the iodine K-edge. In addition to the titanium filter, metal strips (1 mm Al or 0.5 mm Cu) were placed in the X-ray beam upstream of the sample, to reduce the low- energy X-rays and overall X-ray flux without affecting the peak X-ray energy (Fig. 3-1b). The 1 mm in-line copper filter was also tested (Fig. 3-1c,d) to reduce low-energy X-rays even further. The angle of the platinum mirror was adjusted at various angles (1.0, 1.5 and 2.0 mrad) to generate optimal X-ray flux for acceptable image contrast, and image acquisition time relevant to studying non-equilibrium multiphase flow.

Two experimental scanning approaches were utilized in the study. One was a continuous scanning approach where the sample was exposed to X-rays for the entire duration of the experiment. The other consisted of intermittent scanning, where the sample was scanned once per minute and the X-rays shut off between scans. These different scanning approaches were used to determine the effect of X-ray dose on bubble formation.

The exposure time, which largely controls the signal-to-noise ratio (SNR) of the tomographic images, and therefore, the overall image quality, was also tested. Exposure time also controls the duration it takes to acquire a full tomogram so, to a lesser degree, it also affects X-ray dose under the intermittent scanning method.

3.3.2 Experimental setup

All experiments were conducted in randomly packed soda-lime glass bead (0.8–1.2 mm) sintered in a borosilicate glass column. A new glass bead pack column was used for each experiment. The columns were saturated with water before X-ray exposure. The water was doped with potassium iodide at a 1:6 mass ratio to provide contrast

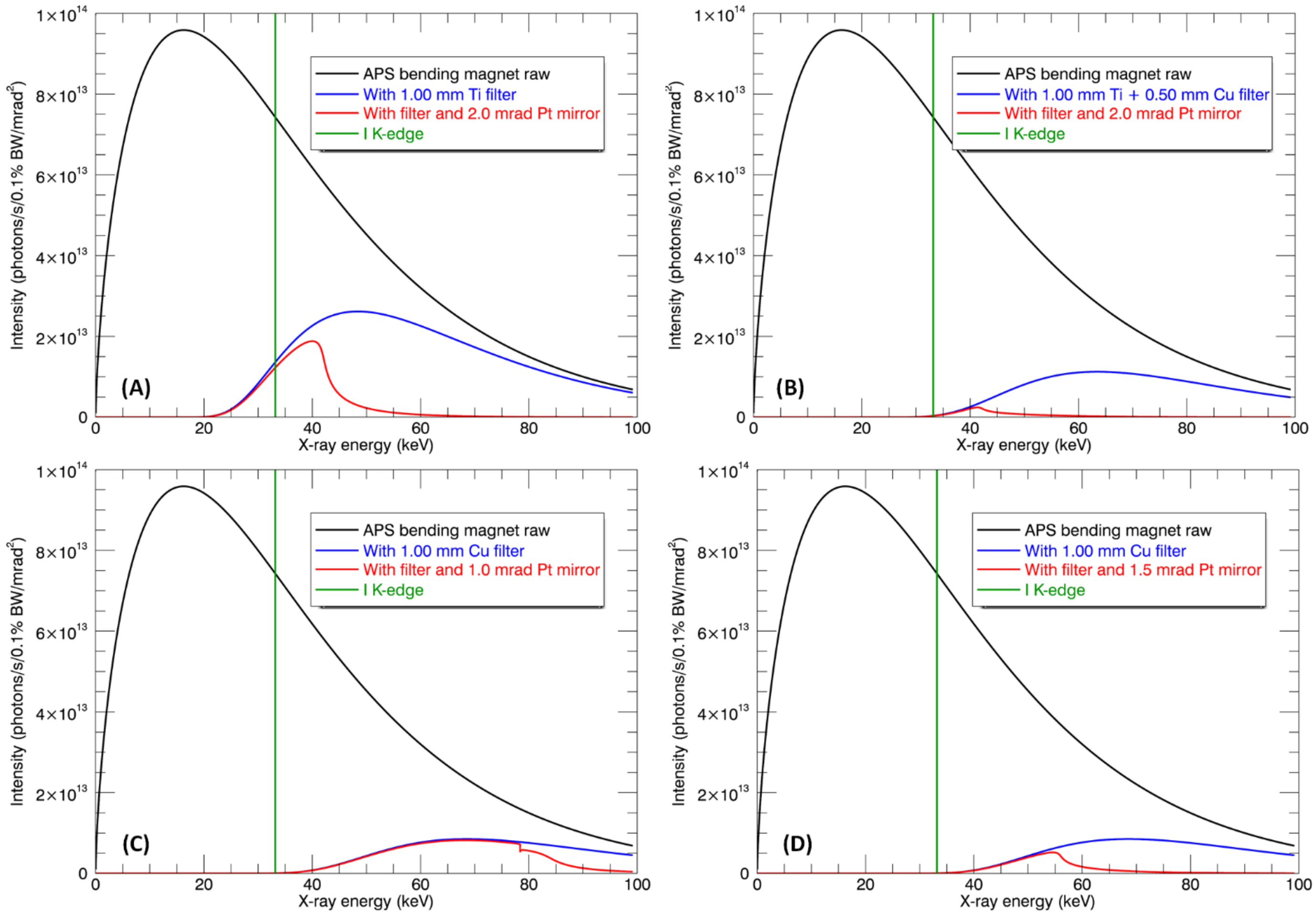

Figure 3-1. X-ray intensity distributions for white beam (black), after passing through an absorber (blue), and after mirror reflection (red) for each beam configuration: (A) 1.0 mm Ti filter + 2.0 mrad Pt mirror; (B) 1.0 mm Ti and 0.5 mm Cu filters + 2.0 mrad mirror; (C) 1.0 mm Cu filter + 1.0 mrad mirror; (D) 1.0 mm Cu filter + 1.5 mrad mirror. Iodine K-edge is in green.

between the water and gas phases in the X-ray images. A control experiment with deionized (DI) water was also tested to determine if the contrast agent was contributing to the generation of bubbles.

3.3.3 Image collection and processing

All scans were collected with a12-bit Point Grey Grasshopper3 CMOS camera with 1920 × 1200 pixels. A 100 microns thick lutetium aluminum garnet scintillator was used, with a Nikon Macro lens imaging the scintillator onto the camera. The resulting pixel size was 3.2 × 3.2 μm. Each acquisition consisted of a 180° rotation of the sample with two-dimensional projections acquired at 900 angle. The projections were reconstructed into 3D images with the tomoRecon software based on Gridrec (Rivers, 2012). The images were denoised using a nonlocal means filter and then segmented using a watershed segmentation using the Avizo™ image processing software.

3.4 Results

3.4.1 Pink-beam parameterization testing to minimize bubble formation

We present a methodical approach to preventing bubble formation in the water phase of a representative porous medium by adjusting pink-beam scanning parameters. Volumes of separate phases (water, bubble and solid) were calculated by counting pixels and multiplying by the voxel size, 3.2 μm^3. The glass bead columns had an average porosity of 0.388 ± 0.003. Bubble saturations were calculated by dividing the bubble volume by the total pore space volume. The rate of bubble saturation change (dS_{NW}/dt) was calculated as the change in bubble saturation over the time between each acquisition and an average dS_{NW}/dt was then calculated for each experiment. This average value is used for any following references to dS_{NW}/dt.

Under the initial pink-beam setup in Fig. 3-1a (1 mm Ti filter, 2 mrad Pt mirror angle, continuous scanning method), a dS_{NW}/dt of $2.23 \cdot 10^{-2}$ was observed. Bubble volumes and 3D visualization of the bubble formation over time is presented in Fig. 3-3(a-c). A DI water standard was subjected to the same scanning conditions and approximately an order of magnitude slower rate was observed, dS_{NW}/dt =

$3.97 \cdot 10^{-3}$. Therefore, radiation exposure of the KI-doped water does produce more bubbles, likely due to increased interaction with the incoming X-rays; however, DI water alone also produces a non-negligible volume of bubbles. We hypothesize that bubble formation can mostly be attributed to hydrolysis of the water or some other chemical reaction occurring with the production of free radicals in the water from X-ray exposure. Based on Henry's Law calculations, only a 2–3% bubble saturation could be attributed to exolution of air dissolved in the water at standard temperature and pressure, yet bubble saturations of up to 57% were observed in the initial experiment.

Decreasing the X-ray dose as much as possible, in addition to reducing low-energy X-rays with different filters, were hypothesized to further reduce bubble formation. These initial scans were conducted under the continuous scanning approach with constant X-ray exposure throughout the experiments. As mentioned previously, we also tested the intermittent scanning approach where X-rays were shut off between scans. Using this intermittent approach, the dS_{NW}/dt in the DI water standard was reduced an additional order of magnitude, $dS_{NW}/dt = 3.14 \cdot 10^{-4}$, to a negligible rate relative to the time scale of non-equilibrium two-phase flow experiments. A dS_{NW}/dt on the order of 10^{-4} was deemed acceptable, and a necessary trade-off, that allows a researcher to utilize pink-beam radiation for investigating two-phase flow.

Additional filters were added to the 1 mm Ti in-line filter and tested for their effectiveness in preventing bubble formation. Various thicknesses of Al were added, but none had a significant effect on dS_{NW}/dt. Adding a 0.5-mm Cu filter (Fig. 3-1b) decreased the rate of bubble formation to a level similar to what was observed for the DI water standard (Table 3-1). With a 0.5-mm Cu filter, the X-ray flux was, however, insufficient to generate a decent SNR at an exposure time relevant for non-equilibrium flow imaging. This large reduction of X-ray flux can be seen in Fig. 3-2b in relation to the other scanning parameters tested. Even though the Ti filter would be the best option in terms of optimizing image contrast (by keeping the X-ray intensity peak located near the iodine k-edge), the in-line 1- mm Cu filter would most likely provide the best results in terms of preventing bubble formation.

Table 3-1. Pink beam testing parameterization and bubble formation rates.

Wetting Phase	In-line Filter	Additional Filter	Pt Mirror Angle (mrad)	Exposure Time (ms)	dS_{NW}/dt intermittent	dS_{NW}/dt continuous	Fig. 3-1	Fig. 3-2
DI Standard	1mm Ti	- -	2	7	3.14E-04	3.97E-03	- -	- -
1:6 KI	1mm Ti	- -	2	7	- -	2.23E-02	A	Initial
	1mm Ti	1mm Al	2	10	7.66E-03	1.51E-02	- -	- -
	1mm Ti	0.5mm Cu	2	20	- -	2.54E-03	B	- -
	1mm Cu	- -	1	20	- -	8.53E-03	C	- -
	1mm Cu	- -	1.5	20	1.88E-04	1.55E-03	D	Final

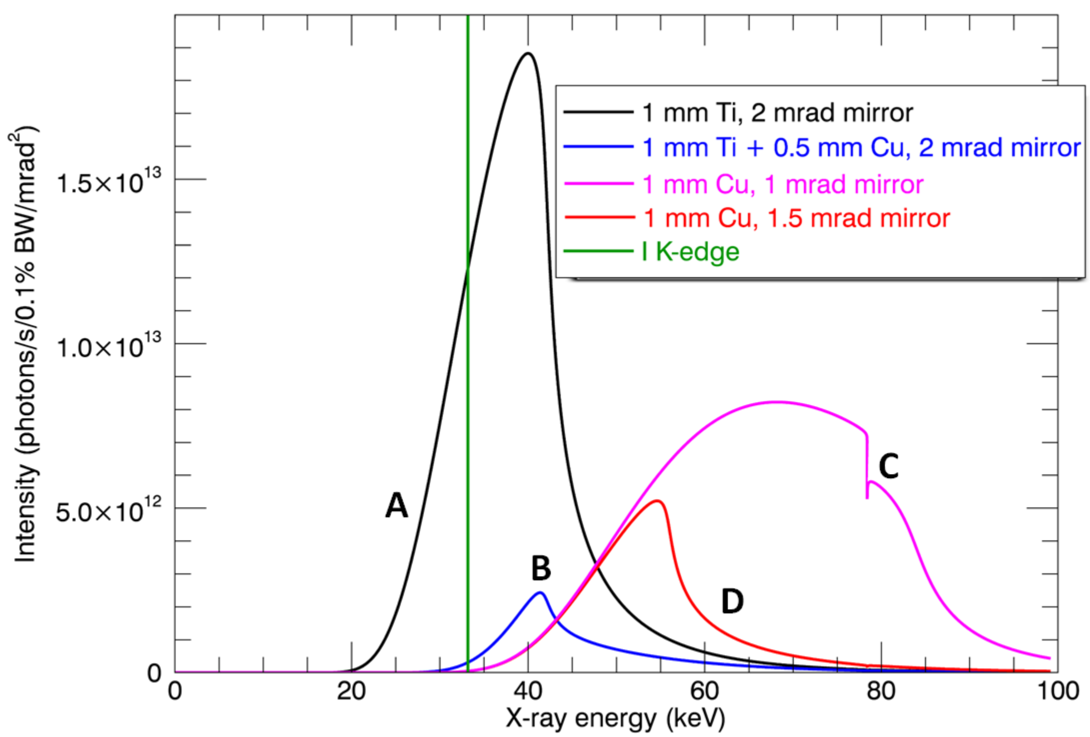

Figure 3-2. X-ray intensity distribution comparison for each beam configuration (filter(s) + Pt mirror angle) presented in Figure 1: (A) 1.0 mm Ti + 2.0 mrad; (B) 1.0 mm Ti and 0.5 mm Cu + 2.0 mrad; (C) 1.0 mm Cu + 1.0 mrad; (D) 1.0 mm Cu + 1.5 mrad. Iodine K-edge is in green.

In an attempt to improve the SNR, the 1-mm Cu filter was tested with a mirror angle of 1 mrad to increase the X-ray flux over that of the previous experiment. Even though this provided an acceptable SNR, the rate of bubble formation was only slightly improved from the initial pink-beam setup (Table 3-1). However, increasing to a 1.5 mrad mirror angle to reduce overall X-ray dose on the sample, resulted in bubble formation rates slightly less than those of the water standard. As observed previously, the intermittent scanning approach resulted in an order of magnitude reduction in bubble formation, and was thus, found to be the preferred approach. This is illustrated via the lower volume of bubbles observed in Fig. 3-3e (intermittent) relative to 3f (continuous), and also by the less steep bubble volume versus time slope in Fig. 3-3 (centre) between the intermittent (d-e) and continuous (e-f) approaches.

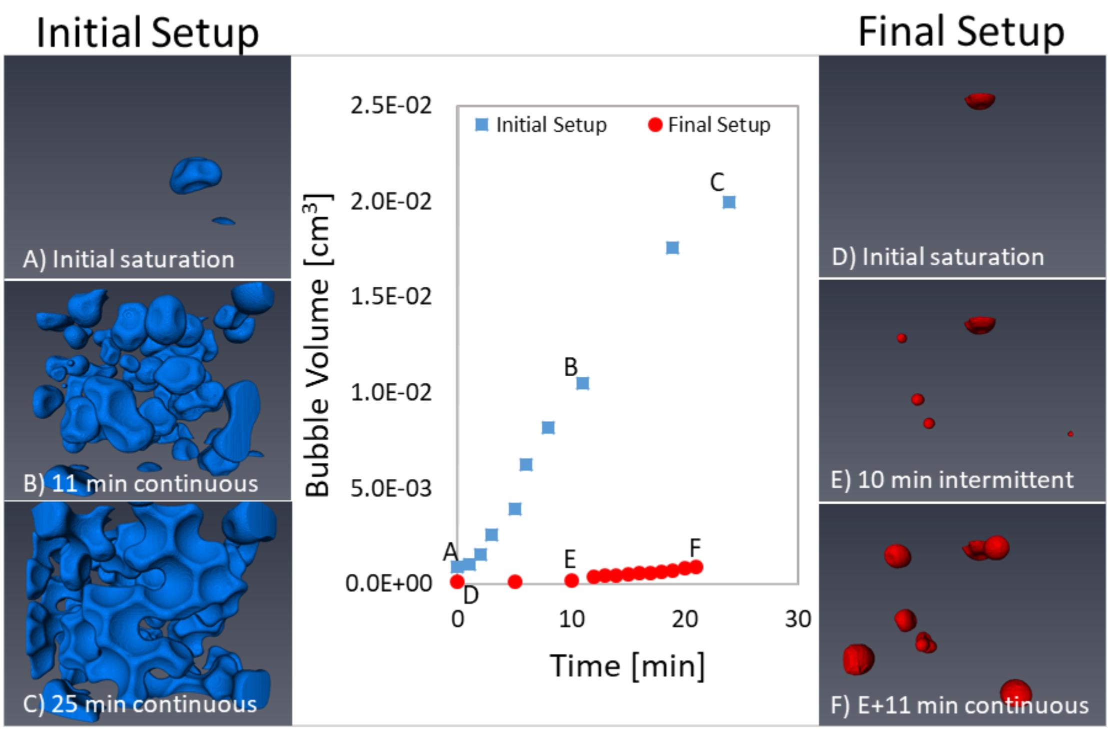

Figure 3-3. (center) Volume of bubbles formed during x-ray exposure for the initial and final pink beam setups. (a) Trapped air prior to the initial pink beam experiment, (b) after 11 min of continuous radiation exposure and (c) 25 min of continuous exposure. (d) Trapped air prior to the final pink beam experiment, (e) after 10 min of intermittent exposure, followed by (f) 11 min of continuous exposure.

In summary, there is a major reduction in bubble formation between the initial (1 mm Ti, 2 mrad, continuous scanning) and final (1 mm Cu, 1.5 mrad, intermittent scanning) pink-beam setups, as illustrated by comparison of Figs. 3-3b and 3-3e, respectively. The final setup produced only a few tiny bubbles (Fig. 3-3e) after 10 minutes of scanning that do not fill pores in the porous media and, therefore, will have a negligible effect on the flow paths within the system.

It should also be noted that these tests were conducted on a static sample being exposed to an X-ray dose. However, during an actual fluid-flow experiment, the fluid phase would be slowly moving through the FOV, thereby transporting some of the free radicals produced out of the beam and most likely reducing the likelihood of bubble nucleation beyond what was observed under the conditions presented here

3.4.2 Optimizing image quality and acquisition time

Having settled on pink-beam parameters intended to minimize bubble formation, different exposure times were tested to study the resulting effect on image quality and temporal resolution. An image acquisition time of 10–30 seconds allows full volume scans to be collected between changes in fluid configuration during non-equilibrium multiphase flow [Berg et al., 2013]. This relatively fast acquisition time reduces the chance of fluid movement during scanning and, therefore, movement artefacts in the reconstructed images. A 10 milliseconds exposure time (per frame) was tested to collect a full acquisition of 900 projections in approximately 9 seconds. However, at this fast acquisition rate, the SNR is rather poor as illustrated by the broad histogram peak (97.9 ± 230.8) observed for the raw greyscale values of the solid phase (Fig. 3-4). The air (-166.4 ± 176.6) and water (327.7 ± 216.3) peaks (not shown) are also broad, which causes poor separation of the phases and leads to difficulties with subsequent segmentation.

This poor SNR reduces the sharpness of interfaces in the image which affects the accuracy of important multiphase flow measures such as contact angle, interfacial curvature and interfacial area. In Fig. 3-5a, the sharpness of the bubble interface is compromised at a 10 milliseconds exposure, especially at the solid surface compared to 15 and 20 milliseconds exposure times (Figs. 3-5b and c, respectively). Both 15 and 20 milliseconds exposure times have adequate SNR for multiphase measures, but the faster total acquisition time of 14 seconds for the 15 milliseconds exposure time is obviously more desirable than 18 seconds for the 20 milliseconds exposure time.

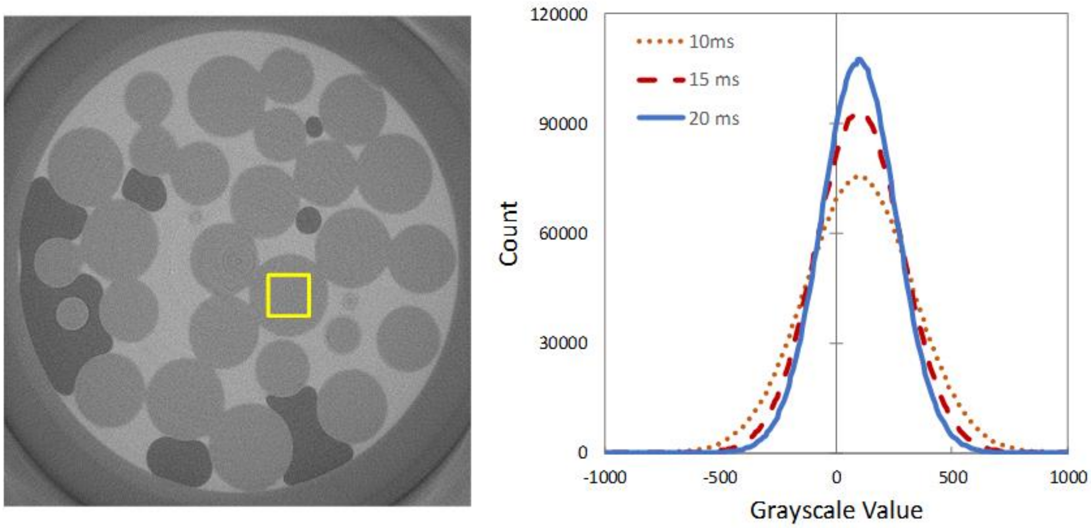

Figure 3-4. (left) A horizontal slice through the sample imaged with a 15 ms exposure time. (right) Histograms collected from the center of a single glass bead (box in left image) for each exposure time as a basis for noise estimation.

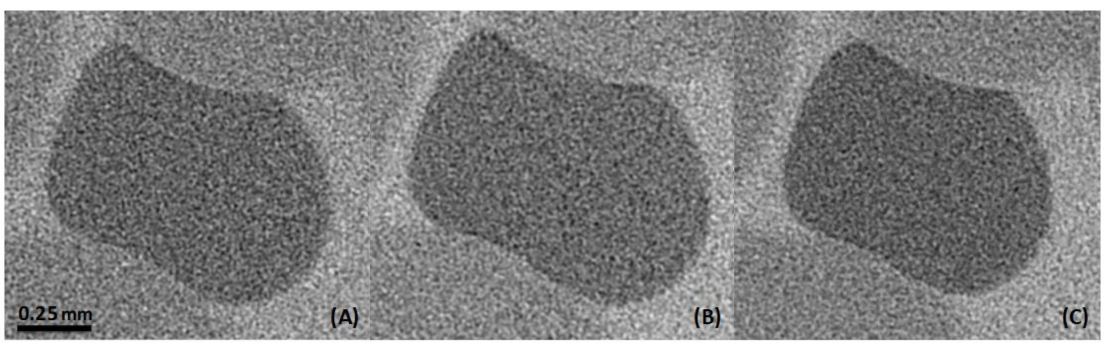

Figure 3-5. A representative trapped bubble for the (A) 10, (B) 15, and (C) 20 ms exposure times.

It should be noted that a high-resolution dry scans of the sample before fluids are introduced, which will generally be necessary to reliably segment the solid phase separately, thereby making it easier to segment the fluid phases in partially saturated images.

The number of projections, n, collected per scan would also have an effect on image quality. Although we did not adjust this parameter in this study, it would have the same effect as it does for a monochromatic beam setup. First, increasing n would fill in missing information in Fourier space until $n = \pi/2 * NX$, where NX is the number of horizontal pixels. Secondly, it would improve the SNR as more X-ray photons are collected with increased number of projections. This noise reduction scales as the square root of the number of projections. It should be noted that although the image quality improves with increased n, the acquisition time also increases. Therefore, it is a question of whether SNR or temporal resolution is more important for the study. In many cases, such as multiphase flow, keeping acquisition time short is more important since it allows for studying non-equilibrium flow phenomena.

3.4.3 Effect of X-ray exposure on wettability within a porous medium

Due to the high X-ray exposure encountered using pink-beam technology, a concern is the potential for wettability change in the system [Brown et al., 2014]. An automatic contact angle measurement code was developed following the approach of Scanziani et al. [2017] to determine whether contact angle, and therefore, the wettability of the system, changes with X-ray exposure. Shown in Fig. 3-6 is the normalized frequency histogram of contact angles for an initially saturated sample (red-dashed), after 25minutes of X-ray exposure (blue-dotted), and 15 minutes after the X-ray exposure (green-solid). The initial contact angle in the system was around 20° which is consistent with a water-wet system. This initial measurement was conducted on the only trapped air pocket in the FOV, causing the distribution to be sparse and most likely attributing to the slight difference from the other curves. The other curves, representing the contact angle distributions after exposure and after relaxation of the system, are nearly identical. If the X-rays were causing wettability alteration in the bead pack, removing the X-rays would allow for some relaxation of this effect as shown in hard X-ray literature [Kwon et al., 2009]. Since this is not seen, it can be concluded that the wettability, and therefore, the physics of the system, is not being significantly changed by the X-ray exposure, at least not in the case of the two fluids used here (air and KI-doped water).

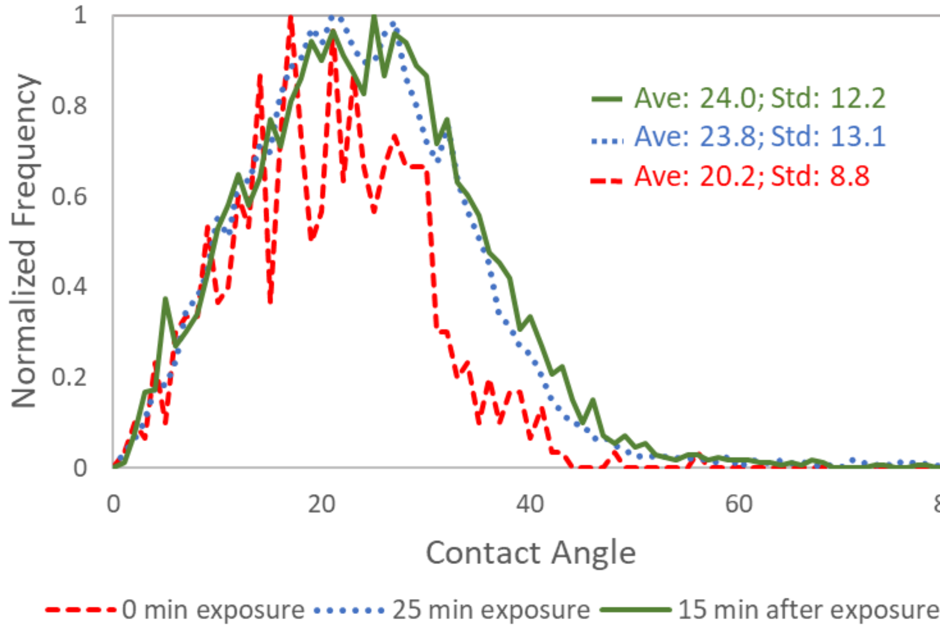

Figure 3-6. Normalized frequency of contact angle measurements for the final pink-beam setup at 0 min of exposure, after 25 min of continuous exposure, and following 15 min of shutdown after the 25 min exposure.

3.5 Conclusions

Fast µCT provides unprecedented access for multiphase flow studies to track moving, and evolving, fluid interfaces in 3D pore space. Interfacial dynamics can now be studied in porous media and the findings used to better inform and evaluate multiphase theories. While a few beamlines specifically designed for monochromatic fast µCT exist, we present a pink-beam technique that can be utilized more broadly, and we tested that the high-flux pink-beam does not affect the physics of multiphase flow. By reducing the low energy X-rays with a 1-mm Cu filter and the overall X-ray flux with a 1.5 mrad Pt mirror angle, bubble formation, due to X-ray exposure on time scales relevant to multiphase flow experiments, was successfully mitigated. We found that a 15 milliseconds camera exposure time provided adequate contrast and image quality to measure multiphase quantities, such as contact angle and interfacial curvature, resulting in a full-scan acquisition time of 14 seconds. A contact angle analysis was performed and it was concluded that pink beam in the suggested configuration does not affect the wettability of the porous medium.

3.6 Acknowledgements

This work was supported by the U.S. National Science Foundation, Hydrologic Sciences Program under award #1344877. This work was performed at GeoSoilEnviroCARS (The University of Chicago, Sector 13), Advanced Photon Source (APS), Argonne National Laboratory. GeoSoilEnviroCARS is supported by the National Science Foundation—Earth Sciences (EAR - 1634415) and Department of Energy—GeoSciences (DE-FG02-94ER14466). This research used resources of the Advanced Photon Source, a U.S. Department of Energy (DOE) Office of Science User Facility operated for the DOE Office of Science by Argonne National Laboratory under Contract No. DE-AC02-06CH11357.

Chapter 4. Exploring the Effect of Flow Condition on the Constitutive Relationships for Two-Phase Flow

Douglas E. Meisenheimer[1], James E. McClure[2], Mark L. Rivers[3] and Dorthe Wildenschild[1]

1. School of Chemical, Biological, and Environmental Engineering, Oregon State University, Corvallis, Oregon, U.S.A.

2. Advanced Research Computing, Virginia Polytechnic Institute and State University, Blacksburg, Virginia, United States

3. Department of Geophysical Sciences and Center for Advanced Radiation Sources, The University of Chicago, Chicago, Illinois, U.S.A.

Advances in Water Resources, Elsevier Ltd.
The Boulevard, Langford Lane, Kidlington, Oxford OX5 1GB, UK
Volume 137
https://doi.org/10.1016/j.advwatres.2020.103506

4.1 Abstract

Empirical relationships that describe two-phase flow in porous media have been largely hysteretic in nature, thereby requiring different relationships depending on whether the system is undergoing drainage or imbibition. Recent studies have suggested using interfacial area to close the well-known capillary pressure-saturation relationship, while others expand upon this by including the Euler characteristic for a geometric description of the system. With the advancement of fast x-ray microtomography at synchrotron facilities, three-dimensional experiments of two-phase quasi- and non-equilibrium flow experiments were conducted to quantify the uniqueness of constitutive relationships under different flow conditions. We find that the state functions that include the Euler characteristic provide the most unique prediction of the state of the system for both quasi- and non-equilibrium flow. Of these functions, those that infer volume fraction from the other state variables are independent of flow condition (quasi- or non-equilibrium). This enhances the applicability of new constitutive relationships allowing for more robust models of two-phase flow.

4.2 Introduction

Immiscible flow of two fluids in porous media occurs in many environmental and industrial applications. Some two-phase flow processes in the environment include: groundwater remediation, enhanced oil recovery, and geologic carbon sequestration; whereas industrial applications include, among others: fluid separation in fuel cells, the adsorption of liquids in absorbing materials, and the drying of porous products such as paper pulp and building materials. The societal, economic, and environmental impacts of these systems require well-informed two-phase flow theories and mathematical models to predict the underlying processes.

Traditionally, practitioners have relied on empirical relationships between macroscopic capillary pressure (P_c) and wetting phase saturation (S_w) to model two-phase systems, defining capillary pressure as:

$$P_n - P_w = P_c(S_w) \tag{4.1}$$

where P_n is the average non-wetting phase pressure for the system and P_w is the average wetting phase pressure. This relationship assumes that P_c is solely a function of saturation, while processes that affect fluid distribution such as porous medium wettability, fluid-fluid interfacial configuration, and pore morphology are not accounted.

The $P_c(S_w)$ relationship is well known to exhibit hysteretic behavior, i.e. the relationship is process and history dependent, and therefore separate functions are needed depending on whether the system is undergoing drainage or imbibition. It has been proposed that a geometric description of the system needs to be included to uniquely describe two-phase flow systems. Hassanizadeh and Gray [1990, 1993] suggested that specific interfacial area between the wetting and non-wetting phases (a_{nw}), accounts for variations in fluid configurations that can be present in a porous medium. They proposed that when taking into account interfacial area in the constitutive equations, such that $P_c = P_c(S_w, a_{nw})$, the drainage and imbibition $P_c(S_w, a_{nw})$ relationships would fall on a unique surface, i.e. the expanded relationship would be non-hysteretic and a single relationship could describe the state of the system.

There has been a concerted effort to validate this theory both numerically and experimentally. Micromodel [Chen et al., 2007; Cheng et al., 2004; Karadimitriou et al., 2013; Pyrak-Nolte et al., 2008] and microtomography imaging experiments [Porter et al., 2010] have shown that the $P_c(S_w, a_{nw})$ relationship is unique, within experimental error, under quasi-equilibrium flow conditions. Similar results were obtained numerically via pore-network modeling [Held & Celia, 2001; Joekar-Niasar & Hassanizadeh, 2011; Joekar-Niasar et al., 2008; Reeves & Celia, 1996] and a Lattice-Boltzmann model [Porter et al., 2009]. However, a lingering question is whether these observations hold true under non-equilibrium flow conditions.

Non-equilibrium flow is a generic term that can cover a broad spectrum of flow in porous media. Most prominently, the term is associated with dynamic or transient flow, being effectively reserved for flow with capillary numbers outside of the capillary fingering regime in terms of the Lenormand phase-diagram [Lenormand et al., 1988]. An important facet of non-equilibrium flow is the resulting absence of interfacial relaxation towards equilibrium, which then affects macroscopic invariants such as saturation, average capillary pressure, and specific interfacial area [Gray et al., 2015; Schlüter et al., 2017]. In this research, we use the term non-equilibrium flow for flow experiments that do not allow for interfacial relaxation during drainage/imbibition cycles, rather than the terms *dynamic* or *transient* which connote higher capillary number flows.

Some effort has been made to study the uniqueness of the $P_c(S_w, a_{nw})$ relationship under transient vs. quasi-equilibrium conditions in micromodels [Godinez-Brizuela et al., 2017; Karadimitriou et al., 2014] and using simulations via dynamic pore-network modeling [Joekar-Niasar & Hassanizadeh, 2012]. The dynamic pore-network model found some differences between the transient and quasi-equilibrium $P_c(S_w, a_{nw})$ surfaces, but determined that the differences were negligible. The micromodel studies, on the other hand, showed that the transient and quasi-equilibrium $P_c(S_w, a_{nw})$ surfaces were statistically different. To our knowledge, no published research exists that compares the $P_c(S_w, a_{nw})$ relationship under quasi- and non-equilibrium conditions for a fully three-dimensional experimental system.

An assumption underlying the original theory behind the $P_c(S_w, a_{nw})$ relationship [Hassanizadeh & Gray, 1990] is that each fluid phase is continuous, but in most circumstances this condition is not met in two-phase flow systems. Therefore, other state variables have been investigated that can describe connectivity and shape of the fluids, such as fluid topology [Herring et al., 2013; McClure et al., 2016; Schlüter et al., 2016]. The Euler characteristic of the non-wetting phase (χ_n) has been used as the standard to measure the connectedness of fluid configurations. Schlüter et al. [2016] showed that the Euler characteristic conveys complementary information that helps explain the hysteresis present in the $a_{nw}(S_w)$ relationship. Using lattice Boltzmann model simulations, McClure et al. further demonstrated that the inclusion of χ_n in a non-dimensionalized $P_c(S_w, a_{nw})$ relationship removes nearly all hysteresis under equilibrium [2016, 2018] and dynamic [2018] conditions.

The ability to visualize non-equilibrium multi-phase flow in three-dimensional porous media has not been possible until very recently. With the improvements in imaging hardware (detector speed and sensitivity), along with increased x-ray brilliance capabilities at synchrotron sources, x-ray computed microtomography (μCT) has become a viable technology to meet this need. Berg et al. [2013] and Youssef et al. [2013] were among the first to investigate two-phase flow using fast μCT. Berg et al. determined that a time resolution between 10 and 30 s was sufficient to capture differences in fluid front configurations surrounding a Haines jump during two-phase flow. Youssef et al. used the technique to determine that saturation of a sandstone followed a linear dependence on the square root of time, thereby validating the Washburn equation with real-time three-dimensional data. Since these initial forays into fast μCT there has been a variety of studies looking at drainage and/or imbibition processes of two-phase flow [Andrew et al., 2015; Armstrong et al., 2014; Berg et al., 2016; Leu et al., 2014; Schlüter et al., 2016; Singh et al., 2017]. Schlüter et al. [2016] did collect three-dimensional experimental data of a time-resolved two-phase flow experiment and determined that the $P_c(S_w, a_{nw})$ relationship was unique in the supporting information, however, they used external pressure transducer readings (rather than P_c determined from internal interfacial curvature measurements) to establish their $P_c(S_w, a_{nw})$ curves. Scanning curves, imbibitions and drainages that start at intermediate wetting saturations, were not collected in the study resulting in an absence of data points that provide information about the space between the hysteretic main $P_c(S_w)$ loop.

The objective of this study was to generate experimental three-dimensional quasi- and non-equilibrium two-phase datasets using fast microtomography to compare an array of state variable constitutive relationships and assess whether any are unique under either flow condition, thus determining if a single relationship can describe the state of a system independent of flow condition.

4.3 Materials and Methods

4.3.1 Experimental setup

Soda-lime glass beads (0.8–1.2 mm) were randomly packed and sintered into a borosilicate glass column (6 mm diameter, 26 mm height) as a simplified porous medium for both two-phase flow experiments. The porosity (ϕ) for the quasi- and non-equilibrium experiments were 0.39 and 0.37, respectively. The glass bead columns were contained in a sample holder which was mounted on the x-ray µCT rotation stage during flow experiments and image acquisition.

The bottom of the sample holder was connected to a Harvard Apparatus PhD 2000 precision syringe pump, controlling fluid volumes and flow rates. The pump directly controlled the flow of the wetting phase (water), inducing the flow of the non-wetting phase (air). The wetting phase was a 1:6 solution by mass of potassium iodide (KI) to deionized water. KI is used as a contrast agent for better differentiation between the fluid phases in x-ray images. A hydrophilic nylon membrane (1.2 µm pore size) compressed between two O-rings was used at the bottom of the setup to seal the system and to reach low water saturation within the column. A pressure transducer (Validyne P55 differential pressure transducer) was inserted in the water line below the porous medium to track the differential pressure between the fluid phases for comparison to capillary pressures calculated from image analysis. Differential pressure was measured from the top of the porous medium as the pressure difference between the atmosphere and the bulk wetting phase. The top of the sample was open to the atmosphere through a long (~2 m) Tygon tube to prevent evaporation within the column during lengthy experiments.

4.3.2 Fast X-ray computed microtomography

All experiments were performed using synchrotron radiation at the 13-BMD beamline at the Advanced Photon Source (APS) located at Argonne National Laboratory in Lemont, IL. The fast microtomography method at 13-BMD uses pink beam rather than the more standard monochromatic beam method. Pink beam is produced by filtering the low and high x-ray energies from the full-spectrum white beam that is produced by a synchrotron. A 1.0 mm copper (Cu) filter was used to filter out the low energy x-rays. The high-energy x-rays were removed by reflecting the beam from a platinum (Pt) mirror angled at 1.5 mrad towards the experimental setup.

All scans were collected with a 12-bit CMOS camera with a resolution of 1920 × 1200 pixels, a Nikon macro lens, and a lutetium aluminum garnet scintillator. The pixel size on the sample was 3.2 µm. Each scan consists of a 180° rotation of the sample with two-dimensional radiographic projections taken at 900 angles. The exposure time of each projection was 15 ms, corresponding to an acquisition time of 13.5 s for a volumetric image. Ten flat-field scans (radiographs without the sample present) were acquired before and after the scan for white-field correction. To unwind all fluid lines, the sample was rotated back to 0° after each scan before another scan was initiated. Allowing for scan time, flat-field acquisitions, and sample rotation, the temporal resolution between each data point using pink beam was 50 s. The x-ray beam was turned off when images were not being acquired to reduce x-ray exposure.

4.3.3 Two-phase flow experiments

4.3.3.1 Quasi-equilibrium flow experiment

The quasi-equilibrium flow experiment was carried out using flow conditions similar to previous µCT fluid flow experiments [e.g. Culligan et al., 2004; Porter et al., 2010], but x-ray images were acquired throughout the experiment rather than just at each quasi-equilibrium point (where the pump was stopped and the fluids were allowed to relax towards equilibrium). Before the wetting phase was introduced to the glass bead column, a dry scan was acquired to facilitate easy separation of the solid phase from the fluid phases in the partially saturated images. The dry porous medium was initially saturated with wetting phase at a rate of 5 mL/hr, fully saturating the field of view (FOV). After saturation, a full cycle of primary drainage (PD), main imbibition (MI), main drainage (MD), and three scanning curves (two starting on the MI curve and one on the MD curve) were executed at a flow rate of 0.2 mL/hr. The scanning curves (SI1, SI2, SD1) were used to help fill in the area between the main imbibition/drainage $P_c(S_w)$ loop. The capillary number (Ca) for this flow rate was 2×10^{-7}, which is indicative of a capillary-dominated flow regime. Flow was stopped at different saturation points along each drainage and imbibition curve, corresponding to a change of ~10% in saturation, where the fluids were allowed to relax towards hydrostatic equilibrium before flow was reinitiated. Scans were also acquired during this relaxation period to study how interfaces relax towards equilibrium. Although relaxation occurs over multiple hours [Gray et al., 2015; Schlüter et al., 2017], the majority of saturation change occurs within the first few minutes. To be able to compare with other quasi-equilibrium experiments [e.g. Culligan et al., 2004; Porter et al., 2010] each quasi-equilibrium point was allowed about 15 min for relaxation. Fig. 4-1 shows an example of how the fluid-fluid interfaces retract during this relaxation period.

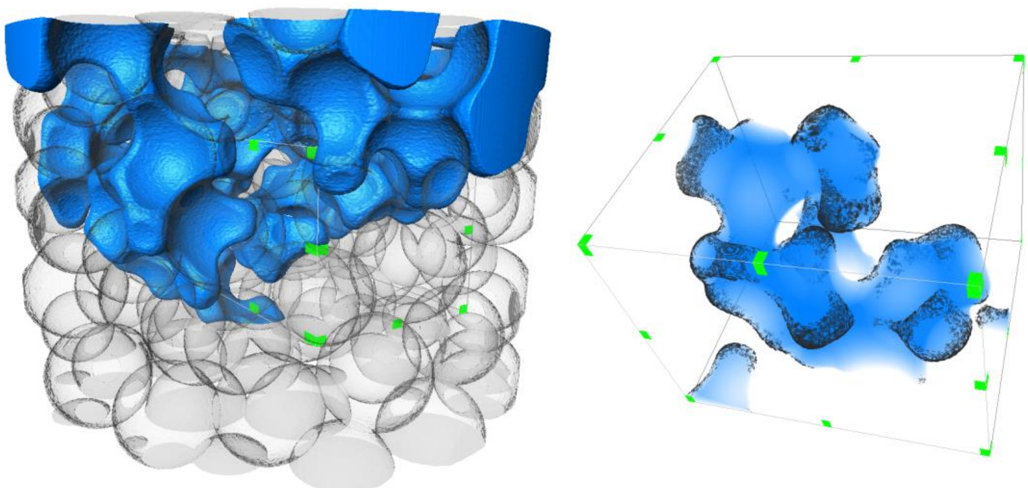

Figure 4-1. (left) Volume rendering of the non-wetting phase in the experimental column during drainage. (right) Subvolume of the rendered non-wetting phase with darkened surfaces representing the magnitude of retraction after 15 min of interface relaxation.

4.3.3.2 Non-equilibrium flow experiment

The non-equilibrium flow experiment was performed in a similarly prepared glass bead column using the same flow rate (Ca = 2×10^{-7}). PD, MI, MD and three scanning curves were collected with image acquisition occurring throughout the experiment. The only difference from the quasi-equilibrium flow experiments was that the pump was only stopped at the end of each (drainage/imbibition) branch, therefore the fluids did not relax during any of the drainage or imbibition experiments.

4.3.4 Image processing

The x-ray projections of each scan were reconstructed into a three-dimensional image with the tomoRecon software based on Gridrec [Rivers, 2012]. Although there is a ring artifact removal step in the reconstruction algorithm which can handle small artifacts associated with the detector, some high frequency ring artifacts, associated with pink beam imaging, remain. These large ring artifacts cause problems during image segmentation as phantom fluid phases are created near the ring artifacts, leading to errors during state variable calculation. These artifacts are attributable to defects in the Pt mirror that is used to filter the high-energy x-rays. Details of the method used to remove high frequency ring artifacts is included in the supporting information, Fig. 4-6.

The images were denoised using a non-local means filter [Buades et al., 2005]. This efficiently denoises the image while preserving image features such as fluid-fluid interfaces, which are important for accurate calculation of specific interfacial area and capillary pressure from image-derived fluid curvatures. All images were aligned to the dry scan acquired before the fluid flow experiment using automatic image registration. The three phases (wetting, non-wetting, solid) in each image where separated using a watershed segmentation [Beucher & Lantuejoul, 1979]. Fig. 4-1 shows a volume rendering of the segmented non-wetting phase in the glass bead column during drainage. From the segmented image, three-dimensional isosurfaces were generated using a marching-cubes algorithm [Lorensen & Cline, 1987] between each phase so that specific interfacial area could be calculated from the images. We adopted the surface smoothing approach (constrained smoothing, smoothing extent = 3) of Li et al. [2018]. For images with similar voxel resolution, they found that these smoothing parameters preserved the original data while achieving the necessary level of smoothing of the interfaces.

Ring artifact removal was performed using ImageJ, but the remaining image processing steps were completed using Avizo™.

4.3.5 Data processing

4.3.5.1 Porosity, saturation and specific interfacial area

Porosity and saturation values were calculated by counting the number of voxels present for each phase in the segmented images. The fluid phases were further separated into connected and disconnected volumes to distinguish the bulk phases for comparison with external pressure transducer measurements. It was assumed that the wetting phase regions connected to the bottom of the FOV and the non-wetting phase regions connected to the top of the FOV represented the bulk phases. Because the outlets of the column were outside of the FOV, it should be noted that these criteria do not guarantee that the identified regions are actually connected to the bulk phases, especially at low saturations.

Isosurfaces between the fluid phases were generated using a marching-cubes algorithm in Avizo™, and total fluid-fluid interfacial area (A_{nw}) was calculated by measuring the total surface area of the triangles comprising those isosurfaces. Specific fluid-fluid interfacial area (a_{nw}) was then calculated by dividing A_{nw} by the total volume. A representative elementary volume (REV) analysis for a subset of saturation and specific interfacial area values are presented in the supporting information, Fig. 4-7. The analysis shows that the parameters stabilize towards the total FOV volume, as reported in similar porous media studies [e.g. Porter et al., 2010; Schlüter et al., 2016].

4.3.5.2 Mean curvature and capillary pressure

Average mean curvature, J_{nw}, was calculated using a modified method of Li et al. [2018]. This involves surface modification (removal of triangles in close proximity to the solid surface). Various studies [Herring et al., 2017; Li et al., 2018; Singh et al., 2017] have reported that surface modification was required to improve curvature estimation from microtomography images due to partial volume effects near the three-phase contact line at the solid surface. Following the methodology of Li et al., a distance threshold, D_{min}, was set to 20% of the maximum distance between a point on the fluid-fluid surface and the nearest point on a solid surface. The mean curvature of each remaining triangle (J_l) for every feature, i, was then weighted by its distance to the solid surface (D_l) assigning more weight to triangles further away and less likely to be affected by the solid surface (Eq. (2)). Pore scale capillary pressure, pic, is calculated using the Young-Laplace equation (Eq. (3)) where the interfacial tension between the fluid phases, σ, is 0.072 N/m. Each feature can then be weighted by its interfacial area (A_{nw}) [Godinez-Brizuela et al., 2017; McClure et al., 2016] to determine the macroscopic average capillary pressure of the system (P_c):

$$J_i = \frac{\sum_l^N J_l D_l}{\sum_i^N D_l} \ for \ D_l > D_{min} \tag{4.2}$$

$$p_i^c = 2 J_i \sigma \tag{4.3}$$

$$P_c = \frac{\sum_i^N p_i^c A_i^{nw}}{\sum_i^N A_i^{nw}} \tag{4.4}$$

In the supporting information, Fig. 4-8, the average capillary pressure of the connected fluid phases is compared to the pressure differential measured from external pressure transducers. This has previously been used as a basis for the verification of the curvature measurement [Li et al., 2018; Schlüter et al., 2017] as the connected phases should equilibrate to the bulk fluid pressures and, therefore, be equal to the pressure differential measured by the external pressure transducers for the quasi-equilibrium case. Although the capillary pressure of the boundary connected fluids has generally been used in previous quasi-equilibrium experimental studies, these pressures do not necessarily represent the system under non-equilibrium flow conditions or, more broadly, under dynamic conditions for higher capillary numbers due to non-equilibrium capillarity effects [Hassanizadeh et al., 2002]. These pressure measurements do not include disconnected fluids that contribute to measures of other state variables (e.g. saturation) which may suggest that they are measured in a fundamentally inconsistent way [McClure et al., 2016]. One cannot neglect the disconnected fluid regions without also neglecting the associated internal energy and any definition for the macroscopic average pressure must respect this in order to develop models that conserve energy. This study instead uses the area-weighted average curvature and capillary pressure of all fluid interfaces, which is consistent with other studies testing two-phase flow constitutive relationships [e.g. Godinez-Brizuela et al., 2017; Joekar-Niasar & Hassanizadeh, 2012; McClure et al., 2016].

4.3.5.3 Euler characteristic

The Euler characteristic (χ) is a topological invariant that describes the connectivity of a fluid phase. It is described by the following relationship:

$$\chi = \beta_0 - \beta_1 + \beta_2 \tag{4.5}$$

where β_0 is the number of distinct regions of the fluid phase, β_1 is the number of redundant connections within each distinct region, and β_2 is the number of encapsulated voids in each region. The β_2 value for the non-wetting phase can be neglected in this study since an element of water or solid could not be completely suspended in air. Fundamentally, the Euler characteristic quantifies the entrapment of fluids and the breaking up of fluid connections through pore throats due to snap-off. This phenomenon has been established as an important source of hysteresis in multi-phase flow [Held & Celia, 2001; Joekar-Niasar et al., 2013; Schlüter et al., 2016], which makes the Euler characteristic an interesting state variable to consider in constitutive relationships [McClure et al., 2018; Schlüter et al., 2016].

4.3.5.4 Constitutive state variable relationships

The constitutive relationships we are studying are based on a generalized form of the Minkowski Steiner formula [Federer, 1959; McClure et al., 2018]:

$$dV_n = c_1 A_n dr + c_2 J_n (dr)^2 + c_3 \chi_n (dr)^3 \tag{4.6}$$

where c_i are coefficients determined by the shape of the non-wetting phase domain and dr is the radius of a small ball. The state variables are extensive and therefore it is useful to divide the entire equation by the total volume, V. Thus, Eq. (4.6) provides a geometric state relationship that describes a change in volume of the non-wetting phase in terms of the invariant properties of the boundaries of a phase: surface area (A_n), mean curvature (J_n), and Euler characteristic (χ_n). The state variables can also be non-dimensionalized (i.e. $\acute{a}_n, \acute{J}_n, \acute{\chi}_n$) using the Sauter mean diameter, $D = 6\phi/\,(a_{ns} + a_{ws})$, as a reference length scale; where a_{ns} and a_{ws} are the specific interfacial areas between the non-wetting/solid surfaces and the wetting/solid surfaces, respectively [McClure et al., 2018]. Non-dimensionalization is important for spline approximation of constitutive relationships (Section 4.3.5.5) because the state variables will then tend to range between [0,1], thereby removing any weighting factors that would affect minimization of the residuals between the observed data and the spline fit.

McClure et al. utilized a modified form of Eq. (4.6) to predict the mean curvature of the system, $\acute{J}_{\mathrm{nw}}(S_w, \acute{a}_{nw}, \acute{\chi}_n)$, using geometric measures available in thermodynamically constrained averaging theory (TCAT) models. We will analyze the same relationship, including lower-dimensional variations, but relationships more closely represented by Eq. (4.6), $S_w(\acute{a}_{nw}, \acute{J}_{\mathrm{nw}}, \acute{\chi}_n)$ and $V_n(\acute{a}_{nw}, \acute{J}_{\mathrm{nw}}, \acute{\chi}_n)$, will also be considered as it is hypothesized that these relationships can more accurately predict the state of the system. The $V_n(\acute{a}_{nw}, \acute{J}_{\mathrm{nw}}, \acute{\chi}_n)$ relationship should provide the best description of the system because V_n is not specific to a porous medium unlike saturation which is based on porosity.

4.3.5.5 Estimating hysteresis with generalized additive models (GAMs)

The hysteresis of a constitutive relationship is evaluated using generalized additive models (GAMs) to fit locally-smooth spline surfaces to the constitutive relationships and evaluating the associated error [McClure et al., 2016, 2018; Wood & Shaw, 2015], which is attributed to the degree of hysteresis associated with the relationship. Two different error measures are evaluated for each GAM to assess the uniqueness of each model. The generalized cross-validation (GCV) value represents the error of the GAM in predicting each data point if it was not included in the construction of the GAM [Golub et al., 1979]; therefore, as GCV approaches zero the GAM predicts the data better. The coefficient of determination, R^2, measures the proportion of variance in the data that is predicted by the GAM where a value of 1.0 would indicate a perfect fit. GCV and R^2 values were calculated for both the quasi- and non-equilibrium data sets as well as for all the data combined to determine whether the constitutive relationships are unique with respect to fluid flow condition.

4.4 Results and Discussion

We will first quantify the effect of the inclusion of additional state variables in constitutive relationships on GAM fitting for the quasi- and non-equilibrium flow experiments separately. Secondly, we will evaluate whether a single constitutive relationship can uniquely describe two-phase flow independent of flow condition.

4.4.1 State variable effect on hysteresis: quasi-equilibrium flow

First, the uniqueness of the two-variable constitutive relationships of state variables ($\acute{J}_{\mathrm{nw}}$, $\acute{a}_{nw}$, $\acute{\chi}_n$) as a function of saturation for the quasi-equilibrium case will be assessed. Three- and four-variable relationships will also be evaluated to determine whether including additional state variables will better predict the state of the system for quasi-equilibrium flow.

The conventional hysteretic $P_c(S_w)$ relationship is observed for the quasi-equilibrium flow experiments (Fig. 4-2a). When the system is allowed to relax towards equilibrium, the capillary pressures tend towards the center of the area bounded by the main imbibition (MI) and main drainage (MD) data. Schlüter et al. [2017] observed similar trends when pressures decreased toward the quasi-equilibrium imbibition curve after fast drainage. When flow is reinitiated following a relaxation point, the capillary pressure rapidly returns to its value before relaxation began.

This hysteretic behavior is significantly reduced in the $a_{nw}(S_w)$ relationship with imbibition located only slightly above drainage (Fig. 4-2b). Interestingly, the reverse has been observed in many glass bead pack oil-water [Porter et al., 2010; Schlüter et al., 2016] and air-water [Culligan et al., 2004] experiments. Yet, many pore-scale models [e.g. Held & Celia, 2001; Joekar-Niasar et al., 2008] of glass bead systems predict that imbibition should fall above drainage, corroborating observations reported here. It is unclear what is causing this discrepancy in fairly similar glass bead systems.

The $\chi_n(S_w)$ relationship is also highly hysteretic (Fig. 4-2c) due to different fluid displacement mechanisms controlling drainage and imbibition. Schlüter et

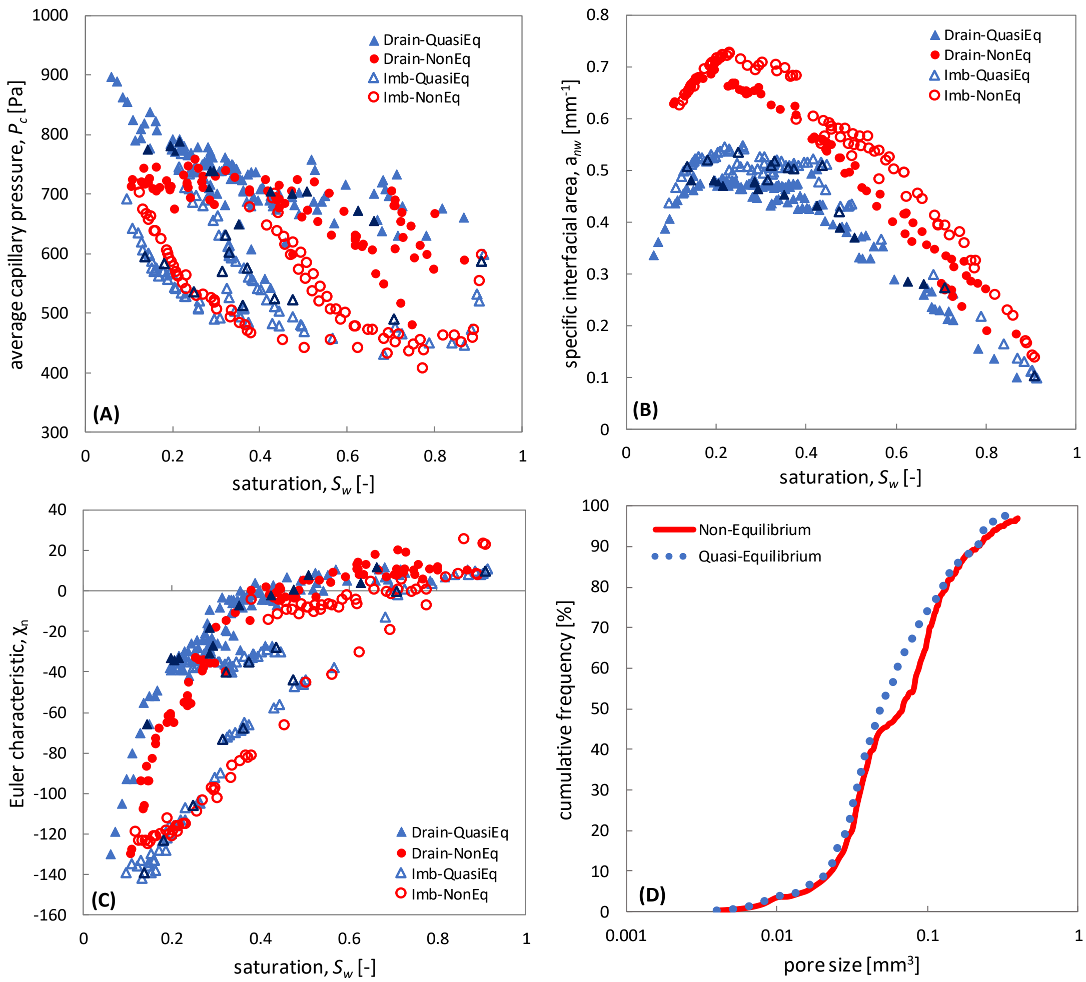

Figure 4-2. (a) Capillary pressure, P_c, as a function of saturation, S_w, for the quasi- and non-equilibrium flow experiments. (b) Specific interfacial area, a_{nw}, as a function of S_w. (c) Euler characteristic, χ_n, as a function of S_w. (d) Cumulative pore size distribution of the porous media.

al. [2016] presented the concept that the $\hat{\chi}_n(\mathrm{Sn})$ relationship follows a power law relation of the form:

$$\hat{\chi}_n = pS_n^i + \epsilon \tag{4.7}$$

where $\hat{\chi}_n$ is the Euler characteristic normalized to the χ_n at 100% non-wetting phase saturation, p and ε are free parameters, and i is the characteristic slope of the relationship. They hypothesized that the characteristic slope is indicative of the fluid displacement mechanism of the system. The normalized Euler characteristic is plotted as a function of non-wetting saturation in Fig. 4-3a with each drainage and imbibition curve fitted to Eq. (4.7). The characteristic slopes of both drainage and imbibition fall within the same ranges presented by Schlüter et al. [2016] for a variety of datasets in different porous media and with different fluid pairs.

Interestingly, when $\hat{\chi}_n$ is plotted against trapped wetting saturation ($S_{w,t}$) there is a nearly linear dependence with very little separation of the drainage and imbibition curves (Fig. 4-3b). This absence of hysteresis was also observed in oil-water data [Schlüter et al., 2016] and is most likely attributable to the causal relation between the production of trapped wetting pendular rings and the invasion of non-wetting phase.

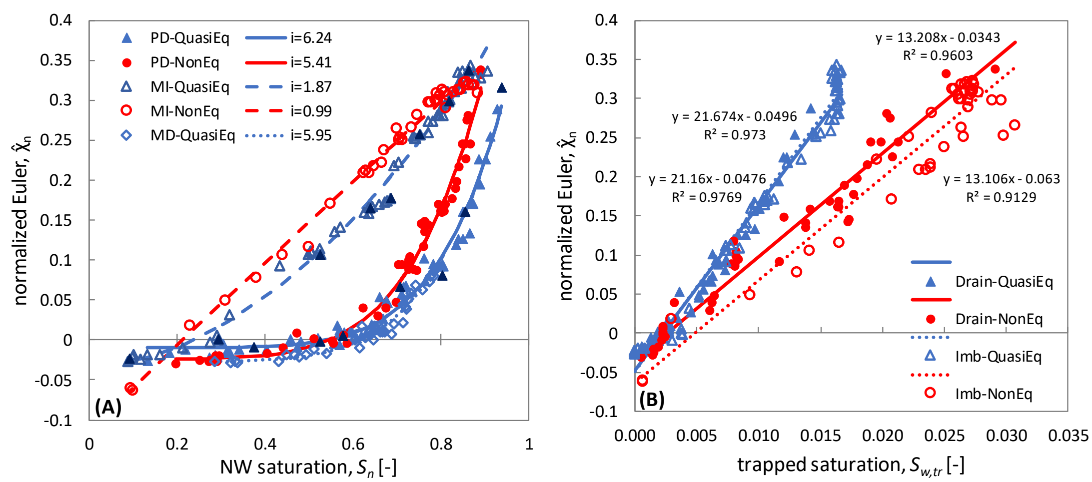

Figure 4-3. (a) Normalized Euler characteristic $\hat{\chi}_n$ as a function of non-wetting saturation S_n with each drainage and imbibition power law fitted to classify the fluid displacement mechanism of the experiment. (b) $\hat{\chi}_n$ as a function of trapped-wetting saturation $S_{w,t}$ with linear fits to the drainage and imbibition data. Bolded points are the quasi-equilibrium relaxation points.

The uniqueness of these two-variable relationships are quantified by fitting GAMs to them and determining the error associated with these fits (Fig. 4-4). As a reminder, curvature ($\acute{J}_{nw}$) is used rather than capillary pressure to keep non-dimensionalization of the state variables consistent. The $\acute{J}_{nw}(S_w)$ relationship exhibits large error values with a GCV of 0.15 and R^2 of 0.14, which is indicative of significant hysteresis in the relationship, as observed in Fig. 4-3a. Also unsurprisingly, the $\acute{\chi}_n(S_n)$ relationship has large error values (GCV = 0.0023 and R^2 = 0.62) due to the difference in displacement mechanisms between drainage and imbibition. The $\acute{a}_{nw}(S_w)$ relationship exhibits a much better fit with a low GCV value (0.00032) and high R^2 value (0.91) indicating that hysteresis is significantly reduced. Interestingly, the $\acute{\chi}_n(S_{w,t})$ relationship offers a statistically quite unique solution (GCV = $8.2 \cdot 10^{-5}$; R^2 = 0.99). This simple relationship could be useful for experimental and numerical datasets because measuring saturation and Euler characteristic (a function of the location of saturation) is much less demanding than measuring P_c and a_{nw} which requires surface generation, though in field-scale P_c is much more easily measured and interpreted.

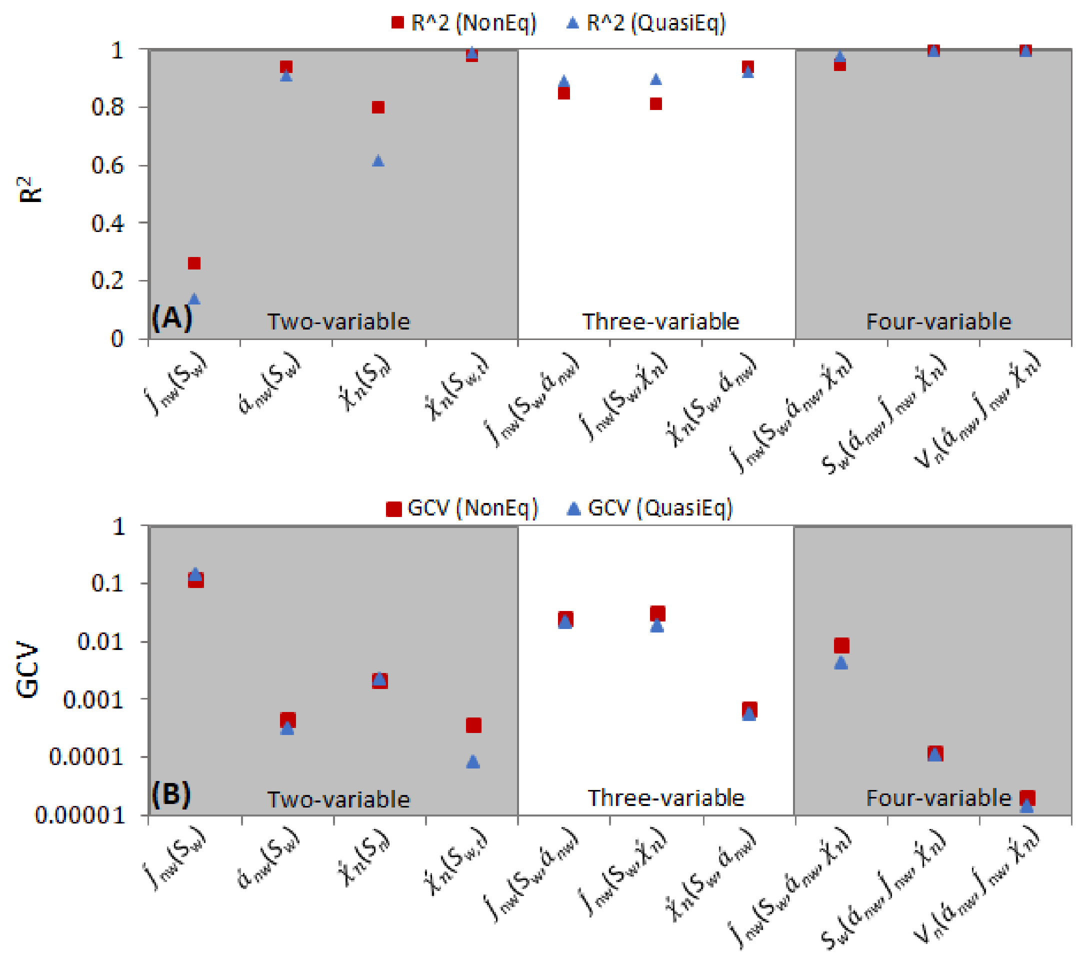

Figure 4-4. Associated errors for GAM fits to two-, three-, and four-variable relationships. Quasi- and non-equilibrium are shown for both R^2 (a) and GCV (b) error values. A large R^2 and small GCV value indicates a better fit.

Similarly to the two-variable constitutive relationships, hysteresis in the three-variable relationships was investigated by measuring the error values of the GAMs fits (Fig. 4-4) in order to assess whether the inclusion of another state variable would result in a less hysteretic relationship. Unlike the two-variable relationships, no combination of the state variables ($\acute{J}_{nw}(S_w, \acute{a}_{nw})$, $\acute{J}_{nw}(S_w, \acute{\chi}_n)$, and $\acute{\chi}_n(S_w, \acute{a}_{nw})$) stands out in terms of a significantly greater reduction of hysteresis ($0.00056 \leq GCV \leq 0.022$ and $0.89 \leq R^2 \leq 0.92$). This suggests that each state variable is independent and each combination provides comparable information to describe the system. Although there is an overall improvement in the ability to predict the system over the two-variable relationships, it is difficult to determine whether the measured errors in the relationships are real or could possibly be explained by the relatively limited amount of scanning curve data available to fill in the area between the main drainage and imbibition curves. This is especially true for the drainage surfaces where only one scanning curve dataset was collected for each experiment. But, similar results were reported for large data simulations of a glass bead pack by McClure et al. [2018] with a R^2 value of 0.93 for the $\acute{J}_{nw}(S_w, \acute{a}_{nw})$ relationship. Godinez-Brizuela et al. [2017] also reported a reduction of hysteresis in micromodels for the $P_c(S_w, a_{nw})$ relationship.

Finally, GAMs were fitted to the constitutive relationship between all state variables in order to verify that a higher dimensional relationship would provide a unique prediction of the system. The $\acute{J}_{nw}(S_w, \acute{a}_{nw}, \acute{\chi}_n)$ relationship predicts the state of the system better than the three-variable relationships with a GCV value of 0.0043 and a R^2 value of 0.98. It is expected that errors associated with measuring interfacial area, curvature [Li et al., 2018], and Euler characteristic [Armstrong et al., 2018] of experimental µCT data contributes to the residual variance in the relationship. But, this result suggests that the $\acute{J}_{nw}(S_w, \acute{a}_{nw}, \acute{\chi}_n)$ relationship is unique for the quasi-equilibrium data, a finding corroborated by McClure et al. [2018]. As hypothesized, the $S_w(\acute{a}_{nw}, \acute{J}_{nw}, \acute{\chi}_n)$ and $V_n(\acute{a}_{nw}, \acute{J}_{nw}, \acute{\chi}_n)$ relationships provide even better fits with the latter being the most accurate ($GCV = 1.5 \cdot 10^{-5}$ and $R^2 = 0.998$).

4.4.2 State variable effect on hysteresis: non-equilibrium flow

We observed similar results in the two-variable relationships for non-equilibrium flow as for quasi-equilibrium flow. For ease of comparison, the non-equilibrium data is illustrated along with the quasi-equilibrium data in Fig. 4-2 and in Fig. 4-4 for the GAM fit errors. The non-equilibrium $\acute{J}_{nw}(S_w)$ relationship exhibits the largest magnitude of hysteresis (GCV = 0.12, R^2 = 0.26). The relaxation points of the quasi-equilibrium $P_c(S_w)$ relationship tend to be bounded by the non-equilibrium relationship (Fig. 4-2a), which is expected due to the earlier observation that capillary pressures tend towards the center of the main drainage/imbibition loop when fluids relax towards equilibrium. The quasi-equilibrium $a_{nw}(S_w)$ relationship, on the other hand, is not bounded by the non-equilibrium relationship (Fig. 4-2b). Both experiments have a peak a_{nw} value around S_w = 0.24, but the non-equilibrium interfacial area generation is much greater than the quasi-equilibrium.

Schlüter et al. [2017] reported a reduction of interfacial area during interface relaxation following a fast drainage experiment. It follows that, if the interfaces are allowed to relax multiple times during a quasi-equilibrium flow experiment, the quasi-equilibrium experiment would inherently produce less interfacial area and the $a_{nw}(S_w)$ relationship would fall below the non-equilibrium experiment, as observed here. Significantly more disconnected interfaces are generated in the non-equilibrium experiment than in the quasi-equilibrium experiment (supporting information, Fig. 4-9) as suggested by [Wildenschild et al., 2001, 2005]. When interfaces are not allowed to relax, the system is forced further away from equilibrium and the surface energy of the system does not reduce to its minimum value at that saturation. This increase in disconnected phase is also represented in the $\hat{\chi}_n(S_n)$ relationship (Fig. 4-3a). The normalized Euler number for the non-equilibrium experiment is slightly more negative than the quasi-equilibrium experiment at low non-wetting phase saturations indicating a larger number of disconnected non-wetting phase blobs. The non-equilibrium $\acute{\chi}_n(S_n)$ relationship has relatively large error values (GCV = 0.0021 and R^2 = 0.80) whereas hysteresis is significantly reduced in the $\acute{a}_{nw}(S_w)$ relationship (GCV = 0.00045 and R^2 = 0.94). As with the quasi-equilibrium case, the $\acute{\chi}_n(S_{w,t})$ relationship is quite unique with a GCV of $3.6 \cdot 10^{-5}$ and an R^2 of

0.98. The non-equilibrium $\acute{\chi}_n(S_{w,t})$ relationship has a shallower slope than the quasi-equilibrium (Fig. 4-3a) which is attributable to the increased production of disconnected phases in the non-equilibrium case.

Similarly to the quasi-equilibrium case, no three-variable combination of the state variables stands out in terms of significantly greater reduction of hysteresis than the others ($0.00071 \leq \mathrm{GCV} \leq 0.032$ and $0.85 \leq R^2 \leq 0.94$). Specifically, only 85% of variance in the $\acute{J}_{\mathrm{nw}}(S_{\mathrm{w}}, \acute{a}_{nw})$ relationship is explained. This result contradicts transient studies including 3-dimensional dynamic pore network simulations [Joekar-Niasar & Hassanizadeh, 2012] and two-dimensional micromodel data [Karadimitriou et al., 2014] where the transient $P_c(S_w, a_{nw})$ surface was found to be unique for a given capillary number within specific margins or error.

Finally, the four-variable relationships were investigated for the non-equilibrium flow experiment. Similar to the quasi-equilibrium relationship, the non-equilibrium $\acute{J}_{\mathrm{nw}}(S_w, \acute{a}_{nw}, \acute{\chi}_n)$ relationship predicts the state of the system better than the three-variable relationships with a GCV value of 0.009 and a R^2 value of 0.95. But, the relationship most representative of Eq. (4.6), $V_n(\acute{a}_{nw}, \acute{J}_{\mathrm{nw}}, \acute{\chi}_n)$, again provides the most accurate prediction of the data ($\mathrm{GCV} = 2.1 \cdot 10^{-5}$, $R^2 = 0.998$). It appears that the inclusion of the Euler characteristic to the $P_c(S_w, a_{nw})$ relationship is needed to produce the most unique relationship. This is an important result as these relationships have not previously been explored in non-equilibrium multi-phase flow experiments. Although the non-equilibrium and quasi-equilibrium experiments exhibit many of the same trends in their state variable relationships, there is still the question of whether a single constitutive relationship can describe two-phase flow independent of flow condition.

4.4.3 Effect of flow condition on two-phase flow constitutive relationships

To determine how flow condition (quasi-equilibrium vs. non-equilibrium) affects hysteresis in constitutive relationships, the quasi- and non-equilibrium data were merged into a single dataset. It follows that if flow condition does not have an effect on a constitutive relationship then the inclusion of all the data would not increase the magnitude of hysteresis. The GCV and R^2 values of the GAM fits for this combined data set are illustrated in Fig. 4-5.

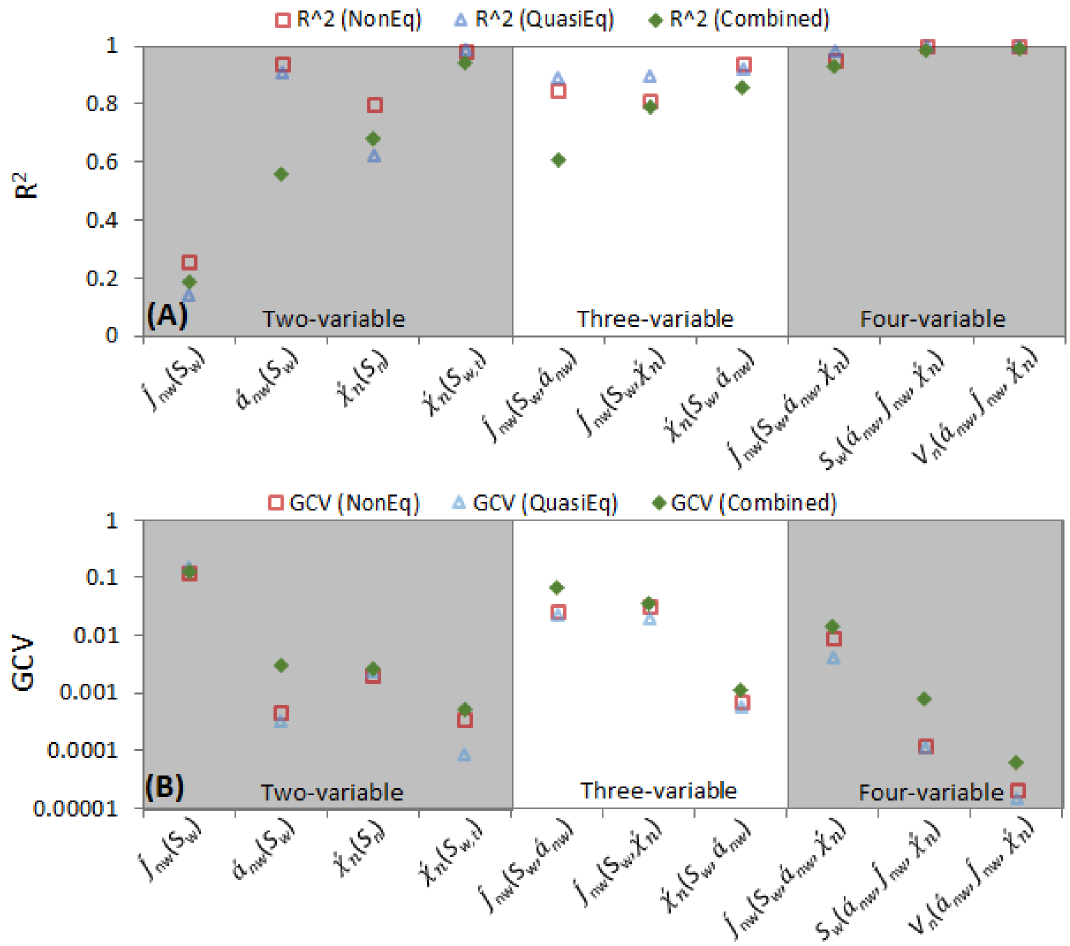

Figure 4-5. The GAM fit error for the combined data set are shown for both R^2 (a) and GCV (b) along with the quasi- and non-equilibrium values from Fig. 4-4.

The two-variable relationships produced no surprises based on a cursory look at the comparison between the quasi- and non-equilibrium data in Fig. 4-2. For the $P_c(S_w)$ and $\chi_n(S_n)$ relationships, the quasi- and non-equilibrium data overlap fairly well (Fig. 4-2), and therefore the magnitude of hysteresis is not changed in the combined data with the GCV and R^2 values falling between the quasi- and non-equilibrium values. The $\acute{a}_{nw}(S_w)$ relationship, however, is highly dependent on flow condition as the error in the GAM fit is dramatically increased when the quasi- and non-equilibrium data are combined. Also of note, the $\acute{\chi}_n(S_{w,t})$ relationship for the combined data explains 94% of the variance in the data compared to 99% and 98% for the quasi- and non-equilibrium experiments, respectively. This suggests that the $\acute{\chi}_n(S_{w,t})$ relationship is slightly dependent on flow condition.

Similarly, the combined three-variable relationships are not unique with respect to flow condition. The hysteresis in the $\acute{J}_{\mathrm{nw}}(\mathrm{S_w}, \acute{a}_{nw})$ relationship is notably increased with the combination of the quasi- and non-equilibrium data (GCV = 0.068, $R^2 = 0.61$). In the supporting information Fig. 4-10, we include a visual comparison of this separation between the non- and quasi-equilibrium experiments with the P_c-S_w-a_{nw} relationship fitted to biquadratic equations as presented in previous works [Porter et al., 2010]. Based on research using two-dimensional micromodels, Godinez-Brizuela et al. [2017] and Karadimitriou et al. [2014] similarly concluded that a single $P_c(S_w, a_{nw})$ relationship does not exist independent of flow condition, for a specific porous medium under transient conditions.

When the quasi- and non-equilibrium data sets are combined, the error present in the four-variable relationship $\acute{J}_{\mathrm{nw}}(\mathrm{S}_w, \acute{a}_{nw}, \acute{\chi}_n)$ is increased in relation to the separate data sets with a GCV of 0.014 and a R^2 of 0.93. Although we cannot conclude that the $\acute{J}_{\mathrm{nw}}(\mathrm{S}_w, \acute{a}_{nw}, \acute{\chi}_n)$ relationship provides a unique solution to the state of the system, by including all the state variables, hysteresis is drastically reduced. The overall $\acute{J}_{\mathrm{nw}}(\mathrm{S}_w, \acute{a}_{nw}, \acute{\chi}_n)$ relationship explains 93% of the variance for fluid configurations in the given porous medium. That means that, depending on the requirements in terms precision, one could use this relationship to predict the state of the system independent of flow condition. Further non-equilibrium experiments with higher capillary number flows would allow for expansion of the validity of this relationship. It is also possible that the error associated with this relationship is partially due to the slight pore size distribution differences between the compared porous media (Fig. 4-2d). It follows that the $V_n(\acute{a}_{nw}, \acute{J}_{\mathrm{nw}}, \acute{\chi}_n)$ relationship should better predict the data as it is less dependent on the porous medium structure. This is indeed the case as the $V_n(\acute{a}_{nw}, \acute{J}_{\mathrm{nw}}, \acute{\chi}_n)$ relationship has a GCV of $6.2 \cdot 10^{-5}$ and R^2 of 0.992. Unlike the $\acute{J}_{\mathrm{nw}}(\mathrm{S}_w, \acute{a}_{nw}, \acute{\chi}_n)$ relationship, we can conclude that (for the experimental conditions explored here) the $V_n(\acute{a}_{nw}, \acute{J}_{nw}, \acute{\chi}_n)$ relationship can uniquely predict the state of the system independent of flow condition.

4.5 Conclusions

We present a comparison of quasi- and non-equilibrium two-phase flow in a three-dimensional porous medium using fast x-ray microtomography. The rapidly improving methodology of fast microtomography provides the unprecedented ability to track moving, and evolving, fluid interfaces in three-dimensional pore space. We have demonstrated with experimental data that the geometric state function, $\acute{J}_{nw}(S_w, \acute{a}_{nw}, \acute{\chi}_n)$, presented by McClure et al. (2018) uniquely predicts the mean curvature for both quasi- and non-equilibrium two-phase flow. This is not the case for many lower dimensional constitutive relationships, which have been demonstrated to be hysteretic. An interesting exception to this conclusion is the $\acute{\chi}_n(S_{w,t})$ relationship which can uniquely predict the connectivity of a system based on the trapped wetting phase saturation. This has significant applications in engineered multi-phase flow situations, for instance subsurface storage of CO_2 via capillary trapping. Yet, it is important to acknowledge that while the theoretical value of this finding is significant, when it comes to solving a practical (field-scale) problem, P_c can be measured relatively easily at larger scales.

When combining the quasi- and non-equilibrium data, the $\acute{J}_{nw}(S_w, \acute{a}_{nw}, \acute{\chi}_n)$ relationship only explains 93% of the variance, suggesting that it is slightly dependent on the flow condition of the system. The $V_n(\acute{a}_{nw}, \acute{J}_{nw}, \acute{\chi}_n)$ relationship, on the other hand, is independent of flow condition. This relationship provides a better prediction of the data because it is less dependent on the porous medium and more closely represents the Minkowski Steiner formula, which is the underlying basis of these relationships.

A few additional points that may need to be addressed in further studies include: (i) non-equilibrium flow experiments using higher capillary numbers would address whether these findings apply under more different non-equilibrium conditions. (ii) Further studies in natural porous media would also be needed to further generalize the validity of the $V_n(\acute{a}_{nw}, \acute{J}_{\mathrm{nw}}, \acute{\chi}_n)$ relationship predicting the state of the system independent of flow condition. It is unclear whether the measured error in the $\acute{J}_{\mathrm{nw}}(S_w, \acute{a}_{nw}, \acute{\chi}_n)$ relationships between the quasi- and non-equilibrium cases is merely a function of the smooth surfaces of sintered glass beads allowing for a higher degree of relaxation within the system. (iii) Interfacial area development is an important parameter describing mass transfer in multiphase flow operations (e.g. groundwater remediation) and, therefore, it is important to understand how relaxation affects interfacial area generation. In a subsequent paper, we are finding that the magnitude of interfacial area generation and the shape of the $a_{nw}(S_w)$ curves are dependent on the degree of relaxation during drainage and imbibition. By better understanding how the extent of relaxation in the system affects interfacial area formation, we will be able to develop more robust models and operational control of many industrial and environmental multiphase systems.

4.6 Acknowledgements

This work was supported by the U.S. National Science Foundation, Hydrologic Sciences Program under award #1344877. This work was performed at GeoSoilEnviroCARS (The University of Chicago, Sector 13), Advanced Photon Source (APS), Argonne National Laboratory. GeoSoilEnviroCARS is supported by the National Science Foundation - Earth Sciences (EAR - 1634415) and Department of Energy- GeoSciences (DE-FG02-94ER14466). This research used resources of the Advanced Photon Source, a U.S. Department of Energy (DOE) Office of Science User Facility operated for the DOE Office of Science by Argonne National Laboratory under Contract No. DE-AC02-06CH11357.

4.7 Supplementary Information

4.7.1 High intensity ring artifact removal methodology

Some high intensity ring artifacts were present in the raw data (seen in Fig. 4-6a) which are not generally observed in monochromatic scans using the same detector. These artifacts are, therefore, attributed to defects in the platinum mirror that the x-ray beam is reflected on to remove high-energy x-rays. The mirror was translated perpendicular to the beam and the defects move with the mirror. The high-intensity artifacts are removed in post-processing by first transforming the data to polar coordinates (Fig. 4-6b) and then to the frequency domain (Fig. 4-6c) using a fast Fourier transform (FFT). In this coordinate system, the high intensities are located along the horizontal axis and are therefore easily eliminated by cropping away the centerline in the FFT image (Fig. 4-6d). An inverse FFT is then performed (Fig. 4-6e), followed by an inverse polar transform back into Cartesian coordinates (Fig. 4-6f), and the result is a clear reduction in ring artifacts.

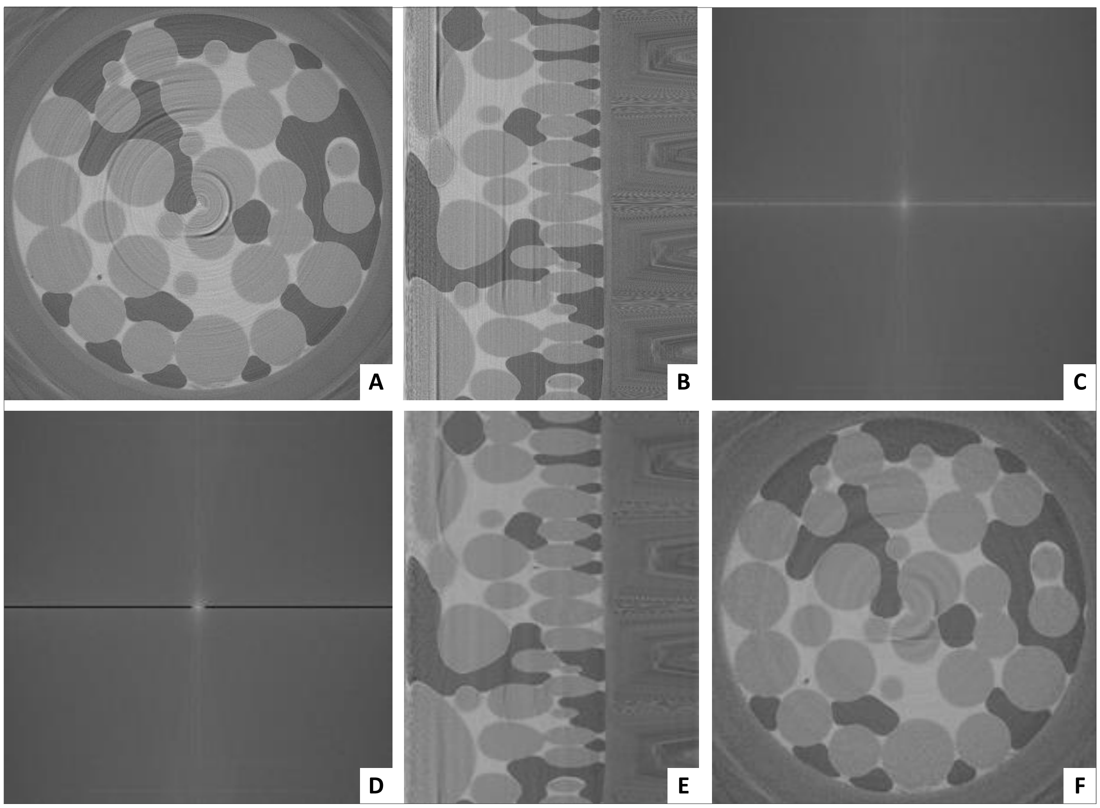

Figure 4-6. Ring artifact removal steps on reconstructed data. The raw data (a) is converted to polar coordinates (b) and then to the frequency domain (c) where the high intensity ring artifacts are located along the horizontal axis and easily removed (d). The data is then converted back to polar (e) and then Cartesian (f) coordinates.

4.7.2 REV analysis

Due to the relatively small field of view size in microtomography images compared to the full experimental column volume, a representative elementary volume (REV) analysis for wetting saturation, S_w, and specific interfacial area, a_{nw}, were performed. If an REV for each parameter is reached, then each parameter becomes independent of the size of the sample and the results of the study can be compared to other studies in similar porous media. These values were calculated in increasing cube volumes (ranging from 0.001-54.9 mm^3) centered in the scanned section of the glass bead column. The REV analysis for a subset of S_w (Fig. 4-7a) and a_{nw} (Fig. 4-7b) values suggest that steady values are being reached towards the outer limit of the domain size. The values were also calculated for the entire cylindrical volume of the scanned section of the column. These total field of view values were less than 2.8% and 0.016 mm^{-1} different than the largest selected cube volume for S_w and a_{nw}, respectively. Thus, furthering the assumption that steady values are being reached, and indicating that edge effects of the column walls are small which has been observed in similar studies (Porter et al., 2010). Therefore, it is likely that the upper domain size (98.3 mm^3) reaches the lower limit of an acceptable REV and this volume was used for all analyses in the study.

Different experimental columns were used for the quasi- and non-equilibrium experimental columns because each data set required use of a full beam-time allocation at the Advanced Photon Source at Argonne National Lab. It has also been reported that high-energy x-ray exposure can cause unwanted effects such as bubble formation in the fluid phase and wettability alteration of the solid surface (Brown et al., 2014; Kwon et al., 2009). Reducing x-ray exposure during experimental runs and using new columns for each experiment allowed us to mitigate such potential artifacts. Because the bead size distributions, porosities, and Euler characteristics are similar for the two experiments, it was assumed that the pore geometries were comparable and analyses performed for either experiment can be compared as long as an REV is achieved. The columns were the same dimension (6 mm radius, 26 mm height) and were randomly packed, with the same size distribution of soda-lime glass beads (0.8-1.2 mm diameter) that were sintered using the same parameters (730 ºC, 20 min). The resulting porosities for the quasi- and non-equilibrium experimental columns were 0.37 and 0.39, respectively. Also, the pore space Euler characteristic (a measure of the connectedness of the pore space) for the quasi- and non-equilibrium experimental columns were very similar at -413 and -386.

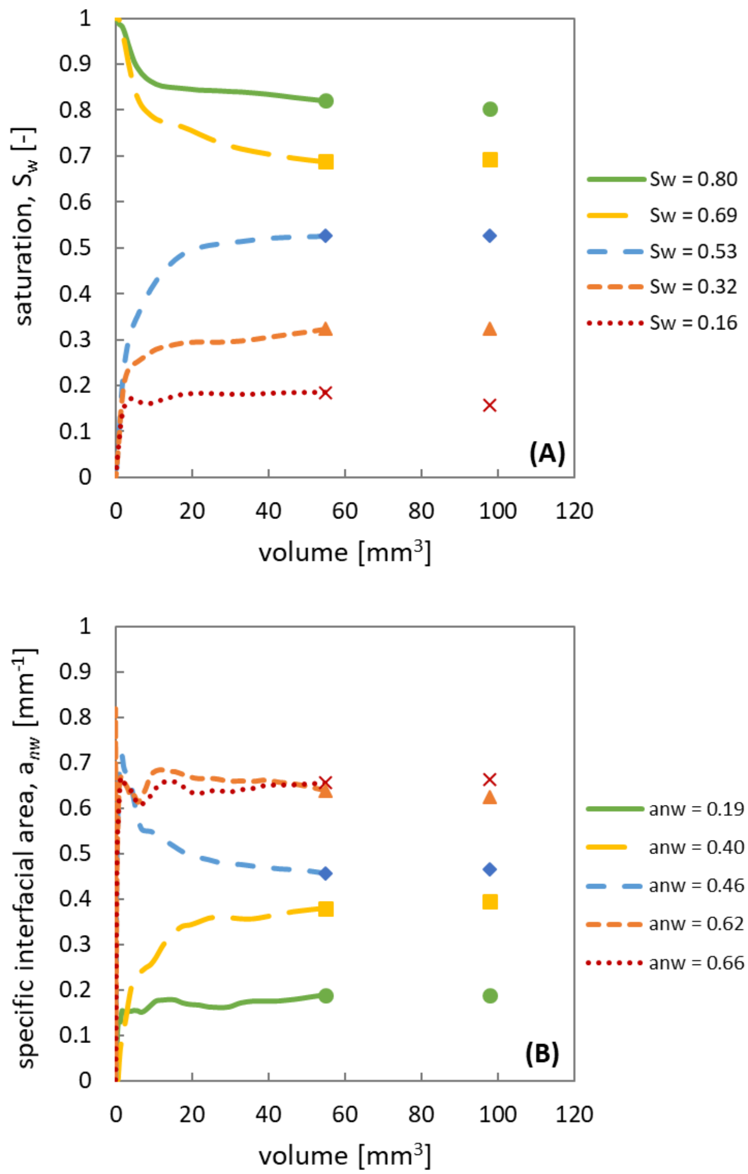

Figure 4-7. A subset of S_w (a) and a_{nw} (b) values for varying cube volumes of interest selected in the porous medium. The data points at 98.3 mm^3 represent the values calculated for the entire cylindrical volume of the imaged section of the column.

4.7.3 External pressure transducer and calculated capillary pressure comparison

For equilibrium data points in the quasi-equilibrium data (Fig. 4-8, bolded points), bulk pressure ($P_n - P_w$) should equal capillary pressure (P_c) due to the Young-Laplace equation. In Fig. 4-8, there is good correlation between $P_n - P_w$ and P_c for the quasi-equilibrium data except at the low capillary pressures. A possible cause for this discrepancy is that the method to separate disconnected and connected regions is not perfect (as described in section 4.3.5.1). If disconnected phase is included in the P_c calculation, then the capillary pressure would be skewed towards the pressure at the time that the phase was disconnected from the bulk phase (Li et al., 2018). This would lead to overestimation of P_c at low capillary pressures and underestimation of P_c at high capillary pressures. In glass bead packs, trapped non-wetting phase blobs are generally larger than trapped wetting phase pendular rings. Therefore, label misidentification causing discrepancies in P_c calculations is more likely for low P_c data points where trapped non-wetting phase is more prevalent. This is corroborated when disconnected phase is intentionally included in the P_c calculation (Fig. 4-8, insert) and the discrepancy with transducer measurements is intensified at pressure extremes.

The non-equilibrium data follows similar trends as the quasi-equilibrium data, but tends to diverge more from the transducer measurements at pressure extremes, especially at high capillary pressures. This could be a function of the overall increase of disconnected phase compared to the quasi-equilibrium experiment (Fig. 4-9), therefore increasing the likelihood of label misidentification. It could also be a dynamic capillary pressure effect as the pressure of the connected phase interface is not allowed to relax towards equilibrium in the non-equilibrium case.

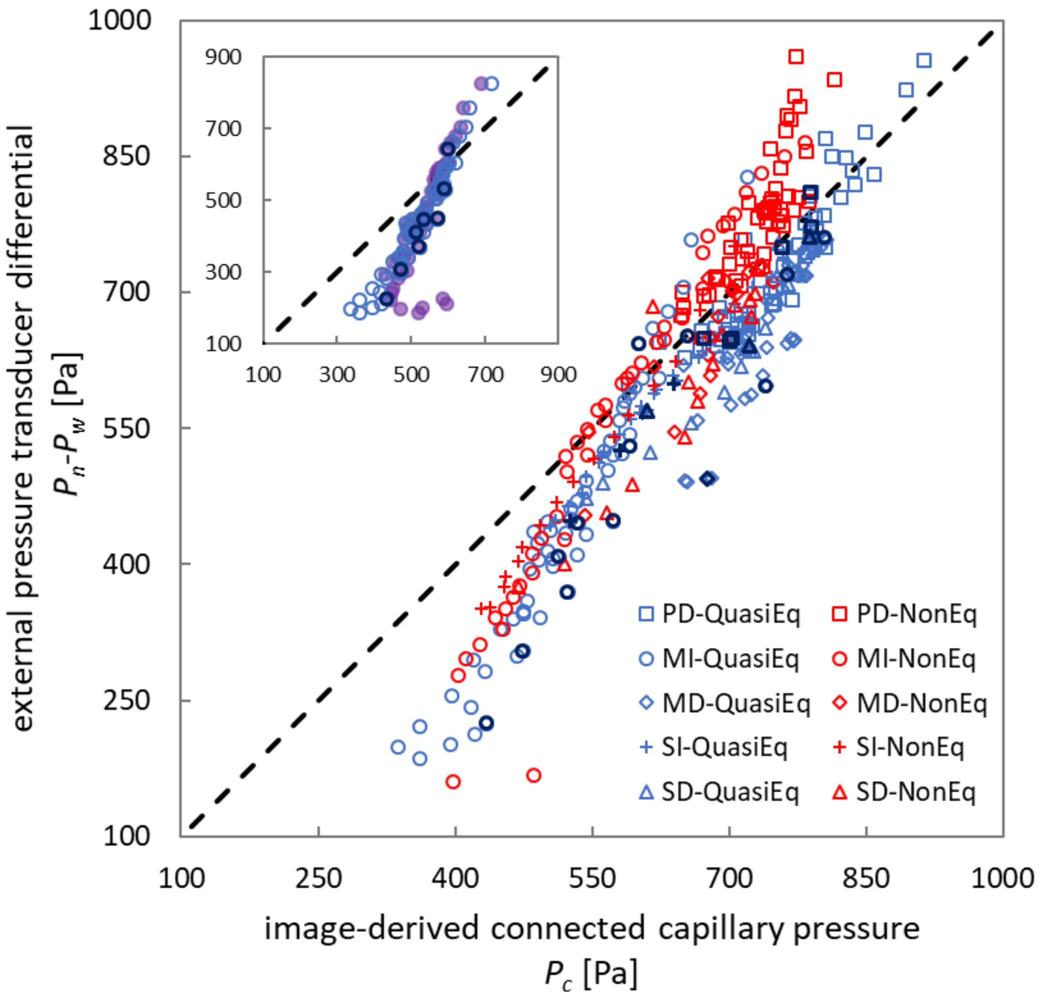

Figure 4-8. External pressure transducer measured pressure differential, $P_n - P_w$, comparison with capillary pressure, P_c, calculated from image-derived interfacial curvatures of the fluid phases connected to bulk phases for the quasi-equilibrium (blue) and non-equilibrium (red) experiments. Quasi-equilibrium relaxation points are bolded. (Insert) The pressures of the main imbibition quasi-equilibrium experiment for connected interfaces (open circles) and for all fluid interfaces (filled circles).

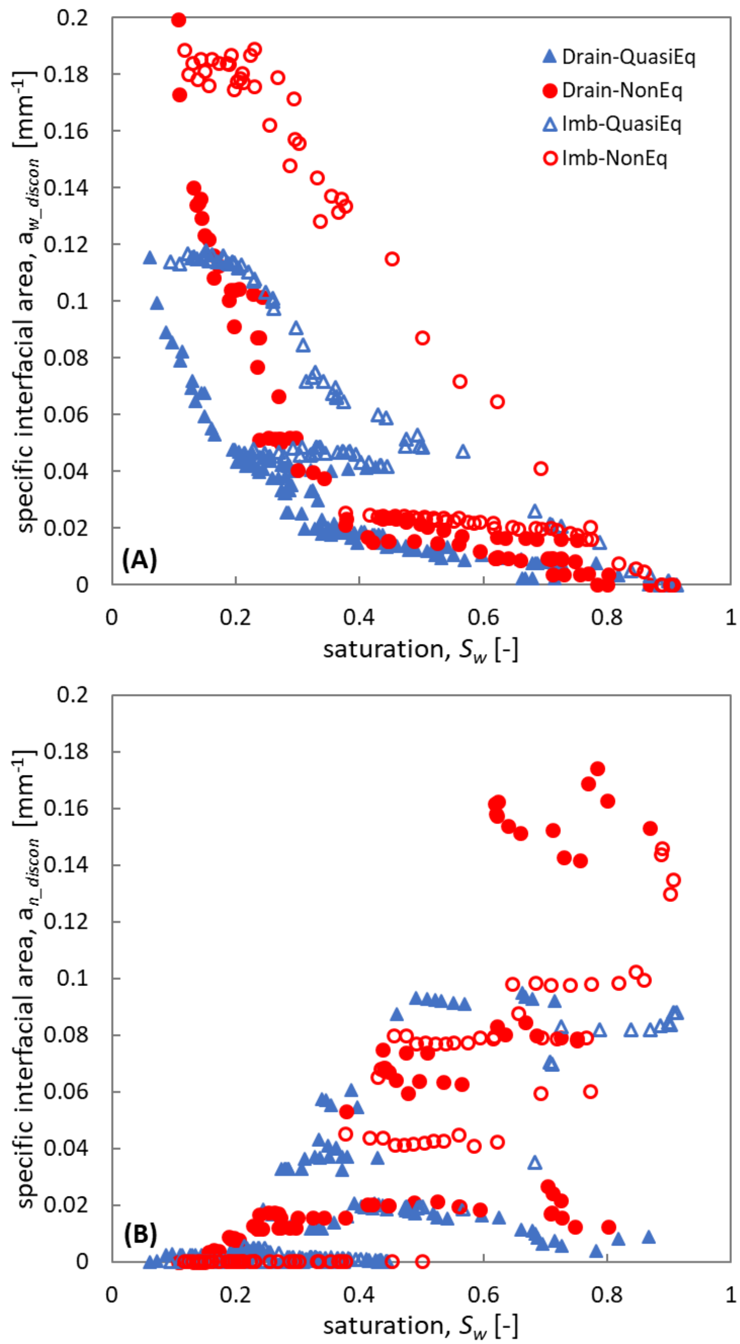

Figure 4-9. Disconnected wetting (a) and non-wetting (b) phase specific interfacial area (a_{w_discon}, a_{n_discon}) as a function of saturation S_w for the quasi- and non-equilibrium flow experiments.

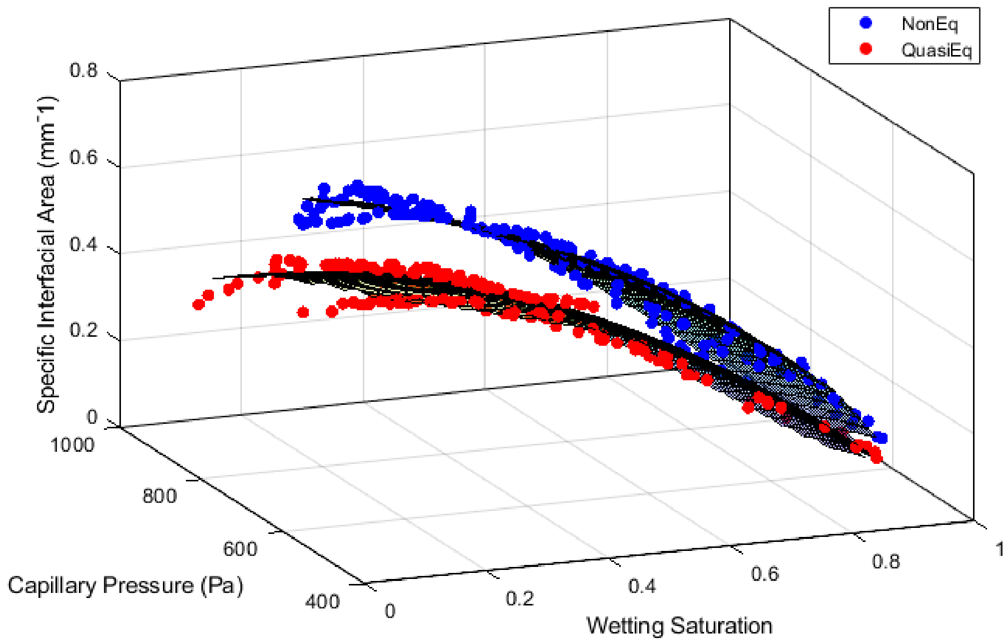

Figure 4-10. Three-dimensional representation of the P_c-S_w-a_{nw} relationships for the non- and quasi-equilibrium experiments fitted by biquadratic polynomials**.**

Chapter 5. Predicting the Effect of Relaxation on Interfacial Area Development in Multi-Phase Flow

Douglas E. Meisenheimer[1] and Dorthe Wildenschild[1]

1. School of Chemical, Biological, and Environmental Engineering, Oregon State University, Corvallis, Oregon, U.S.A.

Water Resources Research, American Geophysical Union
2000 Florida Ave. NW, Washington, DC 20009
Submittal expected April 2020

5.1 Abstract

Two-phase flow experiments in the literature are compared to study the effect of fluid relaxation in quasi-equilibrium experiments on interfacial area generation. Interfacial area is an important parameter that controls mass transfer in many engineered multiphase systems, so it is important to generate accurate predictive tools of multiphase flow to engineer efficient processes. An empirical relationship was theorized and verified for an $a_{nw}(S_w)$ relationship that was also dependent on the number of quasi-equilibrium relaxation points taken during a drainage or imbibition experiment. It was determined that different relationships would be required depending on the fluids and porous medium, but clear trends were observed which could provide the possibility of engineering multiphase systems that generate a particular amount of interfacial area once a predictive relationship is established for the system.

5.2 Introduction

Fluid-fluid interfacial area is an important parameter of relevance to multiphase flow in porous media, and in terms of a variety of applications including geologic CO_2 sequestration [e.g. Herring et al., 2013] and contaminant remediation of groundwater using in-situ air sparging [e.g. Johnson et al., 1993]. Interfacial area controls mass and energy transfer between different fluid phases within a system, thereby controlling the reaction efficiency of the undergoing process, but it also influences the multi-phase fluid flow processes in the system. There is a need to better understand this relationship between interfacial area and fluid flow processes so that more robust theories and models can be developed to improve the efficacy of many multiphase flow scenarios of importance to society.

Of particular interest is the effect that relaxation has on macroscopic invariants (i.e. wetting saturation, average capillary pressure, specific interfacial area, Euler characteristic) during equilibrium of a multi-phase system [Gray et al., 2015; Schlüter et al., 2017; Meisenheimer, McClure et al., 2020]. The relaxation of a multi-phase system leads to distinct differences between flow experiments conducted under non-equilibrium and quasi-equilibrium conditions. Many multi-phase experiments have used x-ray microtomography (µCT) to visualize the movement and distribution of fluids within porous media in three dimensions [e.g. Blunt et al., 2013; Dorthe Wildenschild & Sheppard, 2013]. Traditionally, this methodology has required experiments to be limited to observations under quasi-equilibrium flow conditions due to the time required to acquire a µCT image [e.g. Costanza-Robinson et al., 2008; Porter et al., 2010; Araujo & Brusseau, 2020]. With the recent advent of fast µCT, it is now possible to conduct non-equilibrium multi-phase flow experiments [e.g. Berg et al., 2013; Leu et al., 2014; Schlüter et al., 2016; Singh et al., 2017; Meisenheimer, McClure et al., 2020]. The question remains whether parallels can be drawn between observations made under quasi-equilibrium conditions and those made in non-equilibrium conditions.

Both Gray et al. [2015] and Schlüter et al. [2017] observed a reduction of specific interfacial area (a_{nw}) (the interfacial area between the wetting and non-wetting phases within a representative volume), as the system relaxes towards equilibrium in micromodel and microtomography studies, respectively. By extension, one would conclude that quasi-equilibrium experiments (which allow for relaxation) would generate less interfacial area than non-equilibrium experiments. Indeed, this was observed by Meisenheimer, McClure et al. [2020] using fast µCT experiments.

Many pore scale models [Reeves & Celia, 1996; Kawanishi et al., 1998; Or & Tuller, 1999; Held & Celia, 2001; Diamantopoulos & Durner, 2015] and thermodynamic models [Leverett, 1941; Bradford & Leij, 1997; Oostrom et al., 2001; Grant & Gerhard, 2007] have been utilized to predict interfacial area as a function of wetting saturation (S_w) in porous media systems but, to our knowledge, none of these include descriptions of interfacial relaxation. This study seeks to shed light on the process of interfacial relaxation, and to develop empirical relationships that can be used to predict the $a_{nw}(S_w)$ relationship for similar porous media. The empirical relationships are developed based on the magnitude of interfacial relaxation observed during the main drainage or imbibition branch of a number of multi-phase flow experiments.

5.3 Materials and Methods

5.3.1 Experimental data

All microtomography experiments were performed at the Advanced Photon Source on the GSECARS 13-BM-D beamline at Argonne National Laboratory, IL. An overview of the experiments is presented in Table 5-1. The datasets were collected under quasi-equilibrium [Culligan et al., 2004; Culligan et al., 2006; Wildenschild & Prodanovic, 2009; Wildenschild, 2009; Porter et al., 2010; Meisenheimer, Mcclure et al., 2020] and non-equilibrium [Schlüter et al., 2017; Meisenheimer, McClure et al., 2020] conditions. The difference between quasi-equilibrium from non-equilibrium conditions is defined by Meisenheimer, McClure et al. [2020] as the inclusion of relaxation points, R_{pts}, on a drainage or imbibition curve. The imaging techniques for quasi- and non-equilibrium experimentation are described broadly by Wildenschild and Sheppard [2013] and in detail by Meisenheimer, Rivers and Wildenschild [2020].

These datasets were selected to investigate the validity of an empirical $a_{nw}(S_w)$ relationship over a variety of conditions; (i) the datasets include a varying number of relaxation points ($0 \leq R_{pts} \leq 14$) on a given main drainage or main imbibition curve (flow experiments which fully cover saturations between irreducible wetting and residual non-wetting saturation). (ii) air-water and oil-water experiments were included to test the effect of fluid pair. Soltrol 220 (Chevron Phillips) [Culligan et al., 2004; Culligan et al., 2006] and n-dodecane [Schlüter et al., 2017] were used as the non-wetting phase in the oil-water experiments, but both oils have a similar measured interfacial tension (γ=0.036 N/m) so they were deemed analogous for comparisons in this study. (iii) most of the experiments are performed in glass bead columns except for the experiments performed by Wildenschild and Prodanovic [2009] in crushed tuff samples which are included to investigate the effect of porous medium on the empirical $a_{nw}(S_w)$ relationship. (iv) finally, an experiment which produced scanning curve data (drainage and imbibition curves which begin at intermediate saturations) was included to test whether an expression could be developed to include predicted scanning curves as a function of initial wetting saturation. The porosity of each

Table 5-1. Various two-phase flow x-ray microtomography experiments

Source	Flow Condition	Solid Phase	φ	NW Phase	Flow Rate (mL/hr)	γ (N/m)	Ca
Schlüter et al. (2017)[a]	Non-Eq.	Glass Beads	0.33	n-dodecane	0.02	0.036	1.00E-08
Meisenheimer, McClure et al. (2020)	Non-Eq.	Glass Beads	0.39	Air	0.5	0.072	1.94E-07
Meisenheimer, McClure et al. (2020)	Quasi-Eq.	Glass Beads	0.37	Air	0.5	0.072	2.08E-07
Culligan et al. (2004)	Quasi-Eq.	Glass Beads	0.34	Air	0.25	0.0681	2.64E-08
Culligan et al. (2004)	Quasi-Eq.	Glass Beads	0.34	Air	2.0	0.0681	2.06E-08
Wildenschild (2009)	Quasi-Eq.	Glass Beads	0.37	Air	6.0	0.072	2.45E-06
Wildenschild and Prodanovic (2009)	Quasi-Eq.	Crushed Tuff	0.38	Air	1.0	0.072	3.77E-07
Wildenschild and Prodanovic (2009)	Quasi-Eq.	Crushed Tuff	0.38	Air	3.0	0.072	1.13E-06
Wildenschild and Prodanovic (2009)	Quasi-Eq.	Crushed Tuff	0.38	Air	6.0	0.072	2.26E-06
Porter et al. (2010)	Quasi-Eq.	Glass Beads	0.36	Soltrol	0.6	0.0378	4.54E-07
Culligan et al. (2006)	Quasi-Eq.	Glass Beads	0.34	Soltrol	0.5	0.0364	9.49E-08
Culligan et al. (2006)	Quasi-Eq.	Glass Beads	0.34	Soltrol	3.0	0.0364	6.04E-07

[a] CsCl was used as the wetting phase contrast agent instead of KI

porous medium, ϕ, is similar for all the experiments ($0.33 \leq \phi \leq 0.39$) allowing us to draw parallels between the collected $a_{nw}(S_w)$ data.

The experimental setup for each experiment was similar. The porous medium was contained in a sample holder with wetting and non-wetting fluid lines connected to the bottom and top of the column, respectively. Before fluids were introduced into the porous medium, a µCT image was collected of the dry sample to use as a priori information to help with segmentation of the subsequent partially saturated images. Potassium iodide, KI, was used as a contrast agent in the wetting phase to better differentiate between the fluids for most of the experiments except for Schlüter et al. [2017], who used cesium chloride, CsCl, as the contrast agent in the wetting phase. Generally, pressure transducers (Validyne P55 differential pressure transducer) were inserted in the fluid lines to measure the differential pressure between the fluids during the experiments. In all the experiments, the flow of the wetting phase was controlled by a syringe pump (Precision Instruments SP210IW, Harvard Apparatus PhD 200) which induced the flow of the non-wetting phase. A hydrophobic membrane was used at the bottom of the sample to allow the system to reach low wetting saturations. Quasi-equilibrium points were allowed about 15 minutes of relaxation before a µCT image was collected. More detailed explanations of the experimental setups can be found in the original source of each dataset, see Table 5-1.

The primary drainage (PD) $a_{nw}(S_w)$ relationships of the glass bead experiments in Table 5-1 were initially plotted to visualize obvious trends between interfacial area generation and the magnitude of relaxation in the system. These datasets are presented in Fig. 5-1 and an obvious monotonic reduction in interfacial area generation is observed as R_{pts} in primary drainage is increased. Interestingly, this trend holds for both air-water and oil-water experiments, suggesting that interfacial area generation is not affected by fluid pair composition for drainage experiments in glass bead columns. Also, the saturation at which the peak interfacial area value is reached tends to increase with increasing R_{pts}. To better understand these initial observations, we develop a relationship between $a_{nw}(S_w)$ and R_{pts} in the following.

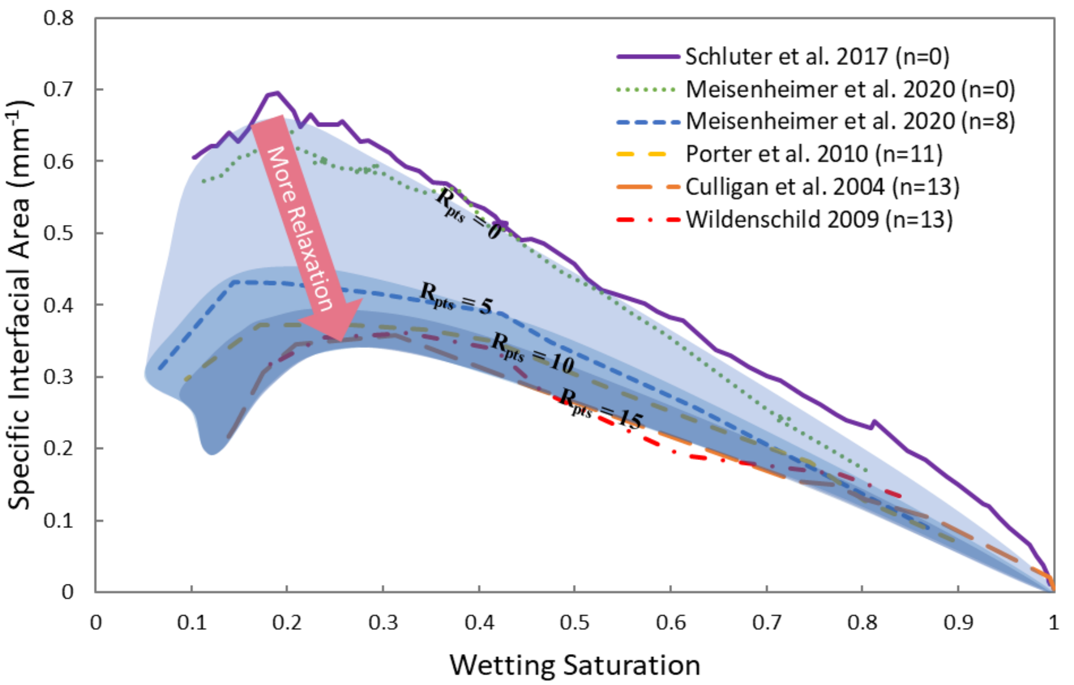

Figure 5-1. Specific interfacial area (a_{nw}) vs. wetting saturation (S_w) data for various primary drainage experiments with shaded regions representing the observed reduction of a_{nw} relative to the number of quasi-equilibrium relaxation points (R_{pts}) for an experiment.

5.3.2 Empirical equation for the $a_{nw}(S_w)$ relationship

Rather than predicting the $a_{nw}(S_w)$ relationship from thermodynamic or numeric models, our aim was to study the effect of relaxation on the $a_{nw}(S_w)$ relationship by the fitting of an empirical equation to experimental data. The basic requirements of an empirical equation would be a continuous function where: $\{S_w \in \mathbb{R} : 0 \leq S_w \leq 1\}$, $a_{nw}(0) = 0$, $a_{nw}(1) = 0$, and $a_{nw}(S_w) > 0\ for\ (0,1)$. Looking beyond the field of multi-phase flow, we discovered a mathematical equation that will allow for these constraints, and that also has a shape similar to typical $a_{nw}(S_w)$ data; the well-known Monod equation [Monod, 1949], with an extension for substrate inhibition developed by Han and Levenspiel [1988] for microbial growth kinetics:

$$\mu = \mu_{max}\left(1 - \frac{S}{S_{max}}\right)^n \frac{S}{S + K_s\left(1 - \frac{S}{S_{max}}\right)^m} \tag{5-1}$$

where μ is the specific growth rate of cells, μ_{max} is the maximum specific growth rate, S is the substrate concentration, S_{max} is the critical substrate concentration above which growth stops, m and n are fitting constants, and K_s is the half-saturation constant (i.e. the substrate concentration where $\mu / \mu_{max} = 0.5$, $m = 0$, and $n = 0$). Using the constraint that $S_{max} = 1$ and changing the variables to model the $a_{nw}(S_w)$ relationship leads to the following empirical relationship:

$$a_{nw} = \mu_{max} \frac{S_w(1-S_w)^n}{S_w+K_s(1-S_w)^m} \tag{5-2}$$

where μ_{max}, K_s, m, and n are constants that represent the maximum a_{nw}, the saturation at which the maximum a_{nw} is achieved, the concavity of the left-hand side of the $a_{nw}(S_w)$ curve, and the concavity of the right-hand side of the $a_{nw}(S_w)$ curve, respectively. A graphical representation of Eq. (5-2) is presented in Fig. 5-2.

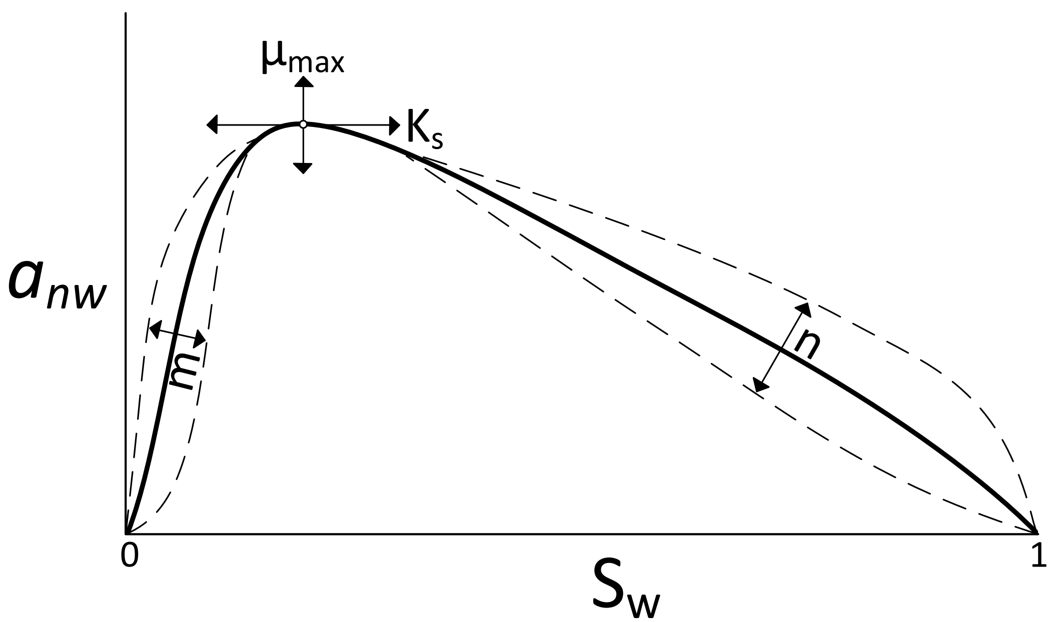

Figure 5-2. Schematic of an arbitrary specific interfacial area (a_{nw}) vs. wetting saturation (S_w) dataset (solid line) with indications on how the constants (μ_{max}, K_s, m, and n) in the extended Monod equation with substrate inhibition would change the shape of the $a_{nw}(S_w)$ curve.

5.3.3 Evaluation of the constants of the empirical $a_{nw}(S_w)$ relationship

Han and Levenspiel [1988] outlined how to evaluate the constants of Eq. (5-2) by first determining μ_{max} and n at high saturation. With the assumption that $S_w >> K_s$, Eq. (5-2) simplifies to:

$$a_{nw} = \mu_{max}(1 - S_w)^n \tag{5-3}$$

and taking the logarithm gives:

$$\ln a_{nw} = n \ln(1 - S_w) + \ln \mu_{max} \tag{5-4}$$

By plotting the high saturation data ($S_w > 0.4$) and fitting a line to Eq. (5-4), μ_{max} and n can be evaluated. K_s and m can be evaluated by rearranging Eq. (5-2),

$$K_{s,obs} = K_s(1 - S_w)^m = S_w\left[\frac{\mu_{max}(1-S_w)^n}{a_{nw}} - 1\right] \tag{5-5}$$

solving for $K_{s,obs}$, and plotting the logarithm of Eq. (5-5) with the low saturation data ($S_w <$ ~0.2)

$$\ln K_{s,obs} = m \ln(1 - S_w) + \ln K_s \tag{5-6}$$

Low saturation is difficult to achieve in experimental data, so some of the data sets do not have enough low saturation data to fit Eq. (5-6) with any certainty. For these datasets with at least one data point at a lower wetting saturation than the maximum interfacial area, μ_{max} and n were evaluated using Eq. (5-4) and then K_s and m were evaluated using the least squares method to minimize the sum of squared residuals of Eq. (5-2) in order to find an approximation. The datasets using this approximation are indicated in Tables 5-2 and 5-3 with R^2 values for the least squares approximation. Tables 5-2 and 5-3 present the evaluated constants for the drainage and imbibition experiments, respectively. Also, the main drainage dataset for the non-equilibrium air-water experiment [Meisenheimer, McClure et al., 2020] was supplemented with the low wetting saturation points from primary drainage to fit a full drainage curve.

Table 5-2. Empirical $a_{nw}(S_w)$ relationship constants for drainage experiments

	Oil-Water						Air-Water										
	Schlüter et al. 2017		Porter et al. 2010			Culligan et al. 2006	Meisenheimer et al. 2020, Non-Eq		Meisenheimer et al. 2020 Quasi-Eq		Culligan et al. 2004			Wildenschild and Prodanovic 2009			
	PD	MD	PD	MD	MD2	MD	PD	MD	PD	MD	PD	MD	MD_ 2mLh	MD	MD2	MD_ 3mLh	MD_ 6mLh
u_{max}	0.83	0.82	0.65	0.49	0.45	0.47	0.99	0.85	0.67	0.62	0.45	0.51	0.50	0.51	0.50	0.47	0.47
K_s	0.06	0.13	0.11	0.09	0.13	0.34	0.08	0.10	0.07	1.28	2.42	1.82	1.99	0.27	0.88	0.52	0.61
m	8.30	12.29	2.00	4.73	11.54	7.65	4.42	10.25	1.51	16.40	20.37	17.12	17.81	6.16	12.03	9.47	12.74
n	0.85	0.80	0.98	0.72	0.62	0.77	1.03	0.74	0.99	0.73	0.74	0.68	0.74	0.31	0.29	0.25	0.26
[redacted]																	
R^2	--	--	--	0.998	--	--	--	--	--	--	--	--	--	--	--	--	0.961
R_{pts}	0	0	11	8	9	13	0	0	8	5	14	9	11	14	10	9	8

Table 5-3. Empirical $a_{nw}(S_w)$ relationship constants for imbibition experiments

	Oil-Water				Air-Water								
	Schlüter et al. 2017	Porter et al. 2010		Culligan et al. 2006	Meisenheimer et al., Non-Eq			Meisenheimer et al. 2020 Quasi-Eq	Wildenschild 2009	Wildenschild and Prodanovic 2009			
	MI	MI	MI2	MI_3mLh	MI	SI	SI2	MI	MI	MI	MI2	MI_3mLh	MI_6mLh
u_{max}	0.63	0.38	0.32	0.46	1.01	1.22	1.27	0.63	0.59	0.66	0.58	0.58	0.59
Ks	0.00	0.22	0.22	0.80	0.10	0.49	0.67	0.13	0.71	0.54	0.37	1.94	1.10
m	50.09	25.18	32.62	13.85	4.80	2.86	2.63	8.32	10.25	6.55	6.70	13.91	9.39
n	0.89	0.63	0.47	0.85	0.83	0.90	0.91	0.80	0.92	0.47	0.39	0.40	0.41
[redacted]													
R^2	0.999	0.997	0.999	--	--	0.993	0.997	0.992	--	0.994	--	--	--
R_{pts}	0	9	8	12	0	0	0	7	12	10	10	8	8

5.4 Results and Discussion

5.4.1 The effect of relaxation points on air-water and oil-water empirical $a_{nw}(S_w)$ relationships

In Figs. 5-3 and 5-4, the fitted empirical constants from Tables 5-2 and 5-3 are plotted against the number of relaxation points in the experiment to better understand the effect of relaxation on the constants under main drainage (MD) and main imbibition (MI) for air-water and oil-water experiments. Most of the trends between the empirical constants and R_{pts} are fitted to quadratic equations, except for the crushed tuff data which does not cover a wide enough range of R_{pts} to be fitted properly. Prediction outside of the experimental range of R_{pts} would not be advised because the resulting parameters would become unreliable and the resulting $a_{nw}(S_w)$ relationship would not make physical sense. Experiments with higher R_{pts} would be needed to generate better predictions.

Fig. 5-3a shows the fit for μ_{max} for both main drainage and imbibition for the air-water experiments. The μ_{max} value for both MD and MI seem to monotonically decrease towards a limit, with slightly higher imbibition interfacial area development than for drainage. The opposite is true for the oil-water experiments where MD interfacial area is located above MI, Fig. 5-3b. Main imbibition for the oil-water experiments is interesting because it is the only case where μ_{max} does not monotonically decrease with increasing R_{pts} over the experimental range. Accordingly, if a greater number of relaxation points are included in an oil-water experiment, imbibition could generate a higher maximum interfacial area than drainage. Interestingly, the main drainage fits for both air-water ($\mu_{max} = 0.0024R_{pts}^2 - 0.0593R_{pts} + 0.8531$) and oil-water ($\mu_{max} = 0.0031R_{pts}^2 - 0.0675R_{pts} + 0.8255$) are almost identical, suggesting that fluid pair only affects maximum interfacial area generation during imbibition.

This observation is reversed for the K_s fits where main imbibition for air-water (Fig. 5-4a) and oil-water (Fig. 5-4b) data are similar, but the main drainage relationships are different. Recall, that K_S controls the saturation at which the maximum a_{nw} is achieved. This suggests that during main imbibition, the saturation at which maximum interfacial area is achieved is not dependent on the fluid pair.

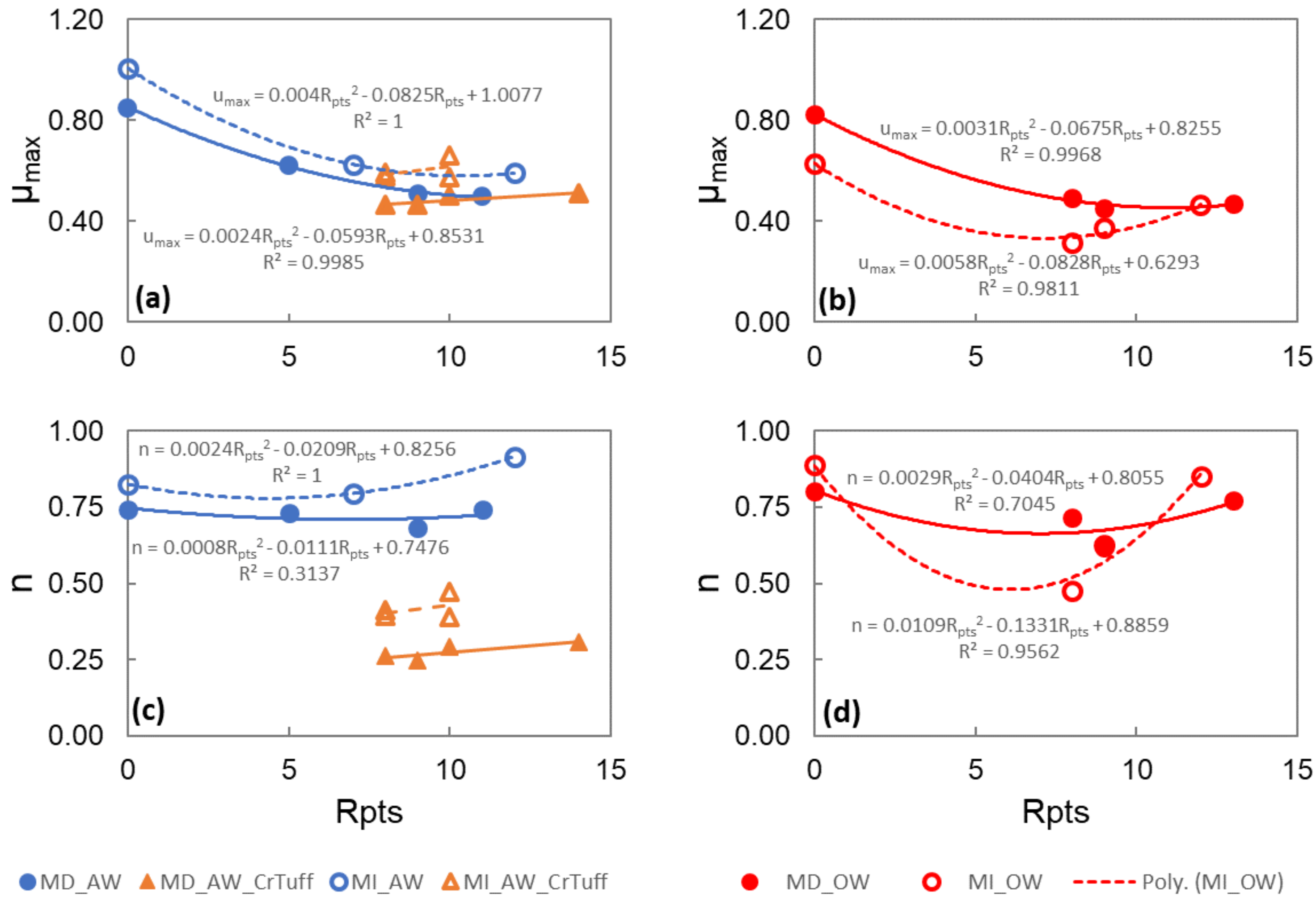

Figure 5-3. Main drainage (solid) and imbibition (dotted) polynomial fits for the $a_{nw}(S_w)$ relationship constants μ_{max} (a,b) and n (c,d) for air-water (left) and oil-water (right) experiments.

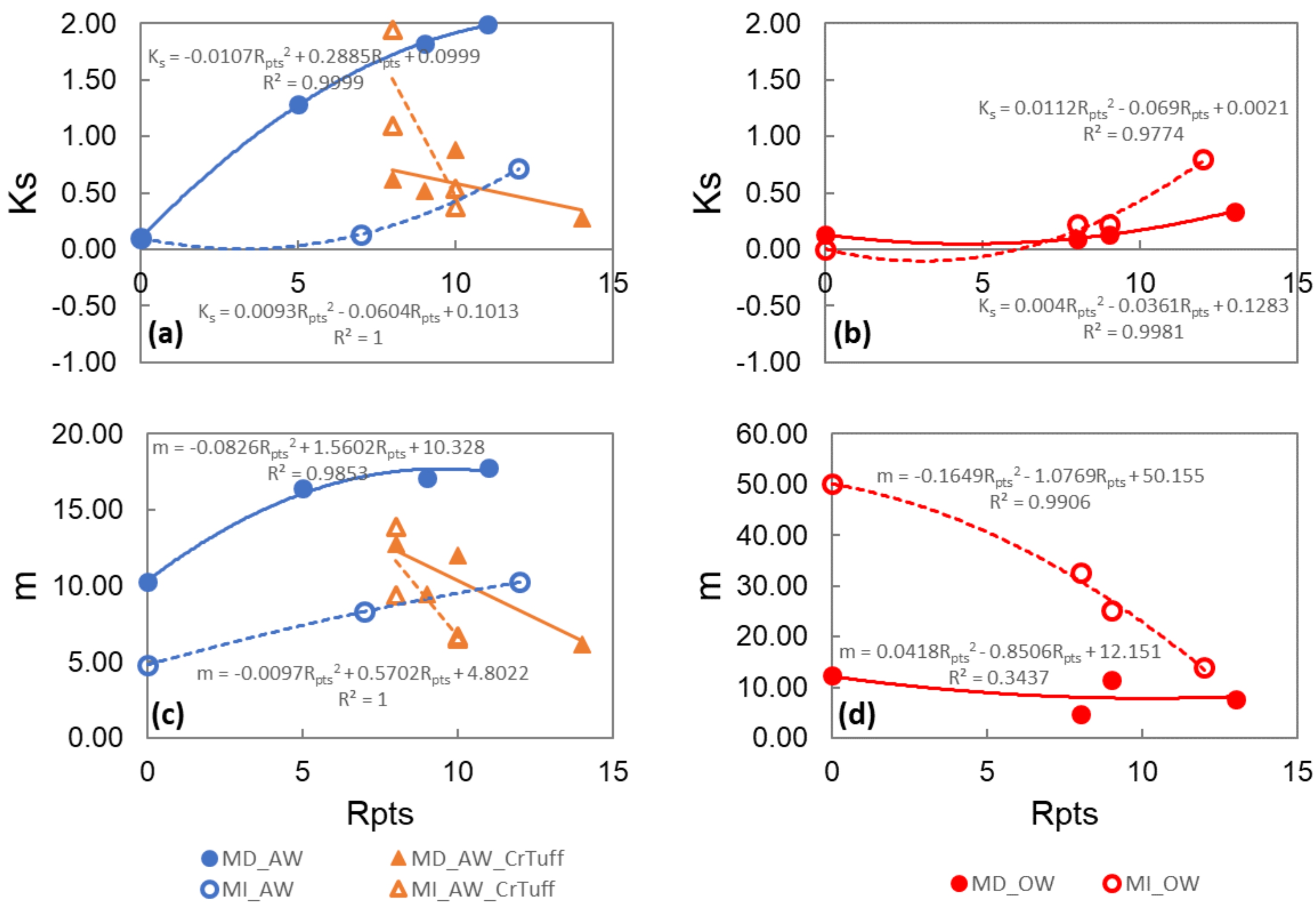

Figure 5-4. Main drainage (solid) and imbibition (dotted) polynomial fits for the $a_{nw}(S_w)$ relationship constants K_s (a,b) and m (c,d) for air-water (left) and oil-water (right) experiments.

The oil-water drainage K_s fit is also fairly similar to the imbibition fit, tending to diverge more at higher R_{pts}. This is not the case for the air-water drainage K_s fit which is equivalent to the imbibition fit when the system is not allowed to relax ($R_{pts} = 0$), but quickly diverges once quasi-equilibrium points are included.

The effect of R_{pts} on the constant m is distinctly different between air-water (Fig. 5-4c) and oil-water (Fig. 5-4d) experiments. This constant describes the concavity of the left-hand side of the $a_{nw}(S_w)$ relationship and therefore is associated with the least amount of confidence as many of the experiments have few points at low saturation. The overall trends show that while the value of m tends to increase with R_{pts} for air-water experiments, m tends to decrease for oil-water experiments. The value for m for the oil-water non-equilibrium main imbibition is also an outlier, with its value being about an order of magnitude larger than drainage. This is not the case for the constant n, which controls the concavity of the right-hand side of the $a_{nw}(S_w)$ relationship. The values for n are nearly independent of R_{pts} for drainage (Fig. 5-3c) and imbibition (Fig. 5-3d) irrespective of fluid pair. This suggests that the number of relaxation points in imbibition or drainage experiments has limited effect on interfacial area generation at high wetting phase saturation, but is a contributing factor to interfacial generation at low wetting phase saturation. Intuitively, this makes sense as fluid films, which are only present at low wetting phase saturation, are assumed to play a significant role in relaxation dynamics of two-phase flow.

Based on the constants from Figs. 5-3 and 5-4, Eq. (5-7)-(5-10) can be used to develop separate empirical $a_{nw}(S_w)$ relationships for air-water and oil-water main drainage and main imbibition experiments in glass bead systems as a function of the number of relaxation point, R_{pts}:

$$\text{AW MD: } a_{nw} = \frac{\left(0.0024R_{pts}{}^2 - 0.059R_{pts} + 0.85\right)S_w(1-S_w)^{0.0008R_{pts}{}^2 - 0.011R_{pts} + 0.75}}{S_w + \left(-0.011R_{pts}{}^2 + 0.29R_{pts} + 0.10\right)(1-S_w)^{-0.083R_{pts}{}^2 + 1.56R_{pts} + 10.3}} \tag{5-7}$$

$$\text{AW MI: } a_{nw} = \frac{\left(0.004R_{pts}{}^2 - 0.083R_{pts} + 1.01\right)S_w(1-S_w)^{0.0024R_{pts}{}^2 - 0.021R_{pts} + 0.83}}{S_w + \left(0.0093R_{pts}{}^2 - 0.06R_{pts} + 0.10\right)(1-S_w)^{-0.0097R_{pts}{}^2 + 0.57R_{pts} + 4.8}} \tag{5-8}$$

$$\text{OW MD: } a_{nw} = \frac{\left(0.0031R_{pts}{}^2 - 0.068R_{pts} + 0.83\right)S_w(1-S_w)^{0.0029R_{pts}{}^2 - 0.04R_{pts} + 0.81}}{S_w + \left(0.004R_{pts}{}^2 - 0.036R_{pts} + 0.13\right)(1-S_w)^{0.042R_{pts}{}^2 - 0.85R_{pts} + 12.2}} \tag{5-9}$$

$$\text{OW MI: } a_{nw} = \frac{(0.0058R_{pts}{}^2 - 0.083R_{pts} + 0.63)S_w(1-S_w)^{0.011R_{pts}{}^2 - 0.13R_{pts} + 0.89}}{S_w + (0.011R_{pts}{}^2 - 0.069R_{pts} + 0.0021)(1-S_w)^{-0.16R_{pts}{}^2 - 1.08R_{pts} + 50.2}} \quad (5\text{-}10)$$

The $a_{nw}(S_w)$ relationships predicted by these empirical expressions are plotted against the experimental data in the supporting information. In Fig. 5-5, Eq. (5-7)-(5-10) are plotted for a range of R_{pts} for air-water (Fig. 5-5a) and oil-water (Fig. 5-5b) experiments. We immediately observe that interfacial area generation is reduced with increasing number of relaxation points. This reduction is independent of fluid flow direction or fluid pair, and corroborates our initial observations, illustrated in Fig. 5-1. Also, as predicted from the trends in the $\mu_{max}(R_{pts})$ relationships, main drainage for air-water experiments always produces less interfacial area than main imbibition over the experimental range of R_{pts}, yet the opposite is true for oil-water experiments. The trend of higher interfacial area production during imbibition has also been reported in numerical simulations using lattice-Boltzmann models [e.g. McClure et al., 2004], using pore network models [e.g. Held & Celia, 2001], using a progressive quasi-static level set method [Prodanović & Bryant, 2006] and some microtomography experiments [e.g. Meisenheimer, McClure, et al., 2020].

We also note that the shape of the $a_{nw}(S_w)$ relationship is similar at high wetting saturation independent of fluid flow direction or fluid pair. This is of course due to a physical constraint as no interfacial area exists at $S_w \sim 1$. Regardless, the shape of the curves are dramatically different at low wetting saturation, especially for the oil-water data, further proving that relaxation at lower wetting saturations has a greater effect on interfacial area generation than at high saturations. There is a sharp peak in the imbibition oil-water data for the $R_{pts} = 4$ curve which is due to the negative K_s value for the fit in Fig. 5-4b. This is most likely non-physical and additional experiments covering a wider range of relaxation points would be needed to generate better predictions at low saturation values. Further experiments with varying fluid pairs would need to be conducted to predict the effect of fluid properties such as interfacial tension, viscosity, and wettability via empirical relationships.

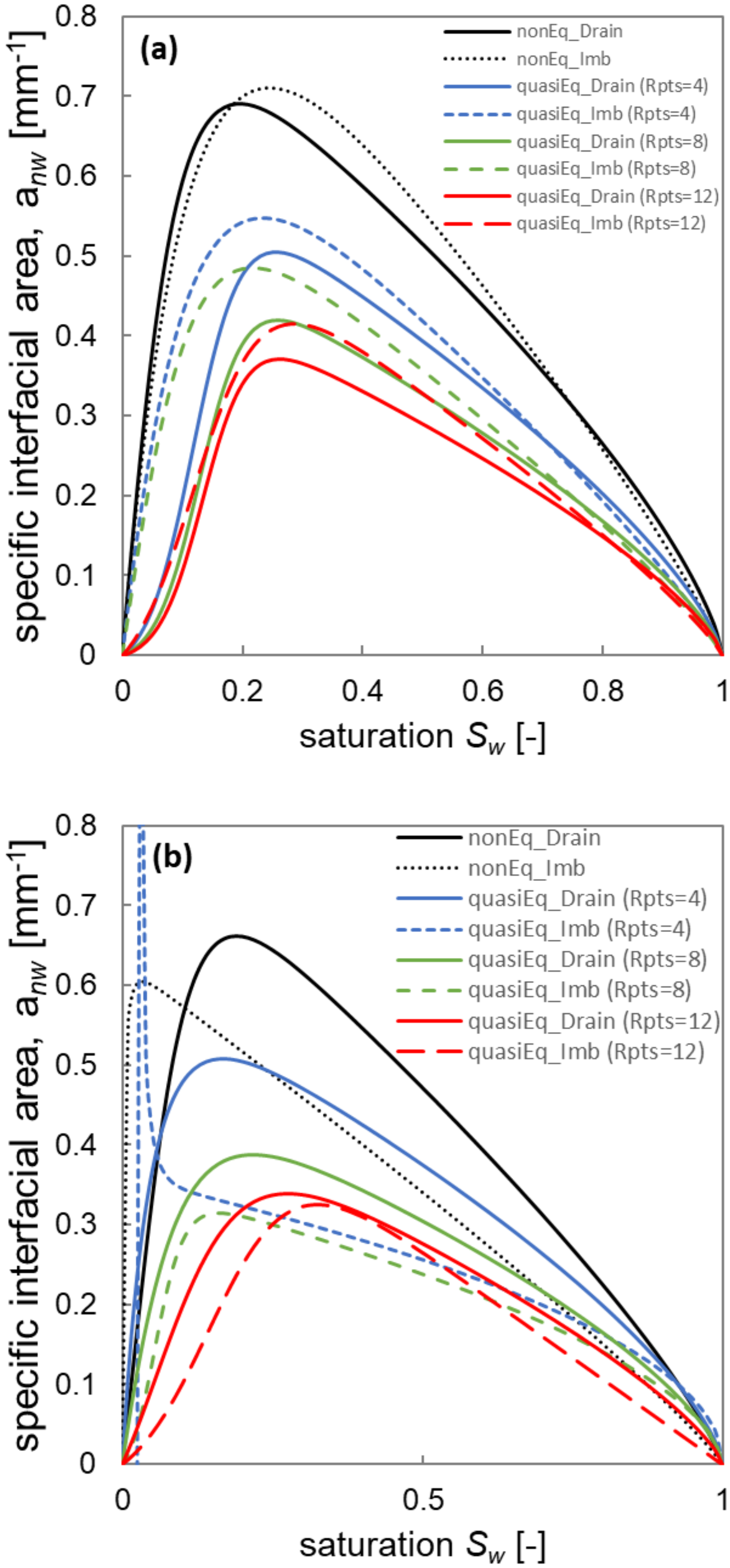

Figure 5-5. Modeled $a_{nw}(S_w)$ data for main drainage (solid lines) and main imbibition (dashed lines) for air-water (a) and oil-water (b) two-phase flow experiments.

5.4.2 Non-equilibrium scanning curve $a_{nw}(S_w)$ relationships

Hysteresis in the $a_{nw}(S_w)$ relationship between main drainage and main imbibition is commonly expected, and is illustrated here by the need for a separate empirical relationship for MD (e.g. Eq. 5-7) and MI (e.g. Eq. 5-8). However, will the predictive methodology presented here also allow for representation of scanning curves, located between the MD and MI curves? The main imbibition and two scanning curves (SI, SI2) for the non-equilibrium air-water data sets [Meisenheimer, McClure et al., 2020] are plotted in Fig. 5-6. The datasets start at a different initial saturation, $S_{w,i}$, on the MD curve ($S_{w,i}$ = 0.12, 0.38, 0.43) and are fitted to Eq. 2 according to Section 5.3.4.

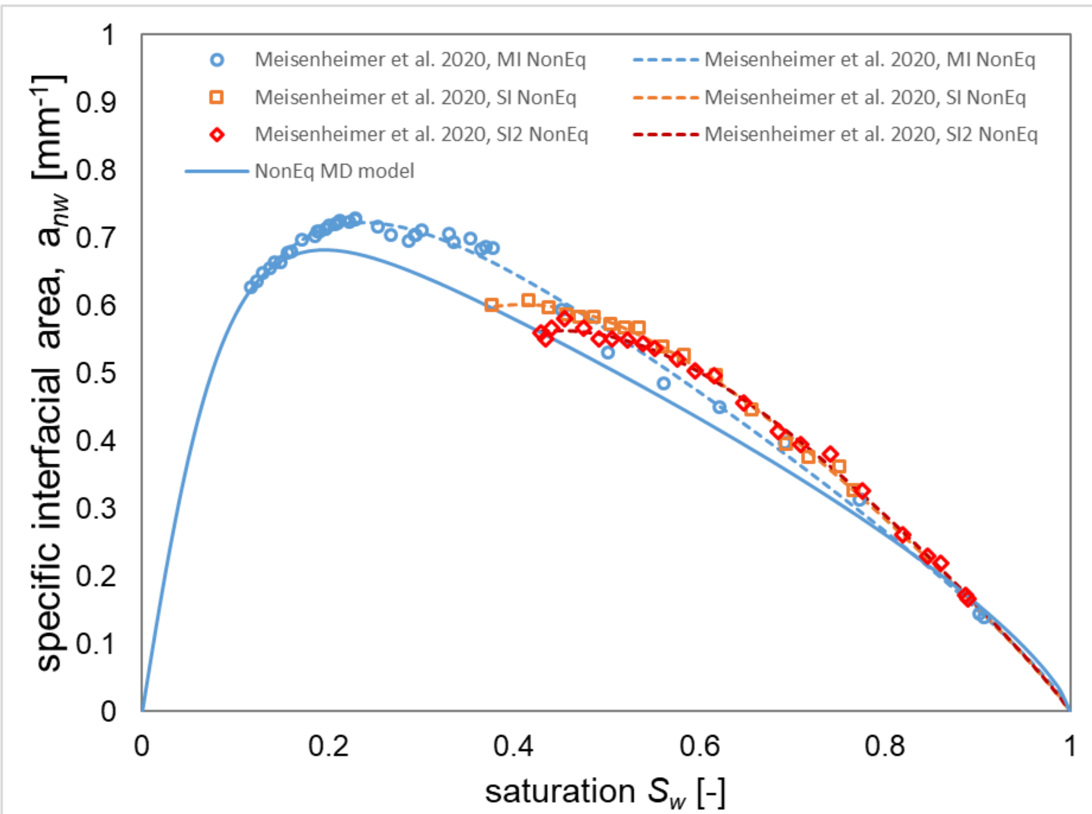

Figure 5-6. Non-equilibrium main imbibition (MI) and imbibition scanning curves (SI, SI2) with fitted empirical $a_{nw}(S_w)$ relationships (dashed lines). The prediction for the main drainage curve (solid line) is included as a reference to show the main drainage/imbibition loop.

The empirical parameters for each $a_{nw}(S_w)$ relationship are included in Table 5-3. Each parameter is plotted in Fig. 5-7 with respect to the initial saturation, shifted by the irreducible wetting saturation, $S_{w,ir}$, and all tend to change linearly with varying $S_{w,i}$. Eq. (5-8) can therefore be generalized and extended to non-equilibrium cases (R_{pts} = 0) to model the complete imbibition air-water $a_{nw}(S_w)$ relationship, including scanning curves. However, the expression is limited to initial saturations, $S_{w,i}$, between irreducible wetting saturation ($S_{w,ir}$ = 0.12) and residual non-wetting phase saturation ($S_{w,r}$ = 0.91):

$$a_{nw,imb} = \frac{(0.83S_{w,i}+0.91)S_w(1-S_w)^{0.27S_{w,i}+0.80}}{S_w+(0.0093S_{w,i}-0.11)(1-S_w)^{-7.04S_{w,i}+5.61}} \; for\ 0.12 \le S_{w,i} \le 0.91 \tag{5-11}$$

It would be beneficial to generate a general $a_{nw}(S_w)$ relationship for the drainage non-equilibrium case as well, but only one scanning curve (SD) exists for drainage, and provides insufficient information to generate an accurate prediction. Fig. 5-9a in the supplementary information shows the non-equilibrium drainage data, with both the MD and SD curves lacking low-wetting phase saturation data. Also, the SD curve has a different overall shape than can be fitted by Eq. (5-2), and therefore a modified version would need to be developed. Further work would be needed with a full main drainage dataset and multiple scanning curves to develop a general $a_{nw}(S_w)$ relationship for non-equilibrium drainage similar to Eq. (5-11).

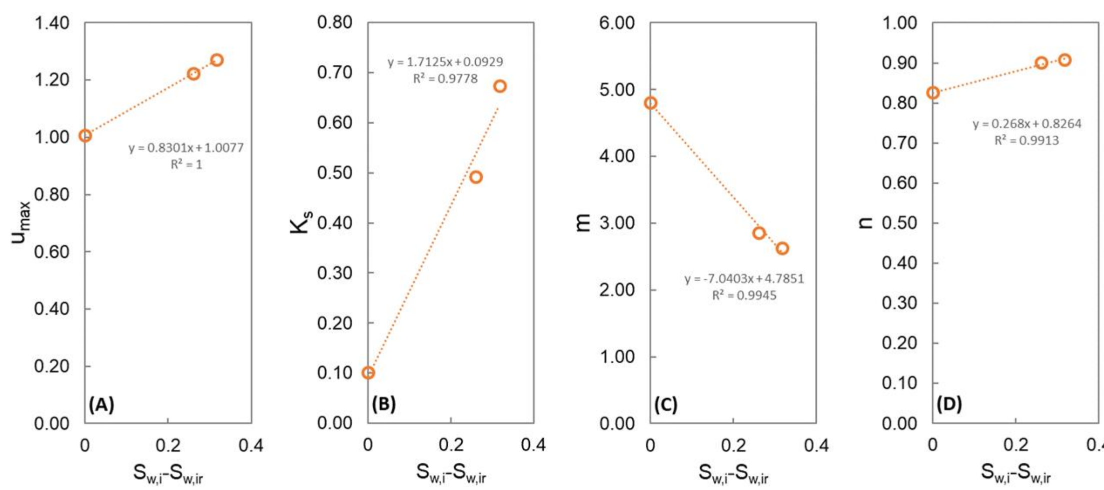

Figure 5-7. Linear fits to the the $a_{nw}(S_w)$ relationship constants for the non-equilibrium (R_{pts} = 0) air-water main and scanning imbibition curves. The empirical constants are plotted against the initial wetting saturation of the curve ($S_{w,i}$) shifted by the irreducible wetting saturation, $S_{w,ir}$.

5.4.3 The effect of porous medium on empirical $a_{nw}(S_w)$ relationships

Figs. 5-3 and 5-4 also include a group of air-water experiments [Wildenschild & Prodanovic, 2009] performed in a different porous medium, crushed tuff, to explore the effect of the type of porous medium on the empirical $a_{nw}(S_w)$ relationships. Interestingly, the trends for μ_{max} in Fig. 5-3a for the crushed tuff data seem to follow the same trends as the air-water glass bead data, except that imbibition is located slightly above drainage. From this we can conclude that maximum interfacial generation is dependent on the porosity of the medium and not the other aspects of the medium (surface roughness, pore size, etc.).

This is not the case for the constant, n, which appears to depend on the properties of the porous medium, as the crushed tuff data has much lower n than the glass bead air-water data in Fig. 5-3c. The magnitude of n controls the slope of the $a_{nw}(S_w)$ curve at high wetting saturations, with smaller values contributing to a flatter curve as exemplified by the crushed tuff data. The fundamental difference between the glass bead and crushed tuff media is the presence of significant surface roughness in the crushed tuff medium [Jansik et al., 2011]. The simulation data in Jiang et al. [2020] also shows that when the surface roughness factor was increased the resulting $a_{nw}(S_w)$ curve was flatter at high wetting saturations. Although the magnitude of n is different than for the glass bead data, the overall trends are similar with imbibition above drainage and the value of n being fairly constant over the range of R_{pts}. Therefore, given one air-water experiment for a specific porous medium, a value for n can be approximated and the value for μ_{max} can be calculated from the glass bead μ_{max}-R_{pts} fit. From these constants, a reasonable fit can be generated to model the $a_{nw}(S_w)$ relationship at mid-high wetting saturations for air-water systems within a range of relaxation points (~0-13).

Unlike μ_{max} and n, the relationships for $K_s(R_{pts})$ (Fig. 5-4a) and $m(R_{pts})$ (Fig. 5-4c) show no resemblance to the glass bead relationships. Because there is a limited range of data for the crushed tuff data, only generalized trends can be observed for K_s and m. Both K_s and m tend to be inversely proportional to R_{pts}. Therefore, the maximum a_{nw} value should be located at a higher wetting saturation for porous media with more surface roughness. The slope of the $a_{nw}(S_w)$ relationship at low saturations would also be steeper for a medium with increased surface roughness. We do indeed observe these trends in Fig. 5-8, and similar trends can also be seen in the simulation data of Jiang et al. [2020]. They also observed an increase in fluid film interfacial area in media with more surface roughness, however the datasets examined in this study were not conducted at sufficiently high image resolution to allow for measurement of interfacial area associated with fluid films.

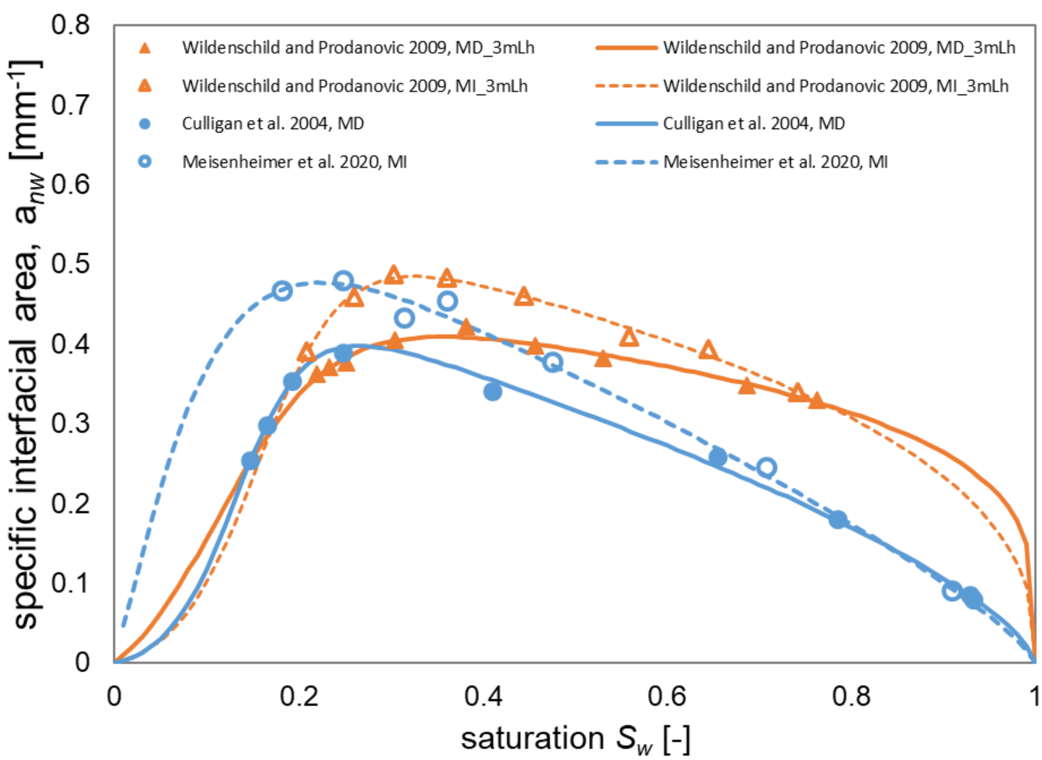

Figure 5-8. Comparison between representative air-water data in a glass bead pack (circles) and crushed tuff (triangles) for main drainage (solid) and imbibition (open), compared to the predicted $a_{nw}(S_w)$ curves for imbibition (dashed) and drainage (solid).

Our findings suggest that separate empirical relationships are needed to model the $a_{nw}(S_w)$ relationship in different types of porous media over a range of relaxation points. Collecting non-equilibrium data can be difficult without access to microtomography facilities specifically built for fast-microtomography, such as the Advanced Photon Source used by Meisenheimer, McClure et al. (2020). But, it is quite feasible to collect data over a range of relaxation points (~5-15 R_{pts}) and follow the approach used here for the glass bead data to predict the non-equilibrium $a_{nw}(S_w)$ relationship for different porous media and fluid pairs.

5.5 Conclusions

Interfacial relaxation in two-phase flow has been shown to affect macroscopic invariants (e.g. specific interfacial area) and, therefore, expressions are needed to describe this effect. We present empirical relationships that can be used to predict the $a_{nw}(S_w)$ relationship in two-phase flow systems. These relationships were derived from data from a variety of existing experiments conducted using a varying number of relaxation points. Due to the inherent hysteresis present in $a_{nw}(S_w)$ relationships, a different empirical relationship was developed for main drainage and main imbibition. These empirical relationships were generated for air-water systems and oil-water systems to study the effect of fluid pair on the $a_{nw}(S_w)$ relationships under varying relaxation conditions. We show that for air-water experiments, interfacial area generation is lower for the main drainage $a_{nw}(S_w)$ curve than for main imbibition, regardless of the degree of relaxation in the system, while the opposite is true for oil-water experiments. Yet, independent of fluid pair, interfacial area generation is decreased as increasing relaxation is allowed in the system. We also found that relaxation generally has a greater effect on interfacial generation at lower wetting saturations than at high saturations. This is likely due to wetting films that are expected to be present at low saturations. A general relationship that can predict air-water imbibition $a_{nw}(S_w)$ curves for the non-equilibrium case was also developed. This, however, relies on information about the initial wetting saturation, which can then be used to fill in the area between the main drainage and imbibition curves. Finally, we predicted the empirical $a_{nw}(S_w)$ relationship for a few air-water experiments in crushed tuff, and it was concluded that a separate relationship is needed for different porous media. Interestingly, the only fitting parameter that is consistent among the studied porous media, is the parameter that controls the maximum interfacial area observed in the system. Therefore, the porosity of a porous medium is a main factor that controls the maximum interfacial area achievable rather than other parameters such as surface roughness.

As demonstrated, the present study provides important insights regarding the effect of relaxation on interfacial generation. Yet, it is important to keep in mind the limitations of the work presented here in terms of type of porous media, and fluid pairs studied. And there are a few points that need to be addressed to expand the methodology to more general scenarios; (i) experiments with fluid pairs with different interfacial tensions are needed to expand the empirical $a_{nw}(S_w)$ relationships to include a reliable dependence on fluid properties. (ii) further studies in different porous media are needed to fully comprehend which characteristic of a porous medium affects interfacial area generation the most under varying relaxation conditions. One interesting outcome of this study is that one could imagine the possibility of "designing" flow scenarios that would allow for generating a particular amount of interfacial area, once a predictive relationship is established for the system of interest.

5.6 Acknowledgements

This work was supported by the U.S. National Science Foundation, Hydrologic Sciences Program under award #1344877. This work was performed at GeoSoilEnviroCARS (The University of Chicago, Sector 13), Advanced Photon Source (APS), Argonne National Laboratory. GeoSoilEnviroCARS is supported by the National Science Foundation - Earth Sciences (EAR - 1634415) and Department of Energy- GeoSciences (DE-FG02-94ER14466). This research used resources of the Advanced Photon Source, a U.S. Department of Energy (DOE) Office of Science User Facility operated for the DOE Office of Science by Argonne National Laboratory under Contract No. DE-AC02-06CH11357.

5.7 Supplementary Information

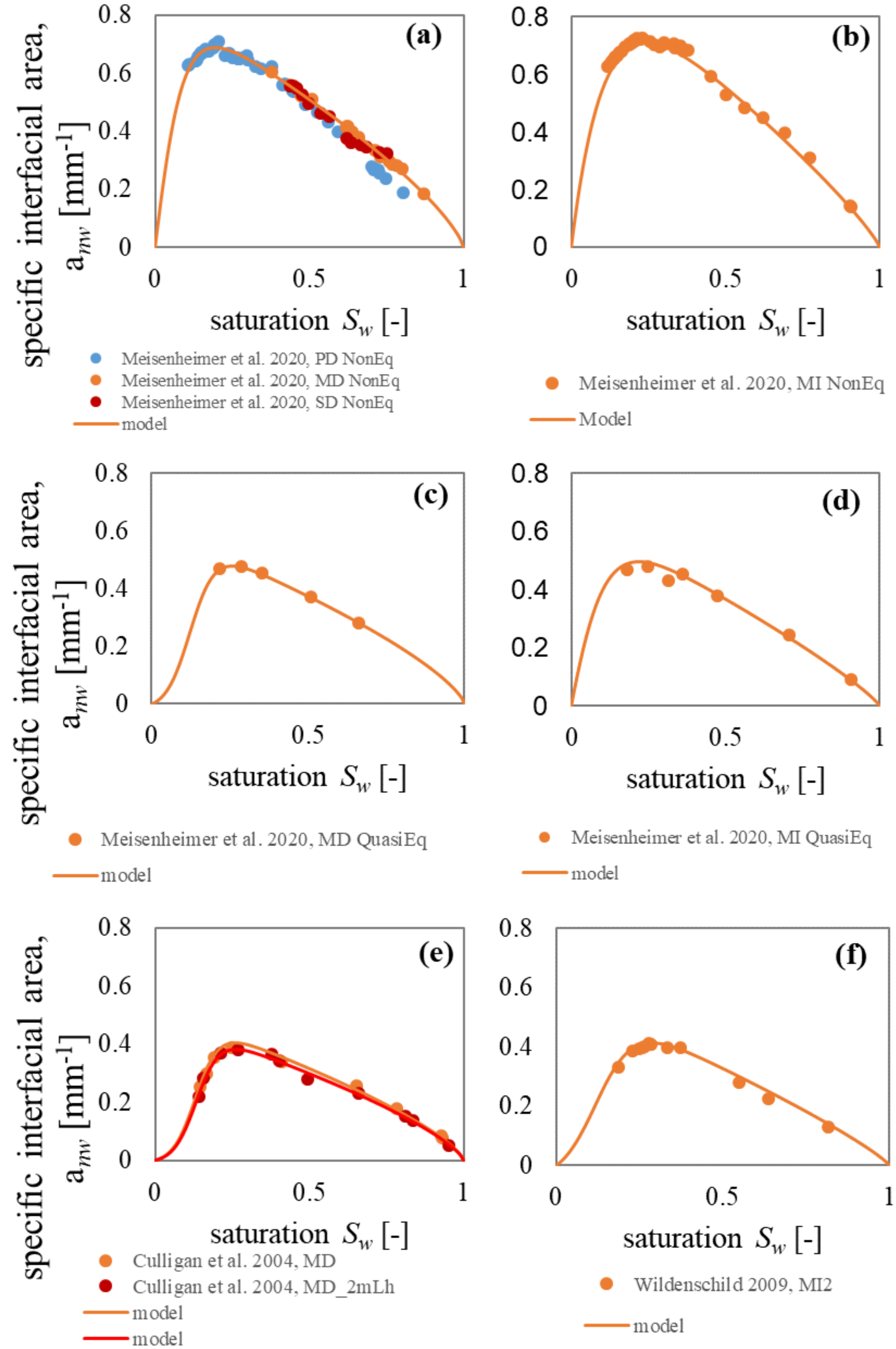

(Continued)

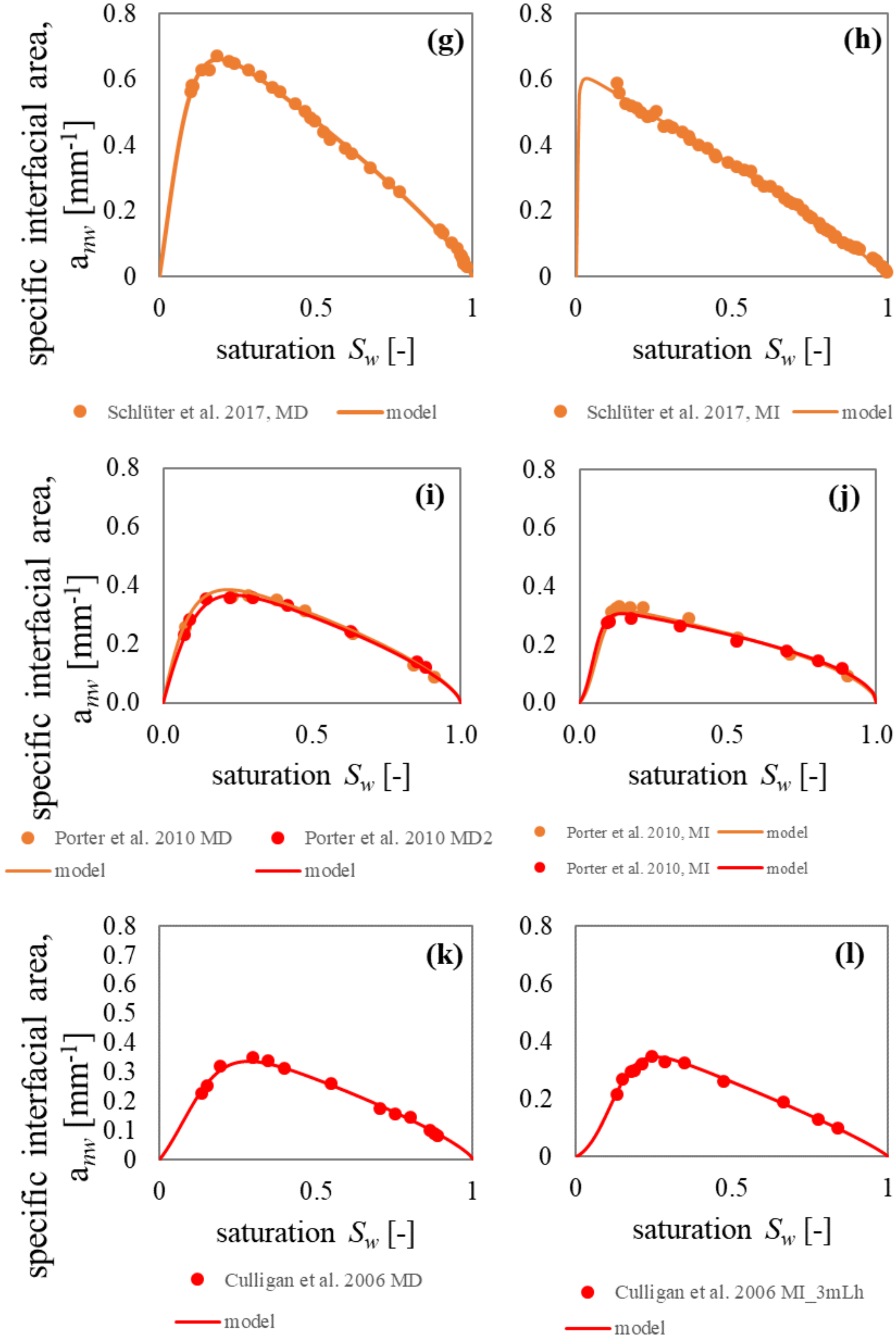

Figure 5-9. Experimental data plotted with the corresponding modeled $a_{nw}(S_w)$ relationship for the number of relaxation points in the experiment.

Chapter 6. Bubbles and two-phase flow constitutive relationships

Douglas E. Meisenheimer[1] and Dorthe Wildenschild[1]

1. School of Chemical, Biological, and Environmental Engineering, Oregon State University, Corvallis, Oregon, U.S.A.

International Journal of Multiphase Flow, Elsevier Ltd.
The Boulevard, Langford Lane, Kidlington, Oxford OX5 1GB, UK
Submittal expected April 2020

6.1 Abstract

Bubbles are used in many multiphase flow engineered systems including for use in stripping volatile compounds from solution and increase dissolved gas concentration for increased yields in chemical and biological systems. It is apparent that models need to be generated and tested to understand the effect of bubble formation and transport on multiphase flow so that that these processes can be predicted for more efficiently engineered systems. A theory of interest in the multiphase flow literature is the use of constitutive relationships between geometric state variables (i.e. fluid curvature, saturation, interfacial area, and Euler characteristic) to uniquely predict the state of a two-fluid flow system. The $V_n(\acute{a}_{nw}, \acute{J}_{\mathrm{nw}}, \acute{\chi}_n)$ relationship, based on the Minkowski-Steiner formula, was found to uniquely predict the state of a two-phase system independent of bubble formation or whether the system is under quasi- or non-equilibrium flow conditions.

6.2 Introduction

Bubble generation and transport controls many environmental engineering process within the subsurface. Environmental production or mobilization of gas can occur in processes such as biogenic production of methane in peats [e.g. Beckwith & Baird, 2001; Chen & Slater, 2015], exsolution of gases during methanogenesis in organic rich aquifers [Fortuin & Willemsen, 2005], and leakage from geologic CO_2 storage systems [e.g. Oldenburg & Unger, 2003; Zuo et al., 2017]. Engineered systems in the subsurface such as in-situ air sparging in conjunction with soil vapor extraction [e.g. Bass et al., 2000; Johnson et al., 1993; Li et al., 2014] and electrical resistance heating [e.g. Hegele & Mumford, 2014; Kingston et al., 2010] both utilize mass transfer to strip volatile organic compounds from contaminated groundwater to produced gas bubbles which are then transported through buoyancy to extraction points. Air sparging can also be used to enhance bioremediation of groundwater contaminated with low-volatility compounds by increasing the dissolved oxygen availability in the groundwater for aerobic metabolism of the contaminant [Brown et al., 1994].

In multiphase systems, it is important to be able to predict the transport of bubbles for accurate multiphase flow models. Predominately, bubbles transporting within pore bodies or those that have become entrapped restrict the hydraulic conductivity of multiphase systems [e.g. Beckwith & Baird, 2001; Hunt & Manga, 2003]. This disruption of flow within porous media, can have other compounding effects on the efficiency of engineered systems such as retarding dissolved oxygen for bioremediation [Fry et al., 1995]. There has been concerted effort in numerical modeling of bubble transport with continuum multiphase models such as TOUGH2 [Pruess et al., 1999] and NUFT [Hao et al., 2012] for a variety of applications such as CO_2 storage [Johnson et al., 2004] and air sparging [Geistlinger et al., 2009]. These continuum models are developed as an extension of Darcy's law and therefore are generally unable to capture the behavior of dynamic gas flows that are not described by stable displacement or continuous channels [Molnar et al., 2019]. Invasion percolation models have also been employed which are generally more equipped to model unstable gas flow [e.g. Glass & Yarrington, 2003; Krol, Mumford, Johnson, & Sleep, 2011].

Empirical relationships between state variable of a multiphase system have also been used to model multiphase flow. The well-known hysteretic capillary pressure-saturation (P_c-S_w) relationship is one such example. There have been many studies which try to expand the P_c-S_w relationship to remove its dependence on the history of the system. One such multiphase flow theory introduces thermodynamically derived specific interfacial area (a_{nw}) as a state variable to extend the P_c-S_w relationship to better describe the system [Hassanizadeh & Gray, 1993]. Pore-network models [e.g. Held & Celia, 2001; Joekar-Niasar & Hassanizadeh, 2011], micromodel experiments [e.g. Cheng et al., 2004; Pyrak-Nolte et al., 2008] and microtomography experiments [Porter et al., 2010] have verified that the $P_c(S_w, a_{nw})$ relationship can uniquely describe two-phase flow under quasi-equilibrium condition. This is not the case for non-equilibrium conditions where the $P_c(S_w, a_{nw})$ relationship was found to be hysteretic in micromodel [Godinez-Brizuela et al., 2017] and microtomography [Meisenheimer, McClurre et al., 2020] experiments. Other studies have further extended this relationship to include Euler characteristic, a measure of the connectivity of the fluid configurations within the pore space. Both lattice Boltzman simulations [McClure et al., 2018] and fast microtomography experiments [Meisenheimer, McClurre et al., 2020] have shown that this geometric state function, $\acute{J}_{nw}(S_w, \acute{a}_{nw}, \acute{\chi}_n)$, uniquely predicts mean curvature (J_{nw}) from the other geometric state variables for both quasi- and non-equilibrium conditions.

While the geometric state function can predict the state of a two-fluid flow system under different flow conditions, the addition of bubble transport has not been tested. This study will explore whether the geometric state function is still unique with the inclusion of bubble generation and transport under quasi- and non-equilibrium two-fluid flow.

6.3 Materials and Methods

6.3.1 Fast X-ray microtomography setup and bubble generation

All experiments were performed at the Advanced Photon Source on the GSECARS 13-BMD beamline using pink-beam fast microtomography (fast µCT). The experiments that didn’t include bubble formation [Meisenheimer, McClure et al., 2020] were performed under the recommended conditions presented by Meisenheimer, Rivers & Wildenschild [2020] with a 1.0 mm copper in-line filter and platinum mirror angled at 1.5 mrad to modify the white beam of the synchrotron to a pink-beam with X-ray intensities predominately in the range of 40-60 keV.

The experiments that included bubble generation and transport used a pink-beam with a higher flux of low-energy X-rays to induce bubble formation through hydrolysis. Fig. (6-1) shows an example of a bubble that has formed near a developing fluid front within the porous media. Bubbles were generated by modifying the pink-beam setup with a 1.0 mm titanium in-line filter and a platinum mirror angled at 2.0 mrad for an X-ray beam intensity predominately in the range of 25-50 keV. Gas volume from bubbles was generated at an average rate of $8.7 \cdot 10^{-4}$ cm^3/min.

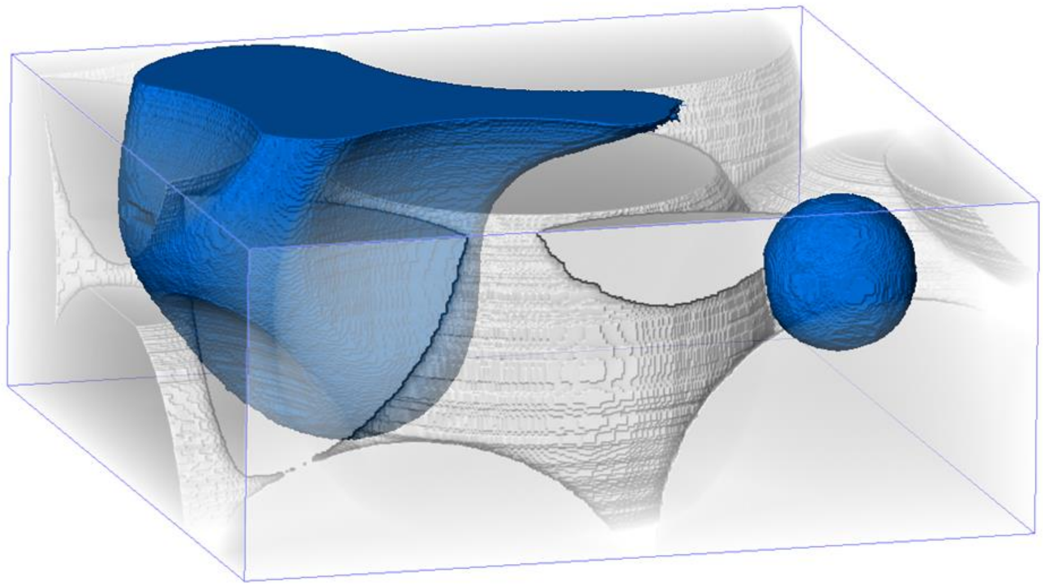

Figure 6-1. Gas bubble trapped near a developing fluid front during primary drainage in a glass bead pack.

6.3.2 Fluid flow experimental setup

All experiments were performed in soda-lime glass bead (0.8-1.2 mm) that were randomly packed and sintered in 6 mm diameter borosilicate glass columns. The two-fluid flow experiments were conducted with water (doped with a 1:6 ratio of potassium iodide for image contrast) and air. The wetting phase (water) flow rate was controlled by a Harvard Apparatus PhD 2000 precision syringe pump which induced the flow of the non-wetting phase (air). A flow rate of 0.2 mL/hr was used for all experiments, which corresponded to a capillary number (Ca) of $2 \cdot 10^{-7}$. For each experiment, the porous medium was initially saturated with wetting phase followed by primary drainage (PD), a main imbibition/drainage loop (MI/MD), and at least one imbibition and drainage scanning curve (SI,SD). For the non-equilibrium experiments, flow was continuous for each drainage or imbibition experiment. Whereas, the flow during the quasi-equilibrium experiments was periodically stopped for 15 min to allow the fluid interfaces to relax. Interfacial relaxation can occur over several hours [Gray et al., 2015; Schlüter et al., 2017], but the majority of saturation and pressure equilibration occurs within the first few minutes. A μCT scan was collected every minute during flow and relaxation periods.

The experiments were collected in different glass bead columns with an average porosity of 0.375 ± 0.01. More details on the experimental setup including image processing and state variable calculation are presented in Meisenheimer, McClure et al. [2020].

6.3.3 Estimating hysteresis of constitutive relationships

Traditionally, the $P_c(S_w, a_{nw})$ relationship was fitted with a bi-quadratic polynomial to the experimental data [e.g. Joekar-Niasar, 2008; Porter et al., 2010]. Hysteresis was estimated by fitting surfaces to the drainage and imbibition data separately and then measuring the error between the surfaces. While this methodology is useful and supplies readily presentable visualizations of the constitutive relationships, it is unable to extend to the higher dimensionality of the geometric state function.

The geometric state function is based on the generalized form of the Minkowski Steiner formula [Federer, 1959; McClure et al., 2018]:

$$dV_n = c_1 A_n dr + c_2 J_n (dr)^2 + c_3 \chi_n (dr)^3 \tag{1}$$

where c_i are coefficients determined by the shape of the non-wetting phase domain and dr is the radius of a small ball. Eq. (1) provides a geometric state relationship that relates a change in the volume of the non-wetting phase (V_n) in terms of the invariant properties of the non-wetting phase: interfacial area (A_n), mean curvature (J_n), and Euler characteristic (χ_n). It is helpful to nondimensionalize these state variables (i.e. $\acute{a}_n$, $\acute{J}_n$, $\acute{\chi}_n$) using the Sauter mean diameter to reduce any weighting factors when measuring error between the experimental data and the model. A modified version of Eq. (1) has been utilized [McClure et al., 2018; Meisenheimer, McClure et al., 2020] to predict the mean curvature of the system using of readily available geometric measures available in thermodynamically constrained averaging theory models, $\acute{J}_{nw}(S_w, \acute{a}_{nw}, \acute{\chi}_n)$. Another version of Eq. (1) was also tested, $V_n(\acute{a}_{nw}, \acute{J}_{nw}, \acute{\chi}_n)$, by Meisenheimer, McClure et al. [2020] which better represents Eq. (1) and is not dependent to a specific porous medium like the relationship with wetting saturation which is dependent on porosity.

The relationships based on Eq. (1) were fitted to locally-smooth spline surfaces using generalized additive models (GAMs) [McClure et al., 2016; Meisenheimer, McClure et al., 2020; Wood & Shaw, 2015]. The error associated of the GAM fit was then used as an estimate of the hysteresis in the relationship, similar to the bi-quadratic fitting method. Two error values were evaluated for each GAM: the coefficient of determination (R^2) and the generalized cross-validation (GCV) value. The R^2 value measures the proportion of variance in the data (a value of unity indicating a perfect fit) and the GCV measures the error of each individual data point if it were not included in the construction of the GAM (a small value indicating a better fit).

6.4 Results and Discussion

6.4.1 Bubble generation effect on state variables

Fig. (6-2) shows the state variable (P_c, a_{nw}, χ_n) relationships with respect to wetting saturation for the quasi- and non-equilibrium cases for both with and without bubble formation. As can be seen from Fig. (6-2a) and (6-2b) the $P_c(S_w)$ relationship is minimally affect by bubble formation for either the quasi- or non-equilibrium experiments. The most likely reason for this is because the capillary pressure is measured as an area-average value [Meisenheimer, McClure et al., 2020] and bubbles, which constitute small fluid volumes with respect to the fluid fronts, will not significantly affect the average capillary pressure of the system before joining with the fluid front. This is fairly unsurprising, including the large hysteresis present between the main drainage/imbibition loop, but provides a good measure of consistency of the data sets that were collected in different glass bead columns.

The non-wetting Euler characteristic relationship, on the other hand, is severely impacted by the presence of bubble formation. Both the quasi- (Fig. (6-2e)) and non-equilibrium (Fig. (6-2f)) $\chi_n(S_w)$ data points with bubble formation have a large amount of variance in comparison with the data without bubble formation.

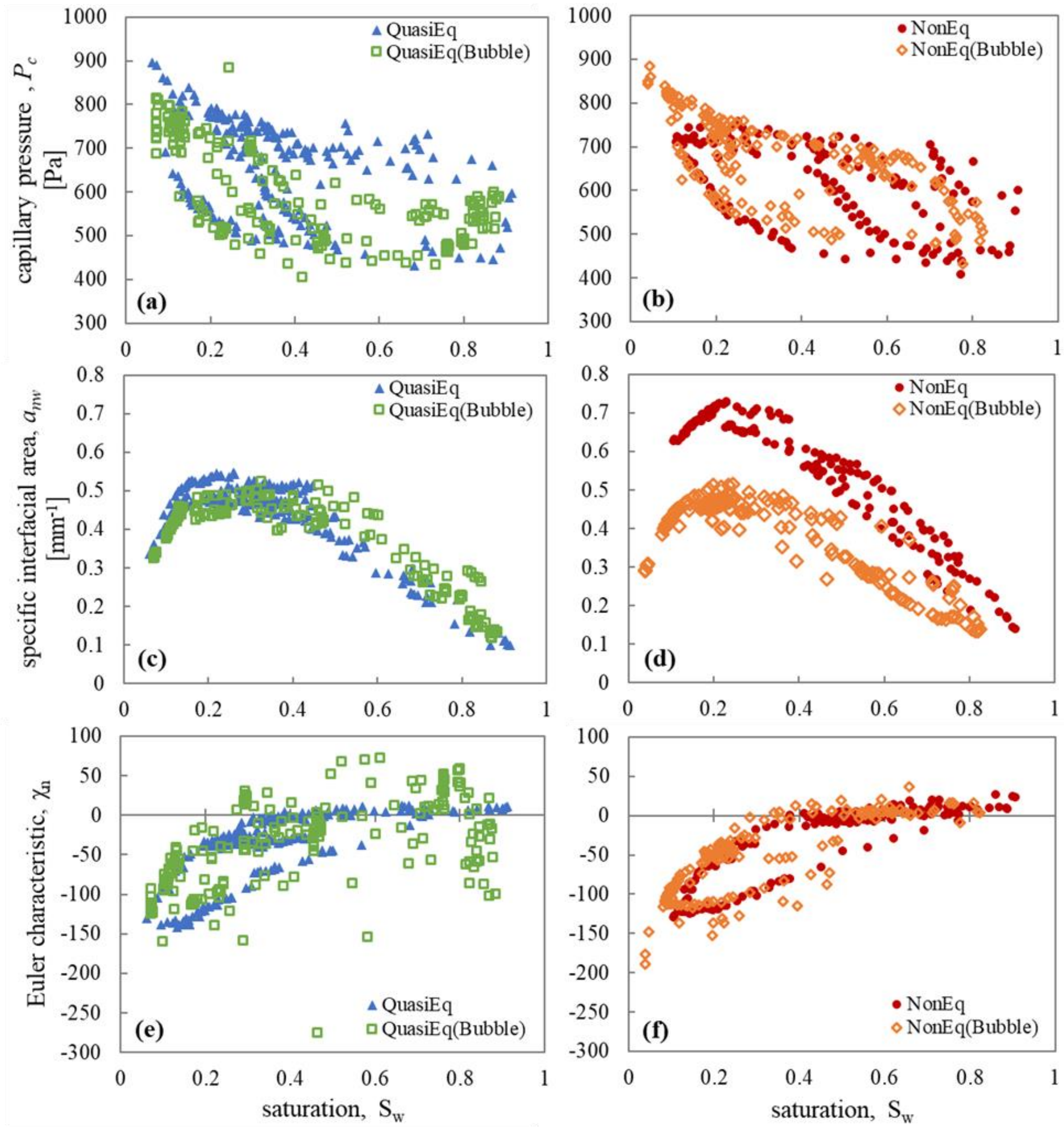

Figure 6-2. Capillary pressure (P_c) vs. wetting saturation (S_w) for (a) quasi-equilibrium and (b) non-equilibrium two-phase flow with (open symbols) and without (closed symbols) bubble formation. Similar plots are presented for the (c,d) specific interfacial area (a_{nw}) vs. S_w and (e,f) Euler characteristic (χ_n) vs. S_w relationships.

Euler characteristic is dependent on the number of distinct non-wetting phase regions. This can be observed in the bubble $\chi_n(S_w)$ relationships which have slightly higher χ_n values on average, indicating more distinct non-wetting regions (i.e. bubbles). But, Euler characteristic is also inversely correlated to the number redundant correlations within the non-wetting regions. Therefore, as bubbles start to fill multiple pore bodies, χ_n will decrease. This can most easily be observed in the quasi-equilibrium bubble experiment (Fig. (6-2e)) at high wetting saturation where there are multiple points that are much more negative than the experiment without bubble formation. Many of these points are from a relaxation period where fluid flow is stopped and bubbles are allowed to start forming large multi-pore connected non-wetting phase regions. Therefore, this balance between bubble formation and coalescence into larger non-wetting phase regions is most likely the cause of the large variance in the bubble data, especially the quasi-equilibrium experiment which had more bubble generation due to interfacial relaxation periods.

The specific interfacial area relationships (Fig. (6-2c) and (6-2d)) are probably the most interesting and unexpected of the state variable relationships. Most noticeably, the non-equilibrium $a_{nw}(S_w)$ relationship for the bubble experiment (Fig. (6-2d)) produces much less interfacial area than the non-equilibrium experiment without bubble formation, to about the same magnitude as the quasi-equilibrium experiment. As has been shown before [Gray et al., 2015; Meisenheimer, McClure et al., 2020; Schlüter et al., 2017], interfacial relaxation reduces the interfacial area within a system to a configuration that is more thermodynamically favorable. It can be assumed that the interfaces of generated bubbles are energetically minimized when they are being transported and subsequently trapped in the porous media. Then, as the invading fluid front connects with trapped bubbles, the interfaces are already in a thermodynamically favorable state resulting in a $a_{nw}(S_w)$ relationship similar to that of the quasi-equilibrium experiment. Also of note, is the fact that the quasi-equilibrium $a_{nw}(S_w)$ relationship (Fig. (6-2c)) with bubble formation produces more interfacial area at high S_w and less interfacial area at low S_w compared to the quasi-equilibrium experiment without bubble formation. The increased a_{nw} at high wetting saturation is due to the increased amount of disconnected non-wetting phase from the bubbles. The lower generation of a_{nw} at low wetting saturation is most likely due to a similar mechanism as the non-equilibrium case. Relaxation of the interfaces is already inherent to the quasi-equilibrium case, but because relaxation occurs over many hours and the interfaces were only allowed 15 minutes of relaxation per quasi-equilibrium point, there is still an effect of the fluid front combining with more thermodynamically favorable disconnected phase configurations and reducing the overall interfacial area.

6.4.2 Capillary pressure, saturation and interfacial area (P_c-S_w-a_{nw}) surfaces

Fig. (6-3) shows the bi-quadratic polynomial surface fits relating capillary pressure, saturation and interfacial area for the quasi-equilibrium (Fig. (6-3a)) and non-equilibrium (Fig. (6-3b)) experiments with bubble formation. The mean squared error of the quasi- and non-equilibrium P_c-S_w-a_{nw} surfaces to the experimental data was $9.96 \cdot 10^{-4}$ and $1.32 \cdot 10^{-3}$, respectively. Although the squared error is relatively low, there is still quite a bit of variance in the data from the surfaces as can be seen in Fig. (6-3). Splitting the drainage and imbibition data and generating separate surfaces (Fig. (6-4)) shows the main cause of this variance. Both the quasi- and non-equilibrium drainage and imbibition surfaces are separated from each other. Table 1 shows the root mean squared error (RMSE) and mean absolute error (MAE) between the drainage and imbibition surfaces for each flow condition, and the error between the unique surfaces (Fig. (6-3)) and the drainage or imbibition surface. With maximum a_{nw} values for both bubble experiments around 0.5 mm^{-1}, the error values between the drainage and imbibition surfaces are comparatively large which indicates a large amount of hysteresis in the relationship.

The hysteresis in the P_c-S_w-a_{nw} surfaces for the non-equilibrium experiment corresponds with other studies [Godinez-Brizuela et al., 2017; McClure et al., 2018; Meisenheimer, McClure, et al., 2020], but the large amount of hysteresis in the quasi-equilibrium experiment is contrary to many studies without bubble formation [e.g. Joekar-Niasar & Hassanizadeh, 2011; Porter et al., 2010; Pyrak-Nolte et al., 2008]. This suggests that bubble formation and entrapment occurs in a manner that cannot be predicted by the $P_c(S_w, a_{nw})$ relationship and further extensions to the constitutive relationship must be made, independent of flow condition.

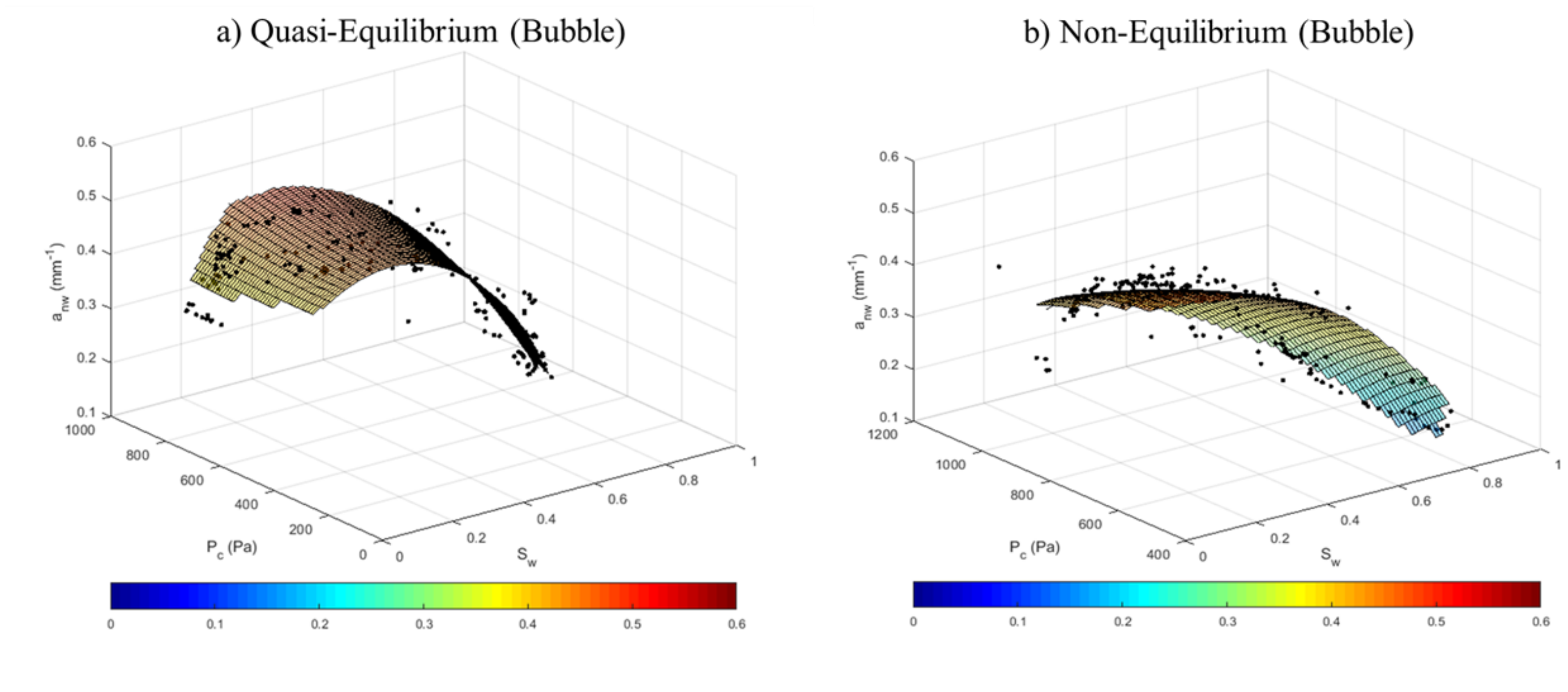

Figure 6-3. P_c-S_w-a_{nw} surfaces for the (a) quasi-equilibrium and (b) non-equilibrium experiments with bubble formation.

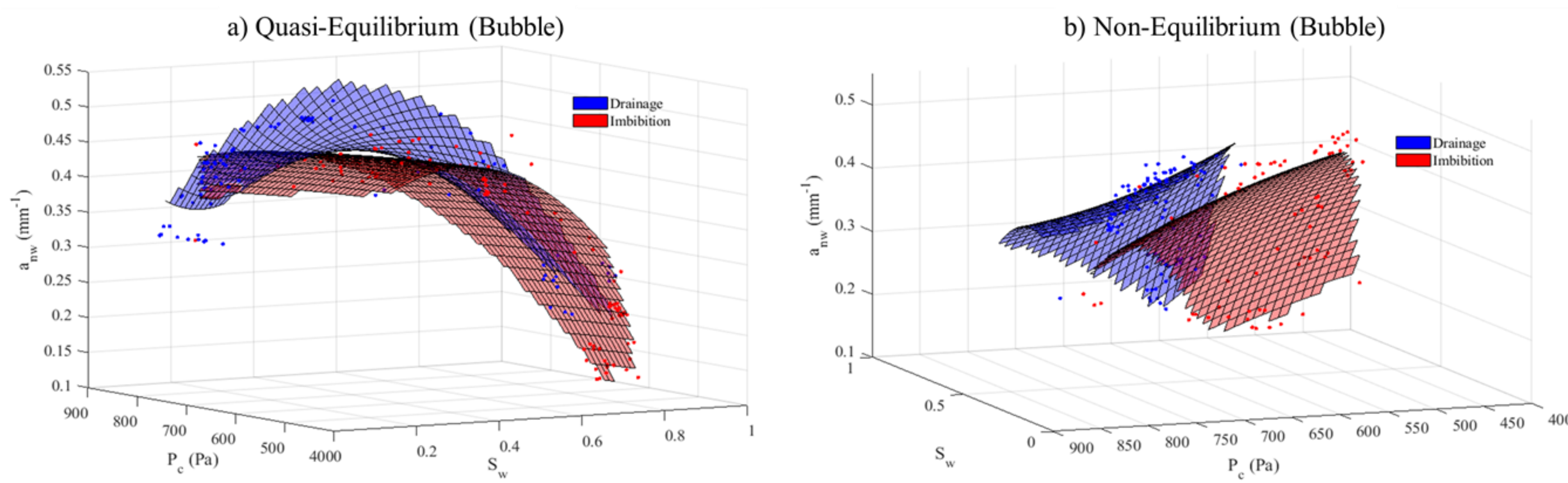

Figure 6-4. Separated drainage (blue) and imbibition (red) P_c-S_w-a_{nw} surfaces for the (a) quasi-equilibrium and (b) non-equilibrium experiments with bubble formation.

Table 6-1. Measured error values between the surfaces presented in Figs. (6-3) and (6-4).

		RMSE [mm^{-1}]	MAE [mm^{-1}]
Quasi-Equilibrium (Bubble)	Drainage/Imbibition	0.046	0.035
	Unique/Drainage	0.029	0.022
	Unique/Imbibition	0.030	0.023
Non-Equilibrium (Bubble)	Drainage/Imbibition	0.069	0.067
	Unique/Drainage	0.015	0.011
	Unique/Imbibition	0.037	0.031

6.4.3 The effect of bubbles on the geometric state function

The constitutive relationships for the quasi- and non-equilibrium bubble experiments were modeled using GAMs and the associated error in those relationships are presented in Fig. (6-5). The $\acute{J}_{nw}(S_w)$ relationship, unsurprising, is highly hysteretic in nature with only 58% of the variance in the data explained by the relationship for both flow conditions. Including interfacial area, the $\acute{J}_{nw}(S_w, \acute{a}_{nw})$ relationship also is hysteretic with the quasi-equilibrium bubble data having a higher magnitude of hysteresis present in the system (R^2 = 0.73, GCV = 0.053) compared to the non-equilibrium bubble data (R^2 = 0.82, GCV = 0.031). This corroborates with the error values seen with the construction of the polynomial surfaces where hysteresis is present but the ability of the $\acute{J}_{nw}(S_w, \acute{a}_{nw})$ relationship to predict the state of the system is more adversely affect by bubble formation under quasi-equilibrium conditions. This observation that bubble formation more greatly affects quasi-equilibrium data is confirmed when comparing with the experimental data without bubble formation (quasiEq: R^2 = 0.89, GCV = 0.022; nonEq: R^2 = 0.85, GCV = 0.026) from Meisenheimer, McClure et al. [2020]. Again, this is most likely due to the fact that the quasi-equilibrium data experienced more bubble formation due to its inclusion of interfacial relaxation periods.

When the constitutive is further extended to include Euler characteristic, the ability of the relationship to predict the state of the system is increased as seen previously in studies without bubble formation [McClure et al., 2018; Meisenheimer, McClure, et al., 2020]. Interestingly, the non-equilibrium bubble data and non-bubble data from Meisenheimer, McClure et al. have nearly the same error associated with the $\acute{J}_{nw}(S_w, \acute{a}_{nw}, \acute{\chi}_n)$ GAM fit (R^2 = 0.95, GCV = 0.01). This is not the cases for the quasi-equilibrium data where only 80% of the variance in the bubble experiment is explained by the GAM fit compared to 98% in the experiment without bubble formation. Thus, further solidifying the observation that bubble formation has a greater impact on the variance of the quasi-equilibrium data. In future work it would be important to distinguish whether this effect is entirely due to the fact that the quasi-equilibrium data has more bubble generation or if some other factor is at play by better engineering the experimental design for equal bubble generation between the flow conditions.

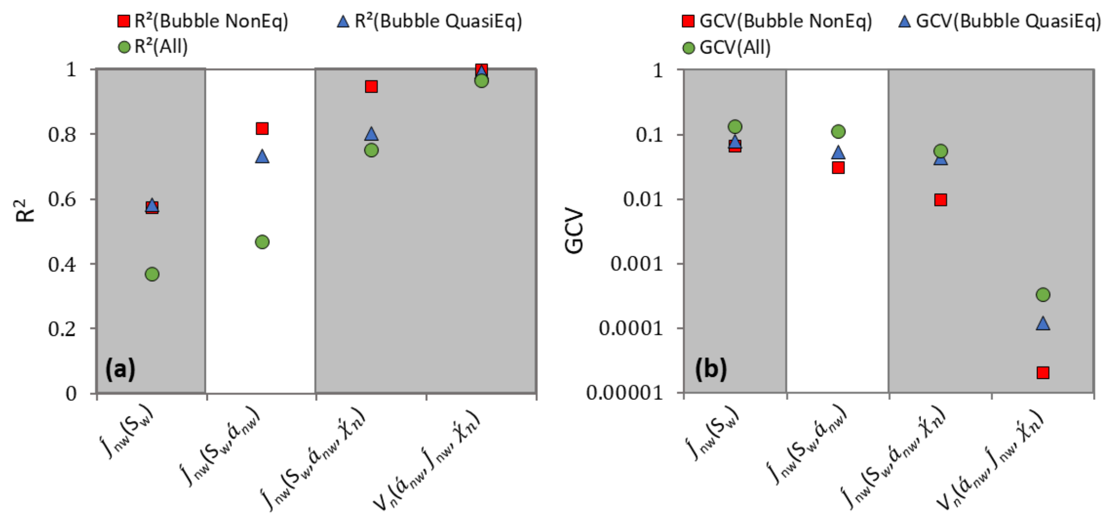

Figure 6-5. Associated quasi- and non-equilibrium (a) R^2 and (b) GCV error values for GAM fits for various constitutive relationships. A combined dataset ("All") is also presented which combines all the quasi- and non-equilibrium data with and without bubble formation [Meisenheimer, McClure et al., 2020]. Large R^2 and small GCV values indicates a better fit.

As with the experiments without bubble formation, the $V_n(\acute{a}_{nw}, \acute{J}_{nw}, \acute{\chi}_n)$ relationship was also tested. As can be seen in Figure (6-5), both the quasi- and non-equilibrium GAM fits for the bubble experiments provided statistically unique predictions of the state of the system (quasiEq: $R^2 = 0.993$, GCV = $1.19{\cdot}10^{-4}$; nonEq: $R^2 = 0.998$, GCV = $2.06{\cdot}10^{-5}$). Thus suggesting that the constitutive relationship more closely representing the Minkowski-Steiner formula is able to predict the state of a two-phase system.

The bubble and non-bubble data were combined into one dataset ("All" in Fig. (6-5)) to see if these conclusion still hold independent of flow condition. As was seen in Meisenheimer, McClure et al. [2020]; the combined data set cannot explain the variance in the data as well for the most of the constitutive relationships except for the $V_n(\acute{a}_{nw}, \acute{J}_{nw}, \acute{\chi}_n)$ relationship ($R^2 = 0.97$, GCV = $3.0{\cdot}10^{-3}$) which has associated error well within experimental error. Therefore, it can be concluded that the $V_n(\acute{a}_{nw}, \acute{J}_{\mathrm{nw}}, \acute{\chi}_n)$ relationship can uniquely predict the state of the system independent of flow condition and bubble formation. This inherently makes sense because the Minkowski-Steiner formula is used to predict the fluid configuration within a porous media based on intrinsic state variables. Therefore, any fluid interface generated in the system (independent of whether it was generated by multiphase flow or through bubble transportation) should be geometrically viable and predicted by the $V_n(\acute{a}_{nw}, \acute{J}_{\mathrm{nw}}, \acute{\chi}_n)$ relationship.

6.5 Conclusions

Bubble formation and transport within porous media has many applications within environmental engineering, but many models are unable to predict the state of a multiphase system due to the transient nature of bubble transport. We present the use of a constitutive relationship, $V_n(\acute{a}_{nw}, \acute{J}_{\mathrm{nw}}, \acute{\chi}_n)$, based on the Minkowski-Steiner formula to predict the state of a two-phase flow system in glass beads based on invariant geometric state variables. We found that this relationship uniquely predicts the state of the system independent of bubble formation or whether the system is under quasi- or non-equilibrium flow conditions. This is not the case for lower dimensional relationships, such as the $P_c(S_w, a_{nw})$ relationship, which have been previously been proven to be non-hysteretic without bubble transport. Therefore, the $V_n(\acute{a}_{nw}, \acute{J}_{\mathrm{nw}}, \acute{\chi}_n)$ relationship is a more general solution that can predict two-phase flow systems over a more wide variety of circumstances.

Although this is the case for the studied air-water glass bead system, there is some future work that is needed to further extend the applicability of this constitutive relationship. Experiments in more diverse and environmentally applicable porous media would be needed to study the effect of porous media, such as surface roughness, on this relationship. Also, it was assumed that the fluid characteristics between the air and the x-ray generated bubbles were similar, allowing the grouping of the two gas phases into one non-wetting phase. Further experiments would be needed to identify whether if the fluid characteristics of the gas phases (interfacial tension, viscosity, wettability, etc.) were more different then the $V_n(\acute{a}_{nw}, \acute{J}_{\mathrm{nw}}, \acute{\chi}_n)$ relationship would still be able to uniquely predict the state of the system.

6.6 Acknowledgements

This work was supported by the U.S. National Science Foundation, Hydrologic Sciences Program under award #1344877. This work was performed at GeoSoilEnviroCARS (The University of Chicago, Sector 13), Advanced Photon Source (APS), Argonne National Laboratory. GeoSoilEnviroCARS is supported by the National Science Foundation - Earth Sciences (EAR - 1634415) and Department of Energy- GeoSciences (DE-FG02-94ER14466). This research used resources of the Advanced Photon Source, a U.S. Department of Energy (DOE) Office of Science User Facility operated for the DOE Office of Science by Argonne National Laboratory under Contract No. DE-AC02-06CH11357.

Chapter 7. Summary and Conclusions

7.1 Research Summary

The research presented in this dissertation has focused on developing an improved understanding of the effect that relaxation of fluid interfaces and bubble formation has on state variable invariants of two-phase flow. This was accomplished in an effort to verify the validity of two-phase flow constitutive relationships under a variety of conditions to better predict multiphase systems in the environment and engineered systems. Specifically, the objectives of this research were to:

1. Develop a fast x-ray microtomography methodology at the Advanced Photon Source 13-BMD beamline to image non-equilibrium two-phase flow.

2. Collect 3-dimensional µCT data for quasi- and non-equilibrium flow with and without bubble formation and transport

3. Investigate the effect of bubble formation and flow condition of the two-phase flow state variables (P_c, S_w, a_{nw}, χ_n).

4. Investigate the effect of fluid relaxation on formation of interfacial area.

5. Test the ability of the state variable constitutive relationships to predict the state of a two-phase system under the various testing situations.

Chapter 3 presented a fast x-ray microtomography technique using pink-beam radiation at the Advanced Photon Source. This fast µCT technique allows for generation of 3-dimensional, high-resolution images of non-equilibrium two-phase flow in an opaque porous medium, a capability that was instrumental for the success of the rest of this work. Chapter 3 also presents guidelines for other researchers to use the technique for dynamic processes of interest (not necessarily constrained to multiphase flow) by presenting a comparison of X-ray beam parameterization to reduce x-ray exposure and hydrolysis effects, and a discussion of image scanning parameterization to optimize image quality and contrast.

Chapter 4 focused on studying quasi- and non-equilibrium air-water flow utilizing the fast µCT technique presented in Chapter 3. In these experiments, µCT images were collected through multiple drainages and imbibitions, as well as during fluid relaxation periods at quasi-equilibrium points, and it was demonstrated that the µCT technique is a powerful tool that allows for collection of 3-dimensional data of dynamic processes in a nondestructive manner. Multiphase state variables (capillary pressure, saturation, interfacial area, Euler characteristic) were measured for each µCT image to track the evolution of these variables, which allowed for comparisons between the quasi- and non-equilibrium flow experiments. Constitutive state variable relationships were tested for the quasi- and non-equilibrium experiments and it was shown that extended $P_c(S_w, a_{nw})$ relationships are needed to predict the state of a two-phase system, agreeing with studies conducted in micromodels and using Lattice-Boltzmann simulations.

In Chapter 5, the interfacial area measurements from Chapter 4 were compared with datasets in the literature to study the effect of fluid relaxation in quasi-equilibrium experiments on interfacial area generation. An empirical relationship was theorized and verified for an $a_{nw}(S_w)$ relationship that was also dependent on the number of quasi-equilibrium relaxation points taken during a drainage or imbibition experiment. It was determined that different relationships would be required depending on the fluids and porous medium, but clear trends were observed which could provide the possibility of engineering multiphase systems that generate a particular amount of interfacial area once a predictive relationship is established for the system.

Finally, Chapter 6 investigated the effect of bubble generation and transport in a porous medium during quasi- and non-equilibrium two-phase flow. Similar to Chapter 4, the effect of bubble transport on multiphase state variables and constitutive relationships was studied. It was determined that higher order constitutive relationships that include descriptions of fluid topology were needed to predict the state of a system independent of flow condition or bubble transport.

7.2 Notable Findings

The results presented in this dissertation provide a methodology for a fast X-ray microtomography technique that can be utilized by a variety of researchers to investigate dynamic processes. From this technique, 3-dimensional two-phase flow experimental data was collected to investigate the effect of equilibration condition and bubble formation on the validity of constitutive relationships to be utilized as predictive tools in multiphase models. Specifically, it was shown that:

- The $\acute{\chi}_n(S_{w,t})$ relationship can uniquely predict the connectivity of a system based on the trapped wetting phase saturation for a specific flow condition. This has significant applications in engineered multi-phase flow situations such as subsurface storage of CO_2 via capillary trapping.

- The geometric state function, $\acute{J}_{nw}(S_w, \acute{a}_{nw}, \acute{\chi}_n)$, uniquely predicts the mean curvature for separate quasi- and non-equilibrium two-phase flow experiments. This is not the case for many lower dimensional constitutive relationships or when bubble formation and transport is present in the porous medium.

- The presented constitutive relationship, $V_n(\acute{a}_{nw}, \acute{J}_{nw}, \acute{\chi}_n)$, can uniquely predict the state of a two-phase system independent of bubble formation or whether the system is under quasi- or non-equilibrium flow conditions.

- While all state variables are affected by fluid relaxation as shown previously [Gray et al., 2015; Schlüter et al., 2017], P_c recovers quickly after relaxation with the quasi-equilibrium points being bounded by the non-equilibrium $P_c(S_w)$ relationship and the $\chi_n(S_w)$ relationships are only slightly different due to increased disconnected phase in non-equilibrium experiments. The quasi- and non-equilibrium $a_{nw}(S_w)$ relationships, on the other hand, are largely different due to the inability of interfacial area to sufficiently recover after each relaxation point.

- An empirical $a_{nw}(S_w)$ relationship, based on the generalized mathematical expression for Monod kinetics with an included dependence on the number of relaxation points in an experiment, can be used to predict interfacial area generation in a system for a given porous medium and fluid pair.

7.3 Future Work

As discussed in the literature review and results presented in this dissertation, there are still a number of open questions that need to be addressed to increase the understanding of differences between quasi- and non-equilibrium flows. It has been demonstrated that the fast μCT methodology presented here is capable of generating novel data that can be used to verify two-phase flow theories and develop predictive tools to help optimize environmental engineering practices. Recommendations for future study to expand the applicability of constitutive relationships to predict two-phase flow systems include the following:

- Further studies in natural porous media would be required to study the effect of various porous media properties such as surface roughness and porosity on the state variables under quasi-equilibrium and non-equilibrium flow conditions.

- Also, experiments with different fluid pairs would be required to determine the effect of interfacial tension, viscosity, and wettability on the state variables as well as expand the $a_{nw}(S_w)$ relationships presented in Chapter 5 to include dependencies on these parameters.

- An experimental design that would allow for the transport of bubbles into the porous medium would expand on the exploratory study in Chapter 6. The effect of generating bubbles throughout the porous medium due to X-ray hydrolysis rather than having the bubbles produced outside of the field of view and possibly constrained to flow paths could affect reported measures of state variables.

Chapter 8. Bibliography

Andrew, M., Menke, H., Blunt, M. J., & Bijeljic, B. (2015). DYNAMIC DRAINAGE AND IMBIBITION IMAGED USING FAST X-RAY MICROTOMOGRAPHY. *International Symposium of the Society of Core Analysts*, (SCA2015-009).

Araujo, J. B., & Brusseau, M. L. (2020). Assessing XMT-Measurement Variability of Air-Water Interfacial Areas in Natural Porous Media. *Water Resources Research*, *56*(1), 1–10. https://doi.org/10.1029/2019WR025470

Armstrong, R. T., McClure, J. E., Robins, V., Liu, Z., Arns, C. H., Schlüter, S., & Berg, S. (2018). Porous Media Characterization Using Minkowski Functionals: Theories, Applications and Future Directions. *Transport in Porous Media*, 1–31. https://doi.org/10.1007/s11242-018-1201-4

Armstrong, R. T., Ott, H., Georgiadis, A., Rücker, M., Schwing, A., & Berg, S. (2014). Subsecond pore-scale displacement processes and relaxation dynamics in multiphase flow. *Water Resources Research*, *50*(12), 9162–9176. https://doi.org/10.1002/2014WR015858

Bass, D. H., Hastings, N. A., & Brown, R. A. (2000). Performance of air sparging systems: a review of case studies. *Journal of Hazardous Materials*, *72*(2–3), 101–119. https://doi.org/10.1016/S0304-3894(99)00136-3

Bear, J. (1988). *Dynamics of Fluids in Porous Media*. Dover Publications, Inc.

Beckwith, C. W., & Baird, A. J. (2001). Effect of biogenic gas bubbles on water flow through poorly decomposed blanket peat. *Water Resources Research*, *37*(3), 551–558. https://doi.org/10.1029/2000WR900303

Berg, S., Armstrong, R., Ott, H., Georgiadis, A., Klapp, S. A., Schwing, A., … Stampanoni, M. (2013). Multiphase flow in porous rock imaged under dynamic flow conditions with fast x-ray computed microtomography. *International Symposium of the Society of Core Analysts*, (SCA2013-011).

Berg, S., Ott, H., Klapp, S. A., Schwing, A., Neiteler, R., Brussee, N., … Stampanoni, M. (2013). Real-time 3D imaging of Haines jumps in porous media flow. *P Natl Acad Sci USA*, *10*(110), 3755–3759. https://doi.org/10.1073/pnas.1221373110

Berg, S., Rücker, M., Ott, H., Georgiadis, A., van der Linde, H., Enzmann, F., … Wiegmann, A. (2016). Connected pathway relative permeability from pore-scale imaging of imbibition. *Advances in Water Resources*, *90*, 24–35. https://doi.org/10.1016/j.advwatres.2016.01.010

Beucher, S., & Lantuejoul, C. (1979). Use of Watersheds in Contour Detection. *International Workshop on Image Processing: Real-Time Edge and Motion Detection/Estimation*, (January 1979), 12–21. https://doi.org/citeulike-articleid:4083187

Blunt, M. J., Bijeljic, B., Dong, H., Gharbi, O., Iglauer, S., Mostaghimi, P., … Pentland, C. (2013). Pore-scale imaging and modelling. *Advances in Water Resources*, *51*, 197–216. https://doi.org/10.1016/j.advwatres.2012.03.003

Bradford, S. A., & Leij, F. J. (1997). Estimating interfacial areas for multi-fluid soil systems. *Journal of Contaminant Hydrology*, *27*(1–2), 83–105. https://doi.org/10.1016/S0169-7722(96)00048-4

Brooks, R. H., & Corey, A. T. (1964). Hydraulic properties of porous media. *Hydrology Papers*.

Brown, K., Schlüter, S., Sheppard, A., & Wildenschild, D. (2014). On the challenges of measuring interfacial characteristics of three-phase fluid flow with x-ray microtomography. *Journal of Microscopy*, *253*(3), 171–182. https://doi.org/10.1111/jmi.12106

Brown, R. A., Hicks, R. J., & Hicks, P. M. (1994). Use of air sparging for in situ bioremediation. In *Air sparging for site remediation* (pp. 38–55).

Buades, A., Coll, B., & Morel, J.-M. (2005). A Non-Local Algorithm for Image Denoising. In *IEEE Computer Society Conference on Computer Vision and Pattern Recognition* (pp. 60–65). San Diego, CA. https://doi.org/10.1109/CVPR.2005.38

Chen, D., Pyrak-Nolte, L. J., Griffin, J., & Giordano, N. J. (2007). Measurement of interfacial area per volume for drainage and imbibition. *Water Resources Research*, *43*(12), 1–6. https://doi.org/10.1029/2007WR006021

Chen, X., & Slater, L. (2015). Gas bubble transport and emissions for shallow peat from a northern peatland: The role of pressure changes and peat structure. *Water Resources Research*, *51*(1), 151–168. https://doi.org/10.1002/2014WR016268

Cheng, J. T., Pyrak-Nolte, L. J., Nolte, D. D., & Giordano, N. J. (2004). Linking pressure and saturation through interfacial areas in porous media. *Geophysical Research Letters*, *31*(8), 1–4. https://doi.org/10.1029/2003GL019282

Cnudde, V., & Boone, M. N. (2013). High-resolution X-ray computed tomography in geosciences: A review of the current technology and applications. *Earth-Science Reviews*, *123*, 1–17. https://doi.org/10.1016/j.earscirev.2013.04.003

Costanza-Robinson, M. S., Harrold, K. H., & Lieb-Lappen, R. M. (2008). X-ray Microtomography Determination of Air−Water Interfacial Area−Water Saturation Relationships in Sandy Porous Media. *Environmental Science & Technology*, *42*(8), 2949–2956. https://doi.org/10.1021/es072080d

Culligan, K. A., Wildenschild, D., Christensen, B. S. B., Gray, W. G., & Rivers, M.

L. (2006). Pore-scale characteristics of multiphase flow in porous media: A comparison of air-water and oil-water experiments. *Advances in Water Resources*, *29*(2), 227–238. https://doi.org/10.1016/j.advwatres.2005.03.021

Culligan, K. A., Wildenschild, D., Christensen, B. S. B., Gray, W. G., Rivers, M. L., & Tompson, A. F. B. (2004). Interfacial area measurements for unsaturated flow through a porous medium. *Water Resources Research*, *40*(12), 1–12. https://doi.org/10.1029/2004WR003278

Diamantopoulos, E., & Durner, W. (2015). Closed-Form Model for Hydraulic Properties Based on Angular Pores with Lognormal Size Distribution. *Vadose Zone Journal*, *14*(2), vzj2014.07.0096. https://doi.org/10.2136/vzj2014.07.0096

Dullien, F. A. . (1992). *Porous Media: Fluid Transport and Pore Structure* (2nd ed.). Academic Press.

Federer, H. (1959). Curvature measures. *Trans. Amer. Math. Soc.*, *93*, 418–491.

Fortuin, N. P. M., & Willemsen, A. (2005). Exsolution of nitrogen and argon by methanogenesis in Dutch ground water. *Journal of Hydrology*, *301*(1–4), 1–13. https://doi.org/10.1016/j.jhydrol.2004.06.018

Fry, V. A., Istok, J. D., Semprini, L., O'Reilly, K. T., & Buscheck, T. E. (1995). Retardation of Dissolved Oxygen Due to a Trapped Gas Phase in Porous Media. *Ground Water*, *33*(3), 391–398. https://doi.org/10.1111/j.1745-6584.1995.tb00295.x

Geistlinger, H., Lazik, D., Krauss, G., & Vogel, H.-J. (2009). Pore-scale and continuum modeling of gas flow pattern obtained by high-resolution optical bench-scale experiments. *Water Resources Research*, *45*(4). https://doi.org/10.1029/2007WR006548

Glass, R. J., & Yarrington, L. (2003). Mechanistic modeling of fingering, nonmonotonicity, fragmentation, and pulsation within gravity/buoyant destabilized two-phase/unsaturated flow. *Water Resources Research*, *39*(3). https://doi.org/10.1029/2002WR001542

Godinez-Brizuela, O. E., Karadimitriou, N. K., Joekar-Niasar, V., Shore, C. A., & Oostrom, M. (2017). Role of corner interfacial area in uniqueness of capillary pressure-saturation- interfacial area relation under transient conditions. *Advances in Water Resources*, *107*, 10–21. https://doi.org/10.1016/j.advwatres.2017.06.007

Golub, G. H., Heath, M., & Wahba, G. (1979). Generalized Cross-Validation as a Method for Choosing a Good Ridge Parameter Generalized Cross-Validation as a Method for Choosing a Good Ridge Parameter. *Technometrics*, *21*(2), 215–223.

Grant, G. P., & Gerhard, J. I. (2007). Simulating the dissolution of a complex dense nonaqueous phase liquid source zone: 1. Model to predict interfacial area. *Water Resources Research*, *43*(12). https://doi.org/10.1029/2007WR006038

Gray, W. G., Dye, A. L., McClure, J. E., Pyrak-Nolte, L. J., & Miller, C. T. (2015). On the dynamics and kinematics of two-fluid-phase flow in porous media. *Water Resources Research*, *51*(7), 5365–5381. https://doi.org/10.1002/2015WR016921

Han, K., & Levenspiel, O. (1988). Extended monod kinetics for substrate, product, and cell inhibition. *Biotechnology and Bioengineering*, *32*(4), 430–447. https://doi.org/10.1002/bit.260320404

Hao, Y., Sun, Y., & J. Nitao, J. (2012). Overview of NUFT: A Versatile Numerical Model for Simulating Flow and Reactive Transport in Porous Media. In *Groundwater Reactive Transport Models* (pp. 212–239). BENTHAM SCIENCE PUBLISHERS. https://doi.org/10.2174/978160805306311201010212

Hassanizadeh, S. M., Celia, M. A., & Dahle, H. K. (2002). Dynamic Effect in the Capillary Pressure–Saturation Relationship and its Impacts on Unsaturated Flow. *Vadoze Zone Journal*, *1*(1), 38–57.

Hassanizadeh, S. M., & Gray, W. G. (1990). Mechanics and thermodynamics of multiphase flow in porous media including interphase boundaries. *Advances in Water Resources*, *13*(4), 169–186.

Hassanizadeh, S. M., & Gray, W. G. (1993). Thermodynamic basis of capillary pressure in porous media. *Water Resources Research*, *29*(10), 3389–3405. https://doi.org/10.1029/93WR01495

Hegele, P. R., & Mumford, K. G. (2014). Gas production and transport during bench-scale electrical resistance heating of water and trichloroethene. *Journal of Contaminant Hydrology*, *165*, 24–36. https://doi.org/10.1016/j.jconhyd.2014.07.002

Held, R. J., & Celia, M. A. (2001). Modelling support of functional relationships between capillary pressure, saturation, interfacial area and common lines. *Advances in Water Resources*, *24*(3–4), 325–343. https://doi.org/10.1016/S0309-1708(00)00060-9

Held, R. J., & Celia, M. A. (2001). Pore-scale modeling extension of constitutive relationships in the range of residual saturations. *Water Resources Research*, *37*(1), 165–170.

Herring, A. L., Harper, E. J., Andersson, L., Sheppard, A., Bay, B. K., & Wildenschild, D. (2013). Effect of fluid topology on residual nonwetting phase trapping: Implications for geologic CO2sequestration. *Advances in Water Resources*, *62*, 47–58. https://doi.org/10.1016/j.advwatres.2013.09.015

Herring, A. L., Middleton, J., Walsh, R., Kingston, A., & Sheppard, A. (2017). Flow rate impacts on capillary pressure and interface curvature of connected and disconnected fluid phases during multiphase flow in sandstone. *Advances in Water Resources*. https://doi.org/10.1016/j.advwatres.2017.05.011

Hunt, A. G., & Manga, M. (2003). Effects of Bubbles on the Hydraulic Conductivity of Porous Materials - Theoretical Results. *Transport in Porous Media*, *52*, 51–56. https://doi.org/10.1023/A:1022312927606

Jansik, D. P., Wildenschild, D., & Rosenberg, N. D. (2011). Flow Processes in the Dry Regime: The Effect on Capillary Barrier Performance. *Vadose Zone Journal*, *10*(4), 1173–1184. https://doi.org/10.2136/vzj2010.0128

Jiang, H., Guo, B., & Brusseau, M. L. (2020). Pore-Scale Modeling of Fluid-Fluid Interfacial Area in Variably Saturated Porous Media Containing Microscale Surface Roughness. *Water Resources Research*, *56*(1), 1–21. https://doi.org/10.1029/2019WR025876

Joekar-Niasar, V., Doster, F., Armstrong, R. T., Wildenschild, D., & Celia, M. A. (2013). Trapping and hysteresis in two-phase flow in porous media: A pore-network study. *Water Resources Research*, *49*(7), 4244–4256. https://doi.org/10.1002/wrcr.20313

Joekar-Niasar, V., & Hassanizadeh, S. M. (2011). Specific interfacial area: The missing state variable in two-phase flow equations? *Water Resources Research*, *47*(5), 1–14. https://doi.org/10.1029/2010WR009291

Joekar-Niasar, V., & Hassanizadeh, S. M. (2012). Uniqueness of Specific Interfacial Area-Capillary Pressure-Saturation Relationship Under Non-Equilibrium Conditions in Two-Phase Porous Media Flow. *Transport in Porous Media*, *94*(2), 465–486. https://doi.org/10.1007/s11242-012-9958-3

Joekar-Niasar, V., Hassanizadeh, S. M., & Leijnse, A. (2008). Insights into the relationships among capillary pressure, saturation, interfacial area and relative permeability using pore-network modeling. *Transport in Porous Media*, *74*(2), 201–219. https://doi.org/10.1007/s11242-007-9191-7

Johnson, J. W., Nitao, J. J., & Knauss, K. G. (2004). Reactive transport modelling of CO 2 storage in saline aquifers to elucidate fundamental processes, trapping mechanisms and sequestration partitioning. *Geological Society, London, Special Publications*, *233*(1), 107–128. https://doi.org/10.1144/GSL.SP.2004.233.01.08

Johnson, R. L., Johnson, P. C., McWhorter, D. B., Hinchee, R. E., & Goodman, I. (1993). An Overview of In Situ Air Sparging. *Groundwater Monitoring & Remediation*, *13*(4), 127–135. https://doi.org/10.1111/j.1745-6592.1993.tb00456.x

Karadimitriou, N. K., Hassanizadeh, S. M., Joekar-Niasar, V., & Kleingeld, P. J.

(2014). Micromodel study of two-phase flow under transient conditions: Quantifying effects of specific interfacial area. *Water Resources Research*, *50*(10), 8125–8140. https://doi.org/10.1002/2014WR015388.Received

Karadimitriou, N. K., Musterd, M., Kleingeld, P. J., Kreutzer, M. T., Hassanizadeh, S. M., & Joekar-Niasar, V. (2013). On the fabrication of PDMS micromodels by rapid prototyping, and their use in two-phase flow studies. *Water Resources Research*, *49*(4), 2056–2067. https://doi.org/10.1002/wrcr.20196

Kawanishi, T., Hayashi, Y., Roberts, P. V, & Blunt, M. J. (1998). Fluid–fluid interfacial area during two and three phase fluid displacement in porous media: a network model study. In *GQ 98. International Conference and Special Seminars on Groundwater Quality: Remediation and Protection*.

Krol, M. M., Mumford, K. G., Johnson, R. L., & Sleep, B. E. (2011). Modeling discrete gas bubble formation and mobilization during subsurface heating of contaminated zones. *Advances in Water Resources*, *34*(4), 537–549. https://doi.org/10.1016/j.advwatres.2011.01.010

Kwon, Y. B., Weon, B. M., Won, K. H., Je, J. H., Hwu, Y., & Margaritondo, G. (2009). X-ray induced changes in wettability. *Langmuir*, *25*(13), 1927–1929. https://doi.org/10.1021/la804081k

Lenormand, R., Touboul, E., & Zarcone, C. (1988). Numerical models and experiments on immiscible displacements in porous media. *Journal of Fluid Mechanics*, *189*, 165–187. https://doi.org/10.1017/S0022112088000953

Leu, L., Berg, S., Enzmann, F., Armstrong, R. T., & Kersten, M. (2014). Fast X-ray Micro-Tomography of Multiphase Flow in Berea Sandstone: A Sensitivity Study on Image Processing. *Transport in Porous Media*, *105*(2), 451–469. https://doi.org/10.1007/s11242-014-0378-4

Leverett, M. C. (1941). Capillary Behavior in Porous Solids. *Transactions of the AIME*, *142*(01), 152–169. https://doi.org/10.2118/941152-G

Li, H., Hu, L., Song, D., & Al-tabbaa, A. (2014). Subsurface Transport Behavior of Micro-Nano Bubbles and Potential Applications for Groundwater Remediation. *International Journal of Environmental Research and Public Health*, *11*(1), 473–486. https://doi.org/10.3390/ijerph110100473

Li, T., Schlüter, S., Dragila, M. I., & Wildenschild, D. (2018). An improved method for estimating capillary pressure from 3D microtomography images and its application to the study of disconnected nonwetting phase. *Advances in Water Resources*, *114*, 249–260. https://doi.org/10.1016/j.advwatres.2018.02.012

Lorensen, W. E., & Cline, H. E. (1987). Marching cubes: A high resolution 3D surface construction algorithm. *Proceedings of the 14th Annual Conference on Computer Graphics and Interactive Techniques - SIGGRAPH '87*, (August

1987), 163–169. https://doi.org/10.1145/37401.37422

McClure, J. E., Armstrong, R. T., Berrill, M. A., Berg, S., Gray, W. G., & Miller, C. T. (2018). Geometric state function for two-fluid flow in porous media. *Physical Review Fluids*, *3*(084306), 1–16. https://doi.org/10.1103/PhysRevFluids.3.084306

McClure, J. E., Berrill, M. A., Gray, W. G., & Miller, C. T. (2016). Influence of phase connectivity on the relationship among capillary pressure, fluid saturation, and interfacial area in two-fluid-phase porous medium systems. *Physical Review E*, *94*(3), 1–12. https://doi.org/10.1103/PhysRevE.94.033102

McClure, J. E., Pan, C., Adalsteinsson, D., Gray, W. G., & Miller, C. T. (2004). Estimating interfacial areas resulting from lattice Boltzmann simulation of two-fluid-phase flow in a porous medium. In *Developments in Water Science* (pp. 23–35). https://doi.org/10.1016/S0167-5648(04)80034-0

Meisenheimer, D. E., McClure, J. E., Rivers, M. L., & Wildenschild, D. (2020). Exploring the effect of flow condition on the constitutive relationships for two-phase flow. *Advances in Water Resources*, *137*. https://doi.org/10.1016/j.advwatres.2020.103506

Meisenheimer, D. E., Rivers, M. L., & Wildenschild, D. (2020). Optimizing pink-beam fast X-ray microtomography for multiphase flow in 3D porous media. *Journal of Microscopy*. https://doi.org/10.1111/jmi.12872

Michiel, M. Di, Merino, J. M., Fernandez-carreiras, D., Buslaps, T., Honkimäki, V., Falus, P., … Svensson, O. (2005). Fast microtomography using high energy synchrotron radiation. *Rev. Sci. Instrum.*, *76*(043702). https://doi.org/10.1063/1.1884194

Miller, C., Christakos, G., & Imhoff, P. (1998). Multiphase flow and transport modeling in heterogeneous porous media: challenges and approaches. *Advances in Water Resources*, *21*(2), 77–120. https://doi.org/10.1016/S0309-1708(96)00036-X

Mokso, R., Marone, F., Haberthür, D., Schittny, J. C., Mikuljan, G., Isenegger, A., & Stampanoni, M. (2010). Following Dynamic Processes by X-ray Tomographic Microscopy with Sub-second Temporal Resolution. In *10th International Conference on X-Ray Microscopy* (pp. 38–41). Chicago, IL: American Institute of Physics.

Molnar, I. L., Mumford, K. G., & Krol, M. M. (2019). Electro-Thermal Subsurface Gas Generation and Transport: Model Validation and Implications. *Water Resources Research*, *55*, 4630–4647. https://doi.org/10.1029/2018WR024095

Monod, J. (1949). The Growth of Bacterial Cultures. *Annual Review of Microbiology*, *3*(1), 371–394. https://doi.org/10.1146/annurev.mi.03.100149.002103

Oldenburg, C. M., & Unger, A. J. A. (2003). On Leakage and Seepage from Geologic Carbon Sequestration Sites: Unsaturated Zone Attenuation. *Vadose Zone Journal*, *2*(3), 287–296. https://doi.org/10.2136/vzj2003.2870

Oostrom, M., White, M. D., & Brusseau, M. L. (2001). Theoretical estimation of free and entrapped nonwetting–wetting fluid interfacial areas in porous media. *Advances in Water Resources*, *24*(8), 887–898. https://doi.org/10.1016/S0309-1708(01)00017-3

Or, D., & Tuller, M. (1999). Liquid retention and interfacial area in variably saturated porous media: Upscaling from single-pore to sample-scale model. *Water Resources Research*, *35*(12), 3591–3605. https://doi.org/10.1029/1999WR900262

Porter, M. L., Schaap, M. G., & Wildenschild, D. (2009). Lattice-Boltzmann simulations of the capillary pressure-saturation-interfacial area relationship for porous media. *Advances in Water Resources*, *32*(11), 1632–1640. https://doi.org/10.1016/j.advwatres.2009.08.009

Porter, M. L., Wildenschild, D., Grant, G., & Gerhard, J. I. (2010). Measurement and prediction of the relationship between capillary pressure, saturation, and interfacial area in a NAPL-water-glass bead system. *Water Resources Research*, *46*(8), 1–10. https://doi.org/10.1029/2009WR007786

Prodanović, M., & Bryant, S. L. (2006). A level set method for determining critical curvatures for drainage and imbibition. *Journal of Colloid and Interface Science*, *304*(2), 442–458. https://doi.org/10.1016/j.jcis.2006.08.048

Pruess, K., Oldenburg, C., & Moridis, G. (1999). TOUGH2 user's guide version 2. Berkeley, CA (US): Ernest Orlando Lawrence Berkeley National Laboratory.

Pyrak-Nolte, L. J., Nolte, D. D., Chen, D., & Giordano, N. J. (2008). Relating capillary pressure to interfacial areas. *Water Resources Research*, *44*(6), 1–14. https://doi.org/10.1029/2007WR006434

Reeves, P. C., & Celia, M. a. (1996). A functional-relationship between capillary-pressure, saturation, and interfacial area as revealed by a pore-scale network model. *Water Resources Research*, *32*(8), 2345–2358. https://doi.org/10.1029/96WR01105

Rivers, M. L. (2012). tomoRecon: High-speed tomography reconstruction on workstations using multi-threading. *Proceedings of SPIE*, *Stuart R. Stock*, *Eds.*, *8506*, 85060U–1–85060U–13. https://doi.org/doi: 10.1117/12.930022

Rücker, M., Berg, S., Armstrong, R. T., Georgiadis, A., Ott, H., Schwing, A., … Kersten, M. (2015). From connected pathway flow to ganglion dynamics. *Geophysical Research Letters*, *42*(10), 3888–3894. https://doi.org/10.1002/2015GL064007

Scanziani, A., Singh, K., Blunt, M. J., & Guadagnini, A. (2017). Automatic method for estimation of in situ effective contact angle from X-ray micro tomography images of two-phase flow in porous media. *Journal of Colloid and Interface Science*, *496*, 51–59. https://doi.org/10.1016/j.jcis.2017.02.005

Schlüter, S., Berg, S., Li, T., Vogel, H.-J., & Wildenschild, D. (2017). Time scales of relaxation dynamics during transient conditions in two-phase flow. *Water Resources Research*, *53*, 4709–4724. https://doi.org/10.1002/2017WR020840

Schlüter, S., Berg, S., Rücker, M., Armstrong, R. T., Vogel, H.-J., Hilfer, R., & Wildenschild, D. (2016). Pore-scale displacement mechanisms as a source of hysteresis for two-phase flow in porous media. *Water Resources Research*, *52*(3), 2194–2205. https://doi.org/10.1002/2015WR018254

Singh, K., Menke, H., Matthew, A., Lin, Q., Rau, C., Blunt, M. J., & Bijeljic, B. (2017). Dynamics of snap-off and pore- filling events during two-phase fluid flow in permeable media. *Scientific Reports*, *7*, 5192. https://doi.org/10.1038/s41598-017-05204-4

Triplett Kingston, J. L., Dahlen, P. R., & Johnson, P. C. (2010). State-of-the-Practice Review of In Situ Thermal Technologies. *Ground Water Monitoring & Remediation*, *30*(4), 64–72. https://doi.org/10.1111/j.1745-6592.2010.01305.x

van Genuchten, M. T. (1980). A Closed-form Equation for Predicting the Hydraulic Conductivity of Unsaturated Soils. *Soil Science Society of America Journal*, *44*(5), 892–898. https://doi.org/10.2136/sssaj1980.03615995004400050002x

Wildenschild, D. (2009). Experimental analysis of non-equilibrium processes for multiphase flow in porous media. In *SIAM Conference on Mathematical and Computational Issues in the Geosciences*. Leipzig, Germany.

Wildenschild, D., Hopmans, J. W., Rivers, M. L., & Kent, A. J. R. (2005). Quantitative Analysis of Flow Processes in a Sand Using Synchrotron-Based X-ray Microtomography. *Vadose Zone Journal*, *4*(1), 112–126. https://doi.org/https://doi.org/10.2113/4.1.112

Wildenschild, D., Hopmans, J. W., & Šimůnek, J. (2001). Flow Rate Dependence of Soil Hydraulic Characteristics. *Soil Science Society of America Journal*, *65*(1), 35–48. https://doi.org/10.2136/sssaj2001.65135x

Wildenschild, D., & Prodanovic, M. (2009). Effect of pore space morphology on interfacial configurations in porous media. In *SIAM Geosciences Annual Meeting*.

Wildenschild, D., & Sheppard, A. P. (2013). X-ray imaging and analysis techniques for quantifying pore-scale structure and processes in subsurface porous medium systems. *Advances in Water Resources*, *51*, 217–246. https://doi.org/10.1016/j.advwatres.2012.07.018

Wood, S. N., & Shaw, S. (2015). Generalized additive models for large data sets. *Journal of the Royal Statistical Society*, *64*, 139–155.

Youssef, S., Deschamps, H., Dautriat, J., Rosenberg, E., Oughanem, R., Maire, E., & Mokso, R. (2013). 4D IMAGING OF FLUID FLOW DYNAMICS IN NATURAL POROUS MEDIA WITH ULTRA-FAST X-RAY MICROTOMOGRAPHY. *International Symposium of Core Analyst*, (SCA2013-012).

Zuo, L., Ajo-Franklin, J. B., Voltolini, M., Geller, J. T., & Benson, S. M. (2017). Pore-scale multiphase flow modeling and imaging of CO2 exsolution in Sandstone. *Journal of Petroleum Science and Engineering*, *155*, 63–77. https://doi.org/10.1016/j.petrol.2016.10.011